Faculty of Applied Engineering
Research Group of Applied Electrochemistry & Catalysis (ELCAT)

Enhancing the stability of Sn-based electrocatalysts for the electrochemical CO_2 reduction towards formate

PhD thesis submitted for the degree of Doctor in Applied Engineering at the University of Antwerp

Kevin Van Daele

Promotors:

Prof. dr Tom Breugelmans

Dr Deepak Pant

Antwerp, 2023

Enhancing the stability of Sn-based electrocatalysts for the electrochemical CO_2 reduction towards formate

Kevin Van Daele

Members of the Jury

Prof. dr Maarten Weyn	President of the Jury Imec/IDLab, University of Antwerp
Dr Daniel Choukroun	Secretary of the Jury ELCAT, University of Antwerp
Prof. dr Tom Breugelmans	Promotor ELCAT, University of Antwerp
Dr Deepak Pant	Promotor VITO
Prof. dr Christophe Vande Velde	Jury Member iPRACS, University of Antwerp
Prof. dr Pascal Van Der Voort	External Jury Member COMOC, University of Ghent
Dr Metin Bulut	External Jury Member VITO
Dr Nejc Hodnik	External Jury Member Laboratory for Electrocatalysis, National Institute of Chemistry Slovenia

This PhD was realised in collaboration with the Flemish Institute for Technological Research (VITO).

The candidate was financially supported through a PhD fellowship strategic basic research (1S83320N) from the Research Foundation Flanders (FWO).

Acknowledgements

It's a strange feeling, finalising my dissertation, after almost five years, by writing these indispensable words of gratitude. As Albus Dumbledore (J. K. Rowling) once said, *"Words are, in my not-so-humble opinion, our most inexhaustible source of magic"*, however, words will never be enough to express how grateful I am to everyone who supported me throughout my PhD.

First and foremost, I want to express my gratitude to my promotors Tom and Deepak. Tom, thank you for believing in me and giving me the opportunity to pursue a PhD, thank you for your guidance and for knowing me so well that you always knew exactly what to say or do to help me move forward. Deepak, thank you for your support, advice, feedback and guidance throughout my PhD. You've always approached my research from a different perspective, which has proven to be invaluable.

In addition to my supervisors, I also received guidance from Nick. Nick, thank you for all the brainstorming, proofreading everything from my FWO to scientific manuscripts and this dissertation and above all, thank you for always asking the right questions during our meetings and for pointing me in the right direction when I felt stuck. You've had a great influence on the outcome of my PhD, for which I cannot thank you enough.

Next, I would like to thank all my ELCAT colleagues. I remember the day I started, when ELCAT was still called ART and I met Daniel, Lien and

Filip, who were the first colleagues I shared an office with. Together with Jonas, Sander, Bert, Oriol, Jonathan, Miguel and Giulia, they made me feel right at home. Since then, ELCAT has grown immensely and many other wonderful colleagues have joined. Thank you, Thomas A., Thomas K., Michiel D. R., Michiel V., Järi, Sven, Mathias, Siebe, Sam, Michele, Lieven, Robbe, Hannelore, Kavita, Quinten, Renée, Shankar, Brend, Fernando and Yu. Thank you for all the laughs, the extracurricular activities and for the friendship. A special thanks to Saskia, Alana and Barbara with whom I shared my last office as a PhD student at ELCAT. Thank you for suffering through my stressing for deadlines and thank you for all the talks and the brainstorm sessions.

Furthermore, I wish to thank everyone who collaborated with me during my PhD. Prof. Sara Bals and the EMAT research group, Prof. Pegie Cool and LADCA, Prof. Christophe Vande Velde and iPRACS, Prof. Ruud Kortlever, Prof. Tom Hauffman and Kitty Baert.

Without the support of my friends and family, this PhD would have been a tremendously long challenge. Thank you, Jens and Jonas, for always being flexible when I had deadlines or was stressing about my research, so we could meet anyway. Thank you for asking about how my PhD was going and thank you for taking my mind off of things during our dinners, movie/gaming nights, bouldering sessions and typical Jens-Kevin brother evenings. Thank you, Horst, Hedwige, Hanne and Saran, for the amazing moments and holidays we've spent together and thank you for always being so welcoming and making me feel like a part of your family. Thank

you, Katja, for being my big sister. I am confident that you will always have my back, and you will never have to worry because I will always have yours. Thank you, mom and dad, for always allowing and enabling me to chase my dreams, nothing is ever too much for you.

Ultimately, Anke, my love, there are so many things I wish to thank you for. We've met right before I was about to start my PhD and throughout these past five years, you've constantly been there for me whenever, whether I was stressed or feeling down because an experiment didn't go as planned or whether I was overjoyed because one of my manuscripts got accepted. Thank you for genuinely showing interest in my research and for listening to me talk about SnO_2 electrocatalysts and the electrochemical CO_2 reduction for, sometimes, hours at a time, and even then you kept asking questions because you wanted to understand and know what I was doing. Zoals wij altijd zeggen; *ik zie je dierentuin graag* en ik kijk uit naar de volgende hoofdstukken van onze toekomst samen.

Thank you!

Mischief managed,

Kevin

Summary

Since the start of the second industrial revolution in the late 19th century, a rapid increase in anthropogenic CO_2 emissions and land-use changes have been supercharging the natural greenhouse effect, making CO_2 Earth's most harmful and prevalent greenhouse gas, bringing about global warming, disrupted weather patterns and an acidification of the oceans.

The electrochemical CO_2 reduction (eCO_2R) into industrially valuable products has become one of the most promising technologies to valorise anthropogenic CO_2 emission, while simultaneously providing a means of energy storage for intermittent renewable sources, such as wind-, solar- and hydro energy. According to most eCO_2R literature and techno-economic assessments, the eCO_2R towards formate/formic acid (FA) has the potential to generate the highest revenue per mole of consumed electrons. However, for this process to become industrially feasible, a low cost catalyst with excellent activity, selectivity and stability is required. While state-of-the-art literature reports a wide variety highly selective and active Sn-based electrocatalysts, their stability is currently inadequate for industrial application of the eCO_2R towards formate/formic acid.

In the first chapters (Chapter 1-4) of this dissertation, a general introduction, highlighting the need for anthropogenic carbon dioxide abatement and several promising technologies, is provided, before delving deeper into the state-of-the-art Sn-based electrocatalysts, followed by an applied consideration of the basic principles of electrocatalysis and rational

electrocatalyst design. An extensive literature study (Chapter 4) allows for the most commonly described degradation pathways to be unravelled for a wide variety of Sn-based electrocatalyst and to propose several mitigation strategies to enhance their long-term stability.

Next, Chapters 5 and 6 describe the synthesis of 'novel' Sn-based electrocatalysts for the eCO_2R towards FA. First, a newly designed SnO_2 containing nitrogen doped ordered mesoporous carbon electrocatalyst (Sn-N-OMC) was synthesised and characterised in-depth to elucidate their electrochemical performance. Yielding a promising FE_{FA} of $60-70\%$ which decreases to 43% after 24 h of electrolysis, the Sn-N-OMC electrocatalysts provided valuable insights into the effect of the SnO_2 species and the nitrogen-doped carbon support on the electrochemical performance. Next, Pomegranate structured SnO_2 and SnO_2@C electrocatalysts (Pom. SnO_2 and Pom. SnO_2@C) where synthesised using the same particle confinement strategy as the Sn-N-OMC catalyst, but to simultaneously increase their performance for the eCO_2R towards FA. The Pom. SnO_2 electrocatalyst exhibits an excellent 24 h stability, maintaining an average FE_{FA} of 83%. Counterintuitively, the Pom. SnO_2@C electrocatalyst, which retained its morphology much better, displayed a decrease in FE_{FA} from 83% to 46% after 24 h of electrolysis. This loss of selectivity, however, proved to be temporary since most of its selectivity was restored to the original FE_{FA}, by leaving the GDE to dry in air. *Ex situ* physicochemical characterisation was used to unambiguously link this temporary selectivity loss of the Pom. SnO_2@C electrocatalyst to the *in situ* SnO_2 reduction to metallic Sn.

Finally, in chapter 7, pulsed-eCO_2R is explored as an alternative electrochemical technique to further enhance the stability of the Pom. SnO_2@C electrocatalyst. Applying a precisely controlled transient operating potential, the Pom. SnO_2@C electrocatalyst maintained a high selectivity of 78 ± 2% after 72 cycles of p-eCO_2R, with a slight decrease of 6%, whereas previously a decrease of at least 15% was observed over the same time period under steady-state operating conditions. Eventually, a similar decrease in FE_{FA} was observed after 24 h of p-eCO_2R, yielding a FE_{FA} of 44%, indicating that while the *in situ* SnO_2 appears to be slowed down, it isn't completely nullified. Additional fine-tuning of the pulse parameters, combined with in-depth physicochemical characterisation are required to unlock the full potential of this novel technique for enhancing the stability of Sn-based electrocatalysts.

Throughout this dissertation, several important insights were gained concerning the stability of Sn-based electrocatalysts. Moreover, several major morphological degradation pathways were diminished, utilising a particle confinement strategy, and the possibilities to further enhance Sn-based electrocatalyst stability, by decreasing *in situ* SnO_2 reduction via pulsed potential eCO_2R, were explored, paving the way for future research.

Samenvatting

Sinds het begin van de tweede industriële revolutie, eind 19e eeuw, versterken een snelle toename van antropogene CO_2-emissies en veranderingen in het landgebruik het natuurlijke broeikaseffect. Hierdoor is CO_2 het meest voorkomende en schadelijkste broeikasgas op aarde geworden, met als gevolg de opwarming van de aarde, verstoorde weerpatronen en verzuring van de oceanen.

De elektrochemische reductie van CO_2 (eCO_2R) tot industrieel waardevolle producten is een van de meest veelbelovende technologieën geworden om deze antropogene CO_2-uitstoot te valoriseren. Tegelijkertijd biedt de eCO_2R een manier om hernieuwbare energie van onregelmatig beschikbare bronnen, zoals wind-, zonne- en waterenergie op te slaan. Volgens de meeste eCO_2R literatuur en techno-economische evaluaties heeft de omzetting van CO_2 naar mierenzuur/formiaat (Formic acid/formate, FA) het potentieel om de hoogste opbrengst per mol verbruikte elektronen te genereren. Om dit proces industrieel haalbaar te maken is echter een goedkope katalysator met uitstekende activiteit, selectiviteit en stabiliteit nodig. Hoewel de meest recente literatuur een grote verscheidenheid aan zeer selectieve en actieve Sn-gebaseerde elektrokatalysatoren meldt, is hun stabiliteit momenteel onvoldoende voor industriële toepassing.

In de eerste hoofdstukken (Hoofdstuk 1-4) van dit proefschrift wordt een algemene inleiding gegeven. Hierin worden de noodzaak van het verminderen van door de mens veroorzaakt koolstofdioxide en

verschillende veelbelovende technologieën benadrukt. Vervolgens wordt dieper ingegaan op de state-of-the-art Sn-gebaseerde elektrokatalysatoren, gevolgd door een toegepaste beschouwing van de basisprincipes van elektrokatalyse op de elektrochemische CO_2 reductie. Een uitgebreide literatuurstudie maakt het mogelijk om de meest voorkomende manieren van degradatie te ontrafelen voor een breed scala aan Sn-gebaseerde elektrokatalysatoren en verschillende strategieën voor het verbeteren van hun lange termijn stabiliteit voor te stellen.

Hoofdstukken 5 en 6 beschrijven de synthese van 'nieuwe' Sn-gebaseerde elektrokatalysatoren voor de elektrochemische omzetting van CO_2 naar FA. Allereerst werden nieuwe SnO_2 bevattende stikstof-gedoteerde koolstof (Sn-N-OMC) elektrokatalysatoren gesynthetiseerd. Een grondige karakterisatie van de geordende mesoporeuze structuur en aanwezige SnO_2 species laten toe om de elektrochemische prestaties te verklaren. Met een veelbelovende maximum selectiviteit (Faradische efficiëntie voor FA, FE_{FA}) van 60-70%, die na 24 uur elektrolyse afneemt tot 43%, leverden de Sn-N-OMC elektrokatalysatoren waardevolle inzichten in het effect van de soorten SnO_2 en het dragermateriaal op de elektrochemische prestaties. Vervolgens werden SnO_2 en SnO_2@C elektrokatalysatoren met een granaatappel (pomegranate) structuur (Pom. SnO_2 en Pom. SnO_2@C) gesynthetiseerd, gebruik makende van dezelfde 'particle confinement' strategie als de Sn-N-OMC katalysator. De Pom. SnO_2 elektrokatalysator vertoont een uitstekende stabiliteit gedurende 24 uur, met een gemiddelde FE_{FA} van 83%. De Pom. SnO_2@C behoudt, volgens *ex situ* TEM

karakterisatie, zijn morfologie beter, maar vertoont contra-intuïtief een afname in zijn selectiviteit van 83% naar 46% na 24 uur elektrolyse. Dit verlies van selectiviteit blijkt echter tijdelijk te zijn, aangezien het grootste deel van de selectiviteit hersteld kan worden naar de oorspronkelijke FE_{FA} door de GDE (Gas Diffusie Elektrode) te laten drogen aan de lucht. Met behulp van verscheidene karakterisatietechnieken werd dit tijdelijke verlies van selectiviteit van de Pom. SnO_2@C elektrokatalysator ondubbelzinnig gekoppeld aan de *in situ* reductie van SnO_2 tot metallisch Sn.

Ten slotte wordt gepulseerde-eCO_2R (p-eCO_2R) onderzocht, in Hoofdstuk 7, als alternatieve elektrochemische techniek om de stabiliteit van de Pom. SnO_2@C elektrokatalysator verder te verbeteren. Door het toepassen van een nauwkeurig gecontroleerde pulserende potentiaal behoudt de Pom. SnO_2@C elektrokatalysator een hoge selectiviteit van 78 ± 2% na 72 cycli p-eCO2R, met een lichte afname van 6%, terwijl eerder een afname van minstens 15% werd waargenomen gedurende dezelfde tijdsperiode. Uiteindelijk werd een vergelijkbare afname in FE_{FA} waargenomen na 24 uur p-eCO2R, resulterend in een FE_{FA} van 44%. Dit geeft aan dat, hoewel p-eCO_2R de *in situ* SnO_2-reductie vertraagt, deze voorlopig niet volledig geëlimineerd wordt. Extra onderzoek naar de optimale puls parameters, in combinatie met grondige karakterisatie, is vereist om het volledige potentieel van deze jonge techniek voor het verbeteren van de stabiliteit van Sn-gebaseerde elektrokatalysatoren te ontsluiten.

In deze dissertatie werden verschillende belangrijke inzichten verworven met betrekking tot de stabiliteit van Sn-gebaseerde elektrokatalysatoren.

Bovendien werd de morfologische degradatie verminderd door het toepassen van de 'particle confinement' strategie. Tot slot werd de mogelijk onderzocht om de stabiliteit van Sn-gebaseerde elektrokatalysatoren verder te verbeteren door de *in situ* SnO_2-reductie te verminderen via gepulseerde-eCO_2R, waarmee de weg werd vrijgemaakt voor toekomstig onderzoek.

Table of Contents

Nomenclature

ADT	Accelerated degradation/durability test
APS	Ammonium peroxydisulfate
ASF	Activity-stability factor
ATR-IR	Attenuated total reflectance infrared spectroscopy
BET	Brunauer-Emmett-Teller
CA	Chronoamperometric
CC	Carbon Capture
CCS	Carbon capture and storage
CCU	Carbon capture and utilisation
CCUS	Carbon capture, utilisation and storage
COD	Crystallography Open Database
CP	Chronopotentiometric
DAC	Direct Air Capture
DEA	Diethanolamine
DFAFC	Direct formic acid fuel cell
DFFC	Direct formate fuel cell
DFT	Density functional theory
DI	Deionised

eCO_2R	Electrochemical CO_2 reduction
ECSA	Electrochemically active surface area
EDL	Electrical double layer
EDS	Energy dispersive spectrometer
EE	Energy efficiency
EXAFS	Extended X-ray absorption fine structure
FA	Formate/Formic acid
FE	Faradaic efficiency (selectivity)
FE_{FA}	Faradaic efficiency towards formic acid
FFT	Fast Fourier Transformations
GDE	Gas diffusion electrode
GHG	Greenhouse gas
HAADF-STEM	High angle annular dark-field scanning transmission electron microscopy
HER	Hydrogen evolution reaction
HPLC	High-performance liquid chromatography
HRTEM	High-resolution transmission electron microscopy
ICP-OES	Inductively coupled plasma optical emission spectroscopy
IEA	International Energy Agency

IHP	Inner Helmholtz plane
IPCC	Intergovernmental panel on climate change
IR	Infrared
IUPAC	International Union of Pure and Applied Chemistry
LAADF-STEM	Low angle annular dark-field scanning transmission electron microscopy
LP-TEM	Liquid-phase transmission electron microscopy
MEA	Monoethanolamine
	Membrane electrode assembly
NMR	Nuclear magnetic resonance
N-OMC	Nitrogen doped ordered mesoporous carbon
N-sorption	Nitrogen physisorption
OCV	Open circuit voltage (OCP, open circuit potential)
OER	Oxygen evolution reaction
OHP	Outer Helmholtz plane
PCET	Proton-coupled electron transfer
p-eCO_2R	Pulsed electrochemical CO_2 reduction
PEMFC	Proton exchange membrane fuel cell
Ppm	Parts per million
RDE	Rotating disk electrode

RDS	Rate-determining step
RHE	Reversible hydrogen electrode
SDA	Structure directing agent
SEM	Scanning electron microscopy
S-number	Stability-number
STEM	Scanning transmission electron microscopy
TEA	Techno-economic assessment
TEM	Transmission electron microscopy
TEOS	Tetraethyl orthosilicate
TOF	Turnover frequency
TPB	Triple-phase boundary
TRLs	Technology readiness levels
UPD	Underpotential deposition
UTF	Ultra-thin film
XAS	X-ray absorption spectroscopy
XPS	X-ray photoelectron spectroscopy
XRD	X-ray powder diffraction

List of Symbols

a_i	Activity of species i
°C	Degree Celsius
C_{dl}	Double layer capacitance [mF]
C_i	Concentration of species i
δ	Boundary layer thickness [µm]
E_a	Activation energy
	Applied anodic potential [V]
E_c	Applied Cathodic potential [V]
E_{cell}	Cell potential [V]
F	Faraday constant (9.6485 x 10^4 C mol^{-1})
FE%	Faradaic efficiency [%]
f_p	Pulse frequency [Hz or s^{-1}]
γ_i	Activity coefficient of species i
G	Gibbs free energy
ΔG	Change in Gibbs free energy
ΔG_{RI}	Gibbs free energy reaction intermediate
Gt_C	Gigaton carbon
Gt_{CO_2}	Gigaton CO_2

h	Hour
ϑ	Theta [°], angle of diffraction
η	Overpotential [V]
φ	Potential [V]
I	Current [A or mA]
iR	Ohmic drop/resistance [Ω]
J	Current Density [mA cm^{-2}]
J_i	Partial current density for species i [mA cm^{-2}]
Mt	Megaton
n	Number of electrons
	Amount of moles
R	Ideal gas constant (8.3145 J mol^{-1} K^{-1})
RC	Resistor-capacitor time constant [ms]
S_{BET}	BET surface area [m^2 g^{-1}]
t	Ton
t_a	Anodic pulse time [s]
t_c	Cathodic pulse time [s]
t_p	Total cycle time (period) [s]
V	Voltage, Volt
z	Number of electrons

Chapter 1

Introduction

This first general introductory chapter highlights the societal relevance of my PhD dissertation. After highlighting one of the biggest scientific challenges of the 21st century, climate change, the urgent need for carbon dioxide sequestration via CCUS is demonstrated. Finally, the electrochemical CO_2 reduction towards formic acid is introduced as a promising technology and the need for stable Sn-based electrocatalysts is emphasised.

Part of this chapter has been published as K. Van Daele *et al.*, "Sn-Based Electrocatalyst Stability: A Crucial Piece to the Puzzle for the Electrochemical CO_2 Reduction toward Formic Acid," *ACS Energy Lett.*, vol. 6, no. 12, pp. 4317–4327, Dec. 2021.
(https://doi.org/10.1021/acsenergylett.1c02049)
And it has been updated with the latest state-of-the-art research.

1.1 Carbon dioxide: a 21st century problem

"There's one issue that will define the contours of this century more dramatically than any other, and that is the urgent and growing threat of a changing climate." (U.S. President Barack Obama, UN Climate Change Summit, September 23, 2014)

1.1.1 Supercharged greenhouse effect

Without greenhouse gases (GHGs), our planet would be uninhabitable since Earth's natural greenhouse effect would be too weak to keep the average global surface temperature above freezing. Natural greenhouse gases, such as, water vapour (H_2O), carbon dioxide (CO_2), ozone (O_3), methane (CH_4) and nitrous oxide (N_2O) trap long-wave (infrared, IR) radiation emitted from the Earth's surface, resulting in an average global temperature of 14 °C versus an estimated -18 °C in their absence. However, since the start of the second industrial revolution in the late 19th century, a rapid increase in anthropogenic CO_2 emissions and land-use changes have been supercharging this natural greenhouse effect, making CO_2 Earth's most harmful and prevalent GHG, bringing about global warming, disrupted weather patterns and an acidification of the oceans.[1,2]

Since the start of the first industrial revolution in 1750, a cumulative amount of more than 1.5 trillion tons of CO_2 has been emitted worldwide.[3] As a consequence, world's largest natural carbon sinks, i.e. vegetation (forests), oceans and soils, which are part of the global carbon cycle (Figure 1.1), aren't able to sequester the increased anthropogenic CO_2 emissions.

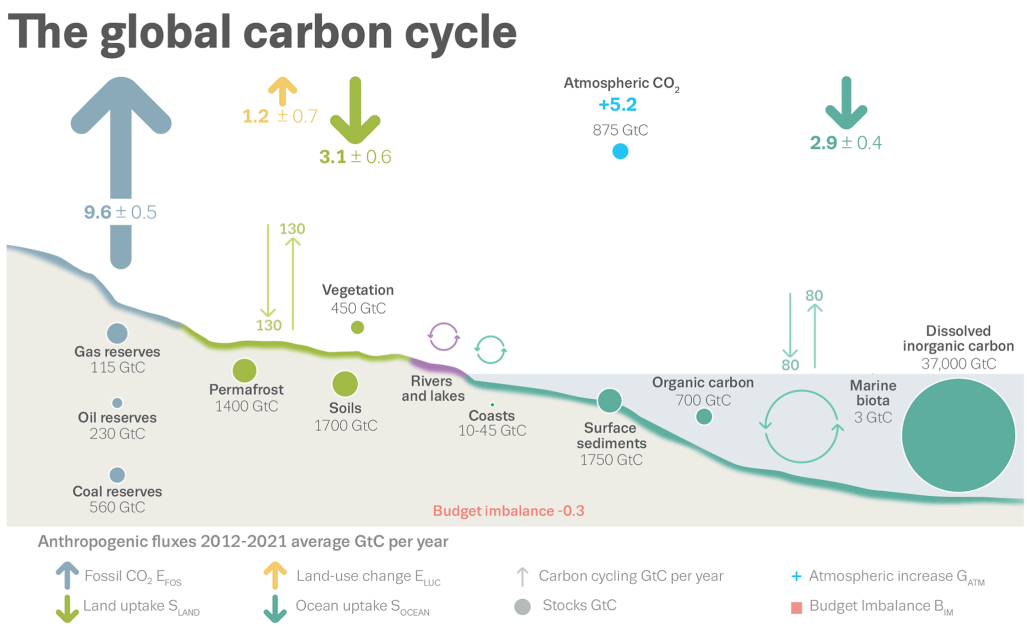

Figure 1.1 Averaged schematic representation of the global carbon cycle for the decade 2012-2021. The uncertainty of the atmospheric CO_2 growth rate of ±0.02 Gt_C was neglected for the figure. Gt_{CO_2} is equal to 3.664 times the value of Gt_C.[4]

This, in turn, has led to a more than 50% increase in atmospheric CO_2 from pre-industrial levels (1750, 278 ppm) to more than 417.2 ppm in 2022.[4] In order to limit global warming to well below 2 °C of warming above pre-industrial levels, as stipulated in the 2015 Paris agreement,[5] both the Intergovernmental Panel on Climate Change (IPCC)[6] and the International Energy Agency (IEA) estimate that collective anthropogenic CO_2 emissions, which are currently over 40.0 Gt_{CO_2} per year (2021) and continue to rise, should drastically be reduced to near-zero by 2050 and even to net-negative emissions by the end of the 21st century.[4,7] Moreover, the remaining carbon budget, i.e. the maximum amount of anthropogenic CO_2 that can still be spent (emitted) in the future, for a 50% probability to limit global warming to 1.5 and 2 °C has, respectively, been reduced to

380 and 1230 Gt_{CO_2} from the beginning of 2023. Assuming CO_2 emission levels of 40.5 Gt_{CO_2} $year^{-1}$, as recorded in 2022, this remaining carbon budget will be spent in approximately 9 or 30 years, respectively.[4]

Even today, with a global warming of "only" 1.2 °C above pre-industrial levels,[6,8] the effects of climate change are undeniable. An increased global warming beyond 2 °C would only make these effects more extreme, with some scientists even predicting a largely uninhabitable and hostile planet if global warming were to reach levels above 4 °C.[6,9–12] Evidently, profound transformations and innovations are necessary if humanity wants to become carbon neutral and limit climate change.[13] Reaching net zero CO_2 emission by 2050 calls for an average decrease in collective anthropogenic CO_2 emission of approximately 1.4 Gt_{CO_2} each year.[4] A substantial amount of action is thus required, equivalent to the observed reduction of 6.3% (2.2 Gt_{CO_2}) in CO_2 emissions during the 2020 COVID-19 pandemic.[14–17]

According to the IPCC, the majority of anthropogenic carbon dioxide emissions are considered to be fossil CO_2, originating from (1) fossil fuel (petroleum, coal and natural gas) combustion for electricity, transport, industry and buildings; (2) fossil carbonates ($CaCO_3$) in cement production and (3) other industrial processes such as chemical and fertilizer manufacturing.[6] Besides the necessary transition into a decarbonized energy system with renewable energy sources[18] and battery or fuel cell powered methods of transportation,[19] other CO_2 emission may need to be offset or abated in another way, in order to limit global warming to well

below 2° C.[20] Innovative negative carbon technologies such as Carbon Capture and Storage (CCS) or Carbon Capture and Utilization (CCU) provide a promising mitigation strategy to strive towards a carbon neutral future.[21–24]

1.1.2 Can we recycle CO_2?

An overwhelmingly large amount of chemicals in our day-to-day lives, such as plastics or wind- and waterproof clothing (perfluorinated polymers) contain carbon (C) which typically originates from finite fossil-C sources. While it is possible to completely decarbonise our energy system, the chemical industry, which will always require carbon, should be defossilised rather than decarbonised, by substituting the fossil-C source.[25] To this extent, CCU provides an interesting approach to recycle harmful carbon dioxide, while simultaneously closing the carbon cycle (Figure 1.2) and providing an alternative carbon feedstock for the chemical industry.[25,26]

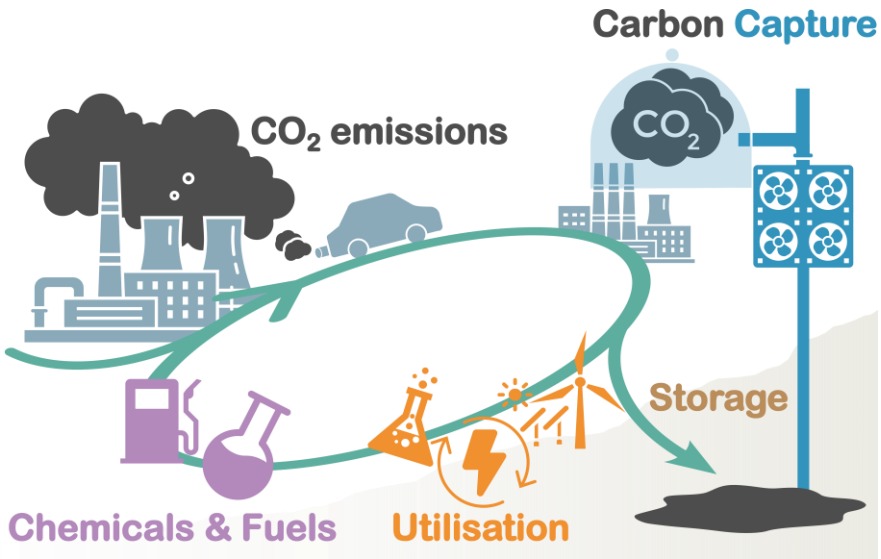

Figure 1.2 CCUS Carbon Cycle.

CCS and CCU commonly consist of two consecutive steps: (1) carbon capture (CC) and (2) subsequent storage or utilisation of the captured CO_2. In the first step, CO_2 can either be captured from flue gas waste streams at stationary sources with high CO_2 concentrations (industry)[27] or directly from the air (Direct Air Capture, DAC).[28] In an industrial context, carbon capture can take place pre- or post-combustion.[29] Generally, CO_2 is separated from a mixed gaseous stream by means of physical solvent absorption (mainly used for pre-combustion CC) or chemical absorption (mainly used for post-combustion CC), which involves a reaction of CO_2 with the chemical solvent to form a weakly bound intermediate. Aqueous amine (monoethanolamine, MEA or diethanolamine, DEA) solutions and liquid ammonia are used for the chemical absorption of CO_2.[27] Afterwards, a pressure or temperature swing is applied to release the absorbed CO_2 from the solvent, before storing it as a highly pressurised pure gas.[30] Other post-combustion CC technologies include physical- or chemical adsorption, cryogenic distillation and membrane separation.[29,31]

In the second step, the captured CO_2 can be stored (CCS) in geological formations for long-term sequestration[31] or utilised (CCU), either directly or as a feedstock for various value-added applications. Direct usages of captured CO_2 include, among others, enhanced oil and gas recovery, use in the food and beverage industry or usage as a solvent, refrigerant or protecting gas. Finally, recovered CO_2 can be recycled into a wide variety of industrially valuable products by means of carboxylation or reduction reactions.[18] Several promising technologies, such as the thermocatalytic-,

plasma catalytic-, photocatalytic- and electrocatalytic CO_2 conversion are currently being investigated,[32,33] the latter being the main topic of this dissertation. Additionally, most of these technologies can be operated flexibly, making them capable of balancing the energy grid and high levels of intermittent renewable energy in the so called Power-to-X approach.[18]

1.2 Electrocatalytic carbon dioxide conversion

1.2.1 An introduction to the electrochemical CO_2 reduction

The electrochemical CO_2 reduction (eCO_2R) enables the conversion of CO_2 into more reduced chemical species/value-added products, by applying electrical energy.

Over the past decades, the eCO_2R into industrially valuable products has become one of the most promising technologies to valorise anthropogenic CO_2 emission, while simultaneously providing a means of energy storage for intermittent renewable sources, such as wind-, solar- and hydro energy.[34–37] The eCO_2R benefits from the fact that it can be carried out at ambient temperature and pressure, while water and renewable electricity, from the aforementioned intermittent sources, provide a renewable feedstock.[38] Furthermore, a variety of products (Figure 1.3), such as formic acid/formate (FA, $HCOOH/HCOO^-$), carbon monoxide (CO), methane (CH_4), methanol (CH_3OH), ethylene (C_2H_4), etc., can be obtained with a relatively high rate of formation.[39–41] Careful tuning of the electrocatalytic cathode material, reaction conditions (including electrolyte, applied potential, etc.) and electrolyser configuration allow for a tailored electrochemical CO_2 reduction towards a desired product.[42,43]

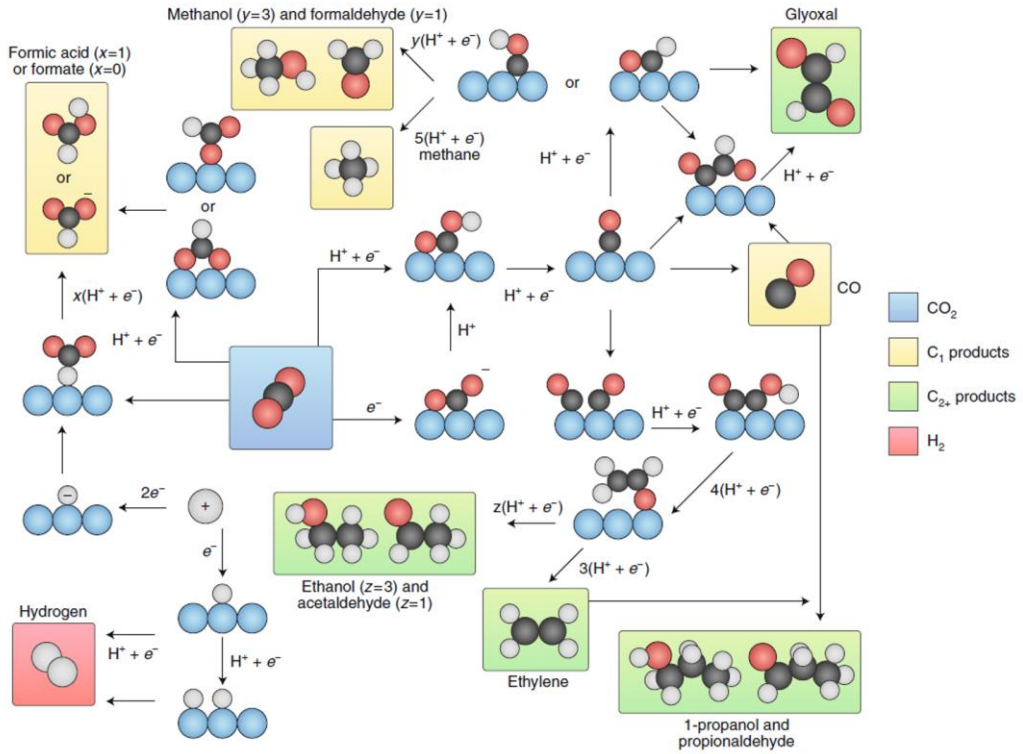

Figure 1.3 Overview possible reaction pathways for the eCO_2R towards different products. Black, red, white and blue spheres symbolize carbon, oxygen, hydrogen and a (metal) electrocatalyst, respectively.[40]

Even though the market price and -size of both CO and FA are the lowest, compared to other possible eCO_2R products,[44] both processes are considered to be industrially feasible as their estimated production costs of US\$0.44 kg^{-1} and US\$0.59 kg^{-1} for CO and FA, respectively, are competitive with their conventional production process.[45,46] According to most eCO_2R literature and techno-economic assessments (TEA), the eCO_2R towards formate/formic acid (FA), a 2-electron transfer liquid product, and CO as gaseous product, currently have the potential to generate the highest revenue per mole of consumed electrons.[47–49] Utilising cheap and earth abundant metals with a high overpotential for the

competing hydrogen evolution reaction (HER), FA can be produced with high Faradaic efficiencies (FEs), at moderate overpotentials.[50] Currently, a variety of formic acid concentrations, ranging from 85, 90, 95 and 98 to 99 wt%, are commercially available with 85 wt% being the most common.[51,52] Typical applications of industrially produced (>85 wt%) FA include, utilisation in food chemicals, pharmaceuticals and textiles, due to its strong acidic nature and reducing properties. Nonetheless, more diluted formic acid feedstocks (<50 wt%), as obtained by the eCO_2R, may be directly utilised as energy carrier in emerging applications such as the direct formic acid fuel cell (DFAFC) or as a liquid hydrogen, CO or CO_2 carrier, making it an excellent and versatile target product for the eCO_2R, which explains why it's the desired product in this dissertation.[51–55]

At the moment, electrocatalytic materials for the eCO_2R can be divided into three major groups: metals (noble and non-noble), metal-organic complexes (molecular catalysts) and carbon-based metal-free electrocatalysts.[56] Heterogeneous metal electrocatalysts are advantageous because of their superior electrocatalytic activity in combination with a low toxicity and facile synthesis methods. This large group can be subdivided into: monometallic electrocatalysts, multimetallic alloys and/or core-shell structures and inorganic metal compounds such as metal oxides, metal chalcogenides and metal carbides.[57]

In 1993, Hori *et al.* categorised various monometallic electrodes according to their predominant eCO_2R products.[58]

I.	Sn, Pb, Hg, In, Cd and Tl	($HCOO^-$)
II.	Au, Ag, Zn, Pd and Ga	(CO)
III.	Cu	(hydrocarbons and alcohols)
IV.	Ni, Fe, Pt and Ti	(H_2, inactive for eCO_2R)

Transition metals, such as Au, Ag and Cu preferably bind CO_2 via the carbon atom, whereas post-transition metals such as Sn and Bi tend to bind CO_2 via the oxygen atoms, explaining their selectivity towards formic acid. It is argued that •OCHO is most likely the key intermediate in formic acid production, while •COOH proceeds towards the formation of CO.[40,59]

Since Hori's pioneering work in 1993, multiple additional metal electrocatalysts, such as Bi, Co and Sb have been found to be selective for the eCO_2R towards FA.[50,60] While Pb, Hg, Cd and Tl are harmful to the environment and have a high toxicity, Co and Sb-based electrocatalysts have only recently gained attention and are still in the early stages of research.[60] Unlike the aforementioned electrode materials, Bi-, In- and Sn-based electrocatalysts all have a low toxicity and are environmentally friendly.[61] Bulk indium was first reported by Hori *et al.*[58] to be able to selectively convert CO_2 to FA with a FE_{FA} of 94.9% at -1.06V vs RHE. Although, compared to Bi- and Sn-based electrocatalysts, In electrodes are more expensive due to the scarcity and scattered distribution of In in the Earth's crust,[62] some believe that they are still a potential electrode material for the industrial eCO_2R towards FA.[60,61] The electrochemical performance of bismuth was first described by Hara *et al.*[63] in 1995 when they reported a FE_{FA} of 82.7% at -0.72 V vs RHE, and has only recently

(2016) regained the interest of the scientific community for the selective electrocatalytic conversion of CO_2 towards FA.[61] Similar to In, bulk Sn was first reported by Hori *et al.*[58] in 1993. While both Bi and Sn are also considered scarce materials, the estimated ultimately available resources for both metals are 20 and 300 Mt, respectively, making Sn more abundant than Bi.[64] Even though Bi-based catalysts currently outperform Sn-based electrocatalysts in terms of stability, Sn-based catalysts are still believed to be viable alternatives if an extended stability of over 80 000 hours can be achieved.[44,65]

Due to their high selectivity (FE%), low toxicity, non-noble nature, ecological and inexpensive properties, Sn-based electrocatalysts are an interesting candidate for the eCO_2R towards FA[66] and improving their stability was the main target set out for this dissertation.

1.2.2 State-of-the-art Sn-based electrocatalysts

As a result, Sn-based electrocatalysts have been studied extensively in the past decade.[66] A wide variety of Sn-based electrocatalysts such as bulk Sn, Sn nanoparticles, Sn-based alloys and core-shell nanoparticles, Sn oxides, -sulphides and other carbon supported Sn-based catalysts have been reported for the eCO_2R towards formic acid.[67–70] Table 1.1 provides a comprehensive overview of some of the best performing Sn-based electrocatalysts for the eCO_2R towards FA with their reported FE_{FA} (%), operating potential (V vs RHE), current density (J) and longest stable operation time, with negligible FE_{FA} decrease, denoted as stability (h).

The best performing Sn-based electrocatalysts from this dissertation (Chapter 5 - 7) have also been included in table 1.1 (in bold), for comparison with the state-of-the-art.

Table 1.1 State-of-the-art Sn-based electrocatalysts.

Catalyst	FE_{FA} (%)	Potential (V) vs RHE	J (mA cm^{-2})	Stability (h)	Electrolyte	Ref
$Bi_{0.1}Sn$*	95	-0.75	100	2400	1.0 M $KHCO_3$	71
Sn nanoparticles GDE*	94	-1.48	140	550	DI water	72
SnO_2 GDE*	70	-1.40	12	174	0.1 M $KHCO_3$	73
FTO/C*	≈90	-0.80	100	168	1.0 M $KHCO_3$	74
SnO_2/γ-Al_2O_3	65	-1.37	21.7	152	0.5 M $KHCO_3$	75
P-Sn/SnO_x*	90	-0.97	192.5	120	1.0 M KOH	76
Bi-Sn/CF	96	-1.14	45	100	0.5 M $KHCO_3$	77
SnDT GDE*	62.5	-0.76	18.7	72	1.0 M $KHCO_3$	78
SnIn-3	84.6	-1.0	39	58	0.1 M $KHCO_3$	79
np-Sn/SnO_2	80	-1.1	16	58	0.5 M $NaHCO_3$	80
p-SnS_x	97	-1.0	15	50	0.1 M $KHCO_3$	81
$CuSn_3$	95	-0.5	33	50	0.1 M $KHCO_3$	82
$Sn_{0.80}Bi_{0.20}$@Bi-SnO_x*	>90	-0.88	20.9	50	0.5 M $KHCO_3$	83
Sn quantum sheets/GO	85	-1.16	21	50	0.1 M $KHCO_3$	84
SnO_x NP-s*	81	-1.20	9.03	50	0.1 M $KHCO_3$	85
CuSn-10C	82	-1.0	18.9	42	0.1 M $NaHCO_3$	86
Sn(S)/Au	93	-0.75	55	40	0.1 M $KHCO_3$	87
$Sn_{2.7}Cu$ GDE*	90	-0.55	243.1	40	1.0 M KOH	88
Cu_1Sn_3-CC	88.35	-0.8	16	36	0.5 M $KHCO_3$	89

3D SnO_2 nanospheres	68	-1.2	45	35	0.1 M $KHCO_3$	90
SnO_2/CC	87	-0.97	50	24	0.5 M $NaHCO_3$	91
Pom. SnO_2@C*	85	-0.70	100	24	0.5 M $KHCO_3$	**
Pom. SnO_2*	83	-0.62	100	24	0.5 M $KHCO_3$	**
$Ag_{76}Sn_{24}/SnO_x$	80	-0.8	19.7	24	0.5 M $NaHCO_3$	92
Commercial SnO_2*	79	-0.50	100	24	0.5 M $KHCO_3$	**
3D SnO_2 nanospheres*	75	NR	500	24	0.4 M K_2SO_4	90
Sn-CF1000	63	-0.8	16.6	24	0.5 M $KHCO_3$	93
Sn-N-OMC (2)*	62	-0.54	100	24	0.5 M $KHCO_3$	**
Sn_9Sb_1 film*	92.7	-1.25	4.2	22	0.1 M Na_2SO_4	94
GDE-$In_{0.9}Sn_{0.1}$	92	-1.2	15	22	0.1 M $KHCO_3$	95
Bi_5Sn_{60}	94.8	-1.0	34.0	20	0.1 M $KHCO_3$	96
SnS_2@SnO_2*	92.2	-0.86	200	20	1.0 M KOH	97
SnCu-CNS	90	-0.9	6	20	0.1 M $KHCO_3$	98
$SnO_{x(100-8)}$	87.1	-1.17	11	20	0.5 M $KHCO_3$	99
Reduced nano-SnO_2/graphene	93.6	-1.16	10.2	18	0.1 M $NaHCO_3$	100
NW-SnO_2	87.4	-1.0	22	18	0.5 M $KHCO_3$	101
Sn dendrite	71.6	-1.36	17.1	18	0.1 M $KHCO_3$	102
OD-Sn-Pb-Sb	91	-1.4	8.3	16	0.1 M $KHCO_3$	103
TNS-2.0-SnO_2	73	-1.6	10	16	0.1 M $KHCO_3$	104
Cu@Sn	100	-0.93	16.52	15	0.5 M $KHCO_3$	105
Sn-pNW	80	-0.8	6	15	0.1 M $KHCO_3$	106
Cu_6Sn_5/Sn	87.2	-0.95	28.69	14	0.5 M $NaHCO_3$	107

SnS_2/rGO	84.5	-0.77	13.9	14	0.5 M $NaHCO_3$	108
ZnSn	94	-1.06	13	12	0.5 M $KHCO_3$	109
$Zn_xSn_yO_z$-CNTs-4*	94	-1.1	75	12	0.5 M $KHCO_3$	110
BM Sn-Cu	92	-0.95	10.8	12	0.1 M $KHCO_3$	111
Mesoporous Sn/SnO_x	89.6	-1.2	11.2	12	0.1 M $KHCO_3$	112
SnO_2/Bi_2O_3	80	-1.0	3.5	12	0.1 M $KHCO_3$	113
SnO_2 NP*	90	NR	150	11	0.4 M K_2SO_4	114
Sn-Cu alloy	82.3	-1.14	79	11	0.5 M KCl	115
Sn/SnO_2-2h	78.8	-1.0	30	11	0.5 M $KHCO_3$	116
Sn@-PANI/NF	94	-1.14	19	10	0.1 M $KHCO_3$	117
In_3Sn/C	92.9	-1.0	1	10	0.1 M $KHCO_3$	118
Sn/CN-0.1	>92	-0.9	3.8	10	0.1 M $KHCO_3$	119
SnO_2/PC	92	-0.86	29	10	0.5 M $KHCO_3$	120
Cu@Sn nanocones	90.4	-1.1	57.7	10	0.1 M $KHCO_3$	121
Sn/CP-UPED	89	-1.1	6.0	10	0.1 M $KHCO_3$	122
SnO_2⊃NC@EEG	81.2	-1.2	11	10	0.1 M $KHCO_3$	123
CuSn NPs/C-A	71.5	-1.0	12.6	10	0.1 M $KHCO_3$	124

**measurements performed in an electrolyser, ** this work*

All potentials were converted to the RHE scale using the following formula and values ($E_{RHE} = E_{ref} + 0.0591 \cdot pH + E^0_{(ref)}$; $E^0_{SHE} = 0.000$ V vs SHE; $E^0_{Ag/AgCl\ (KCl\ sat.)} = +0.197$ V vs SHE; $E^0_{SCE\ (KCl\ Sat.)} = +0.241$ V vs SHE; $pH_{0.1\ M\ bicarbonate\ electrolyte} = 6.80$; $pH_{0.5\ M\ bicarbonate\ electrolyte} = 7.30$). (NR = not reported)

A vast majority of these state-of-the-art Sn-based electrocatalysts have already been discussed extensively in recent review articles.[50,66,67,125] However, it should be noted that excellent Sn-based electrocatalysts with a high selectivity (FE_{FA}) and activity (J), could not be relevant at higher

technology readiness levels (TRLs) if their stability remains insufficient. In industry, electrocatalyst activity and selectivity are usually subsidiary to a prolonged electrocatalyst lifetime. Furthermore, the overpotential and thus operating potential should be as low as possible in order to limit the required amount of electricity and increase the energy efficiency of the overall process.[65]

For Sn-based electrocatalysts to become industrially viable, Kibria *et al.*[44] demonstrated that several figures of merit should be attained. Assuming an estimated CO_2 cost of US\$40 t^{-1}, an electrolyser cost of US\$5000-15000 m^{-2} and a separation cost of US\$60 t^{-1}, they calculated that a prolonged (>80 000h) and stable operation with a selectivity (FE_{FA}) towards FA of 80 - 90% at current densities >300 mA cm^{-2} should be obtained at a cell voltage bellow 1.8 V.[44] To date, as evidenced in Table 1.1, this impeccable and industrially viable Sn-based electrocatalyst has yet to be invented.

At present, several highly selective Sn-based electrocatalysts have been reported to reach a FE_{FA} of approximately 100%,[105] with nearly all state-of-the-art Sn-based electrocatalysts exhibiting a selectivity >80%. Simultaneously, others have reported catalysts performing at higher current densities up to 500 mA cm^{-2}. Chen *et al.*[114] described a carbon-supported SnO_2 nanoparticle electrocatalyst with a FE_{FA} of 90% at 500 mA cm^{-2} on a 25 cm^2 gas diffusion electrode (GDE). Unfortunately, the stability of their electrocatalyst was only assessed for 11 h at a lower current density of 150 mA cm^{-2}, where it already revealed significant

changes in the agglomerate size and aspect ratio.[114] Nguyen-Phan *et al.*[90] reported a similarly active 3D hollow SnO_2 nanosphere electrocatalyst with an average FE_{FA} of 75 ± 6% over 24 h of electrolysis at 500 mA cm^{-2}.[90] While both selectivity and activity currently reach high and industrially relevant values, the stability (long-term performance) of these state-of-the-art Sn-based electrocatalysts remains inadequate.

Looking at the long-term performance of these state-of-the-art Sn-based electrocatalysts (Table 1.1), only eight have a minimum reported stability of 72 hours.[71–78] Lim *et al.*[78] described an electrochemically deposited Sn catalyst with dense tips (SnDT) on a gas permeable carbon cloth electrode, which was able to achieve a formate productivity of 65 mg h^{-1}. No changes in FE_{FA} (62.5%) or current density were observed during 72 h of operation at -0.76 V vs RHE. More importantly, the nanostructure of the SnDT remained largely intact after 72 h of electrolysis.

Wen *et al.*[77] reported a promising and durable Bi-Sn bimetallic electrocatalyst which also showed no apparent signs of degradation after 100 h. This prolonged durability has been ascribed to the strong anchoring of the Bi-Sn electrocatalyst to the carbon fabric supporting material.[77] A similar strategy has been described by Kim *et al.*,[75] who designed a leaching resistant SnO_2/ɣ-Al_2O_3 electrocatalyst. In their research, they found that the strong interaction between the ɣ-Al_2O_3 supporting material and SnO_2 electrocatalyst attributed to retain its morphology, crystallinity, size and electrochemical performance after 152 h of electrolysis.[75] Another

interesting Sn-based electrocatalyst has been reported by Cheng *et al.*[76] to yield a stable performance of 120 h, maintaining a FE_{FA} of ≈90%. The excellent stability of their phosphorus-modified Sn/SnO_x core/shell electrocatalyst is presumably attributed to the surface phosphate groups stabilizing the active sites by acting as a physical and/or chemical barrier, inhibiting SnO_x surface dissolution. Moreover, the Sn/SnO_x core/shell structure was maintained and the contact angle decreased only slightly over an extended period of 120 h.[76] Additionally, Ko *et al.*,[74] describe a fluorine-doped-SnO_2 (FTO) electrocatalyst with a superior FE_{FA} of ≈90% and a stable performance for 7 days at 100 mA cm^{-2}. The fluorine doping has been confirmed, based on DFT calculations, to simultaneously enhance the interaction between $HCOO^-$ and the FTO surface and to modify the electronic structure of CO_2, which facilitates electron transfer. The enhanced stability is also attributed to this fluorine dopant, which plays an important role in the stabilisation of the Sn oxidation state, by forming strong F-Sn bonds, as confirmed by i*n operando* spectroscopy.[74]

Wu *et al.*[73], on the other hand, mentioned SnO_2 nanoparticles of ≈3 nm, supported on a GDE, that exhibit an excellent stability of 174 h, maintaining a FE_{FA} of 70%. Sadly, their stability measurement was performed at a low current density of ≈12 mA cm^{-2}, which is far from the prerequisite current density of >300 mA cm^{-2}, calculated by Kibria *et al.*[44] A more promising and industrially relevant electrochemical performance has been reported by Yang *et al.*[72] Their three-compartment electrochemical formic acid cell exhibited a stable performance for more

than 550 h, utilising a Sn nanoparticle coated GDE with a FE_{FA} of 94% and a current density of 140 mA cm^{-2}.[72] The longest reported stable Sn-based electrocatalyst for the eCO_2R towards FA, to date, has been reported by Li *et al.*[71] Their homogeneously alloyed $Bi_{0.1}Sn$ crystals exhibit a remarkable FE_{FA} of 95% at an overpotential of ≈-0.65 V during a continuous operation at 100 mA cm^{-2} for more than 100 days. While there is no obvious degradation reported for these state-of-the-art Sn-based electrocatalysts, their long-term stability above 2400 hrs remains unclear.

Looking back at the predetermined industrial goals[44] of a prolonged and stable (>80 000h) operation with a FE_{FA} of 80 - 90% at current densities >300 mA cm^{-2}, we are able to conclude that the required selectivity has already been achieved at moderate current densities (≈100 mA cm^{-2}). Sn-based electrocatalyst stability, on the other hand, is still a long way from the targeted 80 000 hours of operation. However, once this prolonged stability has been attained, the eCO_2R towards formate is expected to reach pilot scale. Moreover, Sn-based electrocatalysts are believed to be a viable option and electrocatalyst stability appears to be a crucial piece to the puzzle as lifetimes in the range of several thousands of hours should be reached.[65,126] This clearly establishes the necessity and usefulness of the performed research, in order to transpose the eCO_2R towards FA towards a higher TRL. Finally, it introduces the main goal of this dissertation, enhancing the electrocatalytic stability of Sn-based catalysts, which will be further elucidated in the following chapter (Chapter 2; Scope and outline) and the remainder of this dissertation.

Chapter 2

Scope and outline

In the following chapter, the scope, strategy, objectives and outline of this dissertation will be enlightened.

2.1 Objectives

The general introduction of chapter 1 clearly demonstrates the critical nature of our changing climate and highlights the ever growing need for carbon dioxide abatement. The eCO_2R towards formic acid provides an interesting approach to valorize CO_2, closing the carbon cycle, and simultaneously providing an energy storage for intermittent renewable sources, such as wind-, solar- or hydro energy.

Despite the development of numerous excellent and highly selective state-of-the-art Sn-based electrocatalysts for the eCO_2R towards FA, pilot scale application is currently hampered by an insufficient electrocatalyst stability. The main objective of this dissertation is therefore to bring the electrocatalytic conversion of CO_2 to FA towards an industrial feasibility by increasing the stability of Sn-based electrocatalysts. To achieve this goal, we need to develop an in-depth knowledge and understanding concerning the major degradation pathways of Sn-based electrocatalysts, and explore the possibilities of several mitigation strategies. Moreover, attention will be given to the influence of the supporting material on the stability and electrochemical performance of Sn-based electrocatalyst, in an endeavour to attain a more stable Sn-based electrocatalyst with a selectivity of $>80\%$ at an industrially relevant current density ≥ 100 mA cm^{-2}.

2.2 Strategy

In pursuit of prolonged Sn-based electrocatalyst stability, firstly a comprehensive literature review was performed to (I) elucidate the most common degradation mechanisms that impair long-term electrocatalytic activity of state-of-the-art Sn-based electrocatalysts, (II) to explore the possibilities of a variety of mitigation strategies, and (III) to gather insights into stability issues related to Sn-based electrocatalysts and CO_2 electrolysers.

The electrochemical performance of the Sn-based electrocatalysts was evaluated by means of an in-house designed small (1 cm^2) flow-by CO_2 electrolyser. In this dissertation, we have opted for a flow-by configuration (Figure S5.4) in order to diminish instability issues originating from the CO_2 electrolyser, such as the formation and deposition of salts (carbonate) or mechanical membrane degradation. As a consequence, we were able to assess the long-term stability of our Sn-based electrocatalysts under industrially relevant operating conditions.

Additionally, *ex situ* physicochemical characterisation techniques, such as nitrogen physisorption (N-sorption), X-ray powder diffraction (XRD), advanced electron microscopy (SEM and (S)TEM), X-ray photoelectron spectroscopy (XPS), Raman spectroscopy and inductively coupled plasma optical emission spectroscopy (ICP-OES) were employed to completely elucidate the degradation of these Sn-based electrocatalysts and to explain observations in their electrochemical behaviour.

The combination of extensive electrochemical testing and rigorous physicochemical characterization leads to an in-depth understanding concerning structure-performance correlations, which aids in predicting and understanding the electrocatalytic behaviour. Finally, this helps in unravelling and eventually counteracting the major degradation pathways, in order to arrive at a (semi-)stable electrocatalytic system.

2.3 Outline

This doctoral dissertation has been divided into 8 chapters, through which you will be taken on a journey through my PhD. A schematic overview of the outline is presented in Figure 2.1.

Starting with chapters 1 & 2, a general introduction which outlines the framework, objectives and strategy of my PhD is provided. After highlighting one of the biggest scientific challenges of the 21st century, climate change, the urgent need for carbon dioxide sequestration via CCUS is demonstrated. Finally, the electrochemical CO_2 reduction towards formic acid is introduced as a promising technology and the need for stable Sn-based electrocatalysts is emphasised.

Next, chapters 3 & 4 convey several theoretical considerations concerning the guiding principles behind electrocatalysis and the long-term electrocatalytic stability of Sn-based electrocatalysts. Chapter 3 enables the readers to understand the underlying phenomena of electrocatalysis, while simultaneously applying them to the eCO_2R towards FA.

Additionally, various important figures of merit to quantify the electrochemical performance of electrocatalysts are introduced.

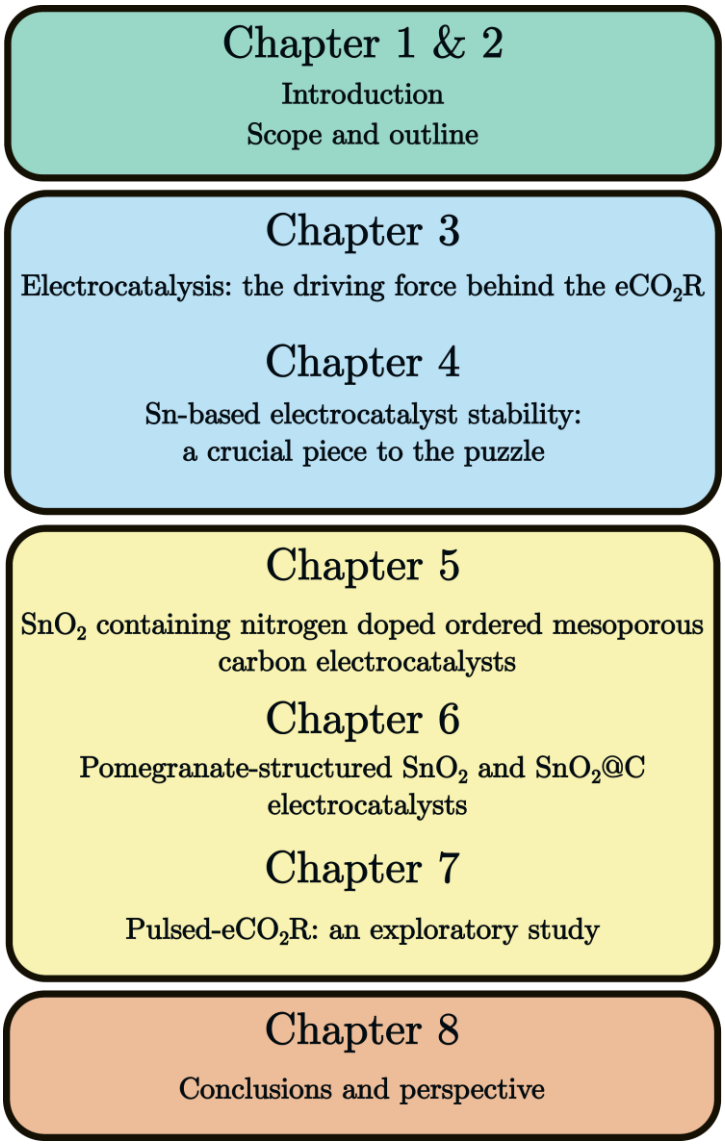

Figure 2.1 Dissertation outline

A more in-depth review regarding the stability of Sn-based electrocatalysts is given in chapter 4. Here, we attempt to elucidate the major degradation pathways that impair long-term electrocatalytic performance, while

simultaneously exploring the possibilities of a variety of mitigation strategies, and gathering insight into stability issues related to Sn-based electrocatalysts and CO_2 electrolysers.

Chapters 5 to 7 are a collection of all experimental endeavours during my PhD. Firstly, in chapter 5, SnO_2 was incorporated into a more open, carbon based supporting material (N-doped ordered mesoporous carbon) in an attempt to significantly increase the stability by inhibiting agglomeration and nanoparticle detachment. Another type of Sn-based electrocatalyst (pomegranate structured SnO_2 & SnO_2@C nanoparticles) was synthesised in chapter 6. These pomegranate SnO_2 electrocatalysts, with a FE_{FA} above 80%, are able to compete with most of the current state-of-the-art Sn-based electrocatalysts and highlight the promising possibilities of a particle confinement strategy to enhance electrocatalytic stability for future electrocatalyst design. While we were able to slow down irreversible morphological changes, the *in situ* reduction of SnO_2 to Sn^0 continues to impede prolonged electrocatalyst stability. Following these results, an exploratory study of pulsed-eCO_2R was performed in chapter 7 in an attempt to further increase the (electrochemical) stability of Sn-based electrocatalysts by diminishing *in situ* SnO_2 reduction.

Finally, in chapter 8 a general conclusion is presented, connecting all chapters. In addition, a perspective on future research, to bring the electrocatalytic conversion of CO_2 to FA towards an industrial feasibility by increasing the stability of Sn-based electrocatalysts, is given.

Chapter 3

Electrocatalysis: the driving force behind the eCO_2R

The guiding principles behind electrocatalysis will be explained and applied to the electrochemical CO_2 reduction. Furthermore, several important figures of merit will be introduced to evaluate the electrochemical performance of electrocatalysts.

3.1 The guiding principles of electrocatalysis

The word "electrocatalysis" is an amalgamation of electrochemistry and catalysis, from the Greek word *katalyein* "to dissolve" (*kata* "down", *lyein* "to loosen"). Electrochemistry interconverts electrical and chemical energy, while catalysis alters (increases or decreases) the rate of a chemical reaction.[127,128] Similar to a catalyst, an electrocatalyst participates in an electrochemical reaction, without being consumed, modifying the rate of the electrochemical reaction at an electrode surface.[129]

Nowadays, electrocatalysis is becoming increasingly important to enhance the sustainability of our human society. Several technologies, such as fuel cells, water electrolysis, the electrochemical synthesis of next-generation fuels from CO_2, energy storage (batteries) and sensors all rely on efficient electrocatalysts.[130] In this chapter the guiding principles behind electrocatalysis will be explained and applied to the electrochemical CO_2 reduction.

3.1.1 Conquering the energy barrier

The energy barrier or activation energy (E_a) is defined as the minimum amount of energy needed to activate molecules or atoms so that they can undergo a chemical (or electrochemical) reaction from reactant to product. In electrochemistry, the E_a is a function of an electrical variable, such as the cell potential (E_{cell}) or the overpotential (η) of the overall electrochemical reaction.[131] It is this energy barrier that is influenced by the electrocatalyst (Figure 3.1), which in conjunction reduces the operating

potential at which the electrochemical reaction occurs. Figure 3.1 illustrates this as it shows the E_a, for an uncatalysed and a catalysed reaction, as a function of the potential energies of the reactants and products.[129,131]

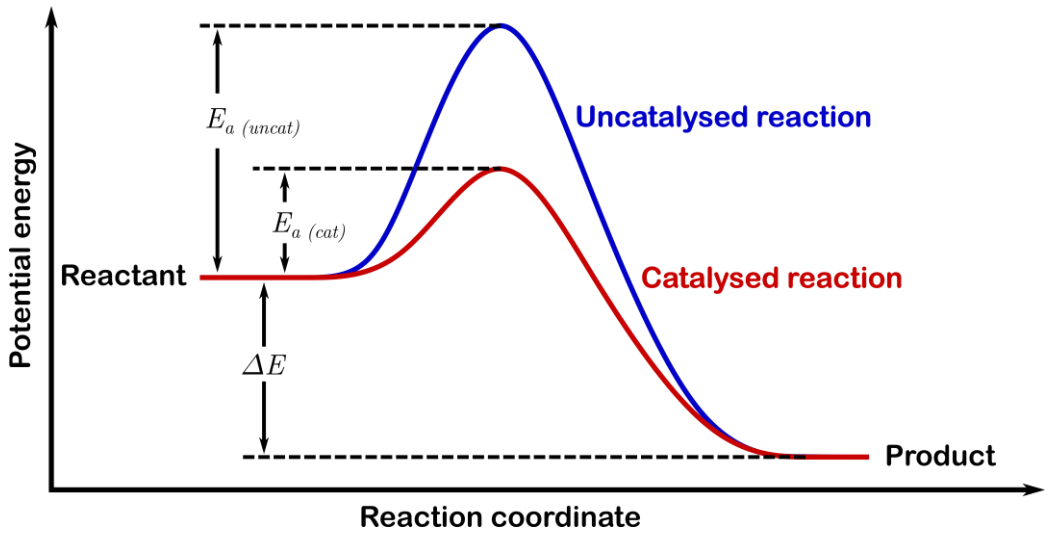

Figure 3.1 Activation energy of an uncatalysed and a catalysed reaction. (Redrawn from ref.[129])

An overall electrocatalytic process involves one (or multiple) cathodic reduction reaction(s) and one (or more) anodic oxidation process(es), which take place in opposing directions, in order to assure electroneutrality.[132] Aside from homogeneous redox reactions, these half-reactions are typically separated in space, occurring at opposing electrodes. Depending on the cell configuration, these half-reactions occur in two compartments, separated by an ion-exchange membrane in order to prevent mixing of the cathodic and anodic reaction products.[127,132] Whenever the sum of the free energy changes at both electrodes is negative, the electrochemical process will occur spontaneously (galvanic) and the

released electrical energy can be harvested. Opposite, when the change in free energy is positive, external electrical energy needs to be supplied in order to force (electrolysis) the electrochemical process to take place and convert electrical energy into chemical energy.[132,133]

3.1.2 Electron transfer in different classes of electrocatalysis

For the eCO_2R, multiple types of electrocatalysts, including homogeneous catalysts in solution or immobilized on the electrode surface and heterogeneous electrocatalysts have been explored.[134] A general scheme for the homogeneous- and heterogeneous electrocatalytic CO_2 reduction is depicted in figure 3.2.

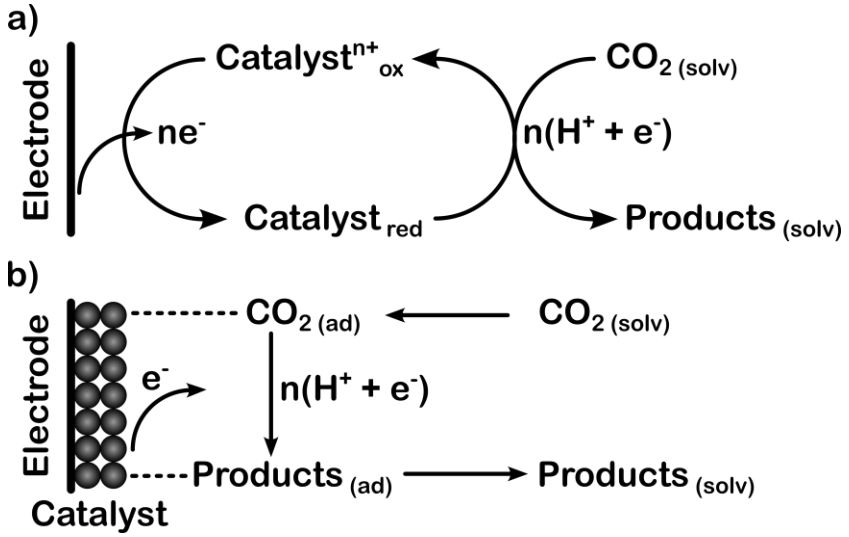

Figure 3.2 Schematic representation of a) homogeneous electrocatalytic CO_2 conversion and b) heterogeneous electrocatalytic CO_2 reduction. (Adapted from ref.[134])

A homogeneous electrocatalyst, typically an organic metal complex, is present in the same phase as the reactants, i.e. in solution. Generally, the metal complex accepts electrons from the electrode, which is typically

inert, before donating them to the CO_2 in solution and returning to its initial state. The homogeneous metal complex electrocatalyst acts as a redox (reduction-oxidation) shuttle between the electrode and dissolved CO_2, with the overall reaction being an indirect electrolysis of CO_2. Notwithstanding their excellent selectivity and activity, the non-recyclable character and high cost of homogeneous electrocatalysts currently impede their application for the industrial eCO_2R. Alternatively, these homogenous organic metal complex electrocatalysts can be immobilized on the electrode by surface binding, combining the advantages of homogeneous electrocatalysis and enabling them to be recycled.[134–136]

In this dissertation, high surface area heterogeneous Sn-based electrocatalysts are developed and used for the eCO_2R. Contrary to the homogeneous electrocatalysed CO_2 reduction, the heterogeneous electrocatalytic CO_2 conversion occurs at the electrode-electrolyte interface.[134] Considering the general eCO_2R reaction (Eq. 3.1) at a heterogeneous electrocatalyst,[34] a series of steps, as presented in figure 3.3, facilitate the reduction of CO_2 towards value-added products.

$$kCO_2 + n(H^+ + e^-) \rightleftarrows P + mH_2O \qquad \text{(Eq. 3.1)}$$

Since the electrochemical reaction takes place in the proximity of the electrode surface, CO_2 has to diffuse (mass transfer), either through the electrolyte or through the GDE (in the case of an electrolyser) towards the electrode-electrolyte interface. Next, the reduction reaction is initiated by the adsorption of CO_2 on the electrode surface. As the CO_2 approaches the

cathode surface, according to most of the proposed reaction mechanisms, it bends from its linear 180° configuration in order to activate the carbon atom and form $CO_2^{\bullet-}$.[40,137,138] Following a series of proton-coupled electron transfers from the cathode to the CO_2, various intermediates and products are formed on the electrocatalyst surface. After the desorption of the final eCO_2R product, the reaction products migrate away from the electrode surface due to diffusion and the active site becomes available for a new CO_2 molecule.[66,133,139]

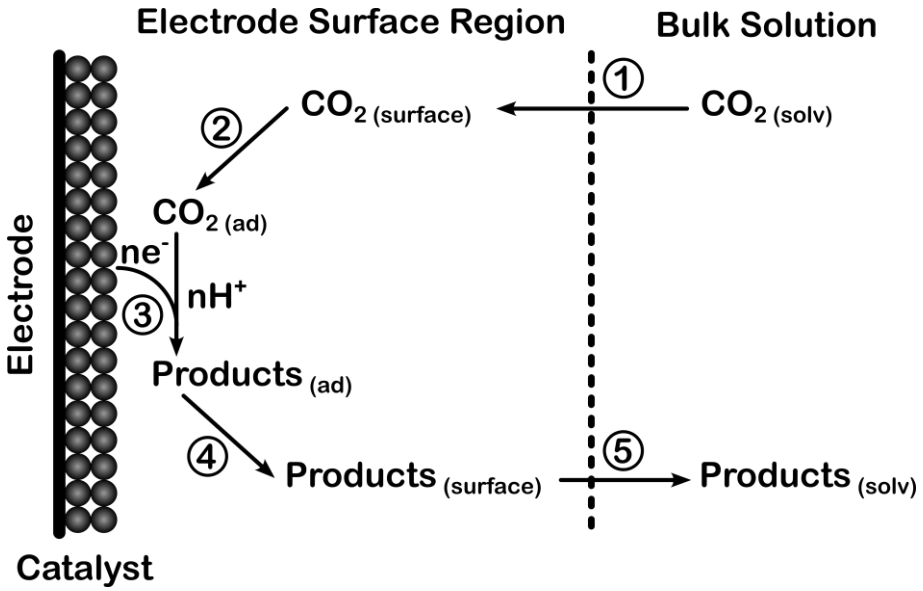

Figure 3.3 Simplified reaction steps of the eCO_2R at a heterogeneous electrocatalyst, with 1) diffusion, 2) adsorption, 3) charge transfer, 4) desorption and 5) diffusion. (Adapted from ref.[133]*)*

Given that the eCO_2R is a combination of several steps, the reaction rate (or current) of the overall reaction is dependent on the slowest one. This so-called rate-determining step (RDS) or rate-limiting step slows down the more facile or faster reactions due to the slow rate at which it creates or

disposes their reactants or products, respectively. The RDS can be any of the aforementioned processes, such as mass transfer, electrode transfer at the cathode surface, chemical reactions preceding or following the electron transfer or other surface reactions such as adsorption or desorption. Interestingly, the rate of some of these processes, such as the electron transfer or adsorption are potential dependent, while mass transfer is influenced by the reaction conditions and electrolyser configuration.[133]

In this dissertation, a small flow-by electrolyser and GDE (Figure S5.4) are used to enhance mass transfer and to be able to assess the electrochemical performance of the Sn-based electrocatalysts at industrially relevant operating conditions. In a flow-by electrolyser, it was generally accepted that the eCO_2R occurs at the triple-phase boundary (TPB) between the gaseous CO_2, liquid electrolyte and solid electrocatalyst.[140] Furthermore, the higher reaction rates, compared to an H-type electrochemical cell, were often ascribed to the presence of this TPB. Smith *et al.*,[141] however, recently argued that, even when using GDEs, the eCO_2R occurs at the two-phase interface, where gaseous CO_2 molecules reach the electrocatalyst's surface by dissolution and diffusion though the electrolyte present in the pores of the GDE. Nonetheless, mass transfer is still enhanced when working with GDEs, due to the CO_2 only having to diffuse a short distance from the gas phase through the liquid towards the electrocatalyst, which is why this configuration was chosen here to study the performance of Sn-based electrocatalysts at industrially relevant conditions.[141] An H-cell configuration would otherwise limit the

attainable current densities, without venturing into mass transfer limitation, to a couple tens of mA cm^{-2} (≈20 mA cm^{-2}).[142]

3.1.3 The electrical double layer

Whenever an electrocatalyst covered electrode is brought into contact with a liquid electrolyte, the application of a potential establishes an interfacial region with excess charge carriers of opposite charge on the electrode and in solution, that has been shown to behave as a capacitor.[133,143] This region is called the electrical double layer (EDL) and is typically described as an assembly of layers, depicted in figure 3.4.[143,144]

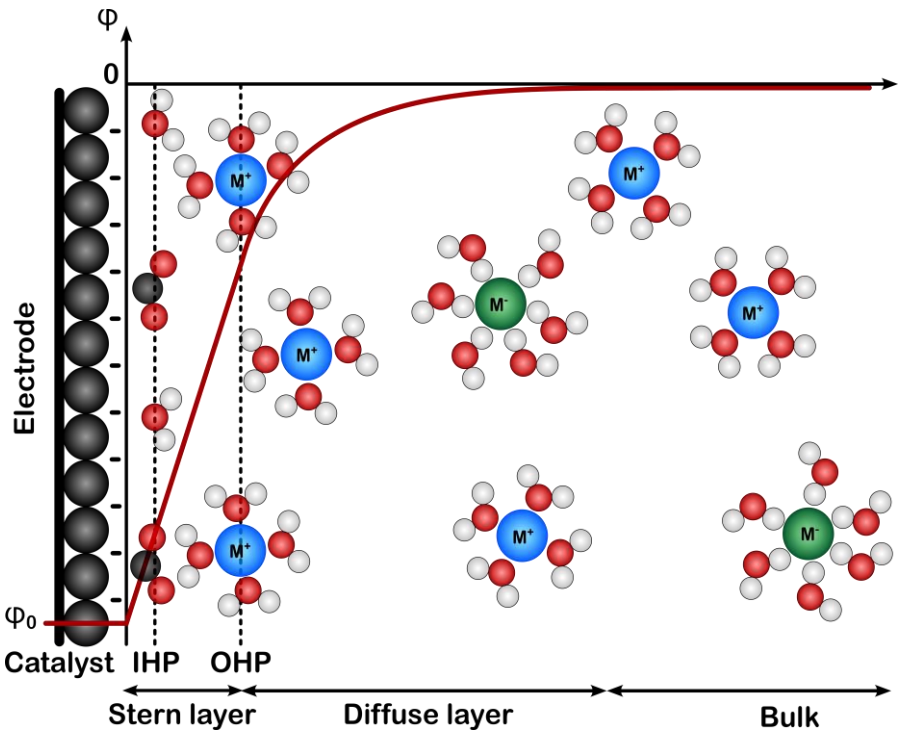

Figure 3.4 Schematic representation of the electrical double layer (Gouy-Chapman-Stern model). Black, red, white, blue and green spheres represent carbon/catalyst, oxygen, hydrogen, a cation and an anion, respectively. The red curve expresses the potential as a function of the distance from the electrode surface. (Redrawn from ref.[145]*)*

Closest to the electrode are specifically adsorbed species, such as solvent molecules, reactants, reaction intermediates, products and other specifically adsorbed molecules or ions. The locus of their electrical centres is called the inner Helmholtz plane (IHP). Adjacent to the IHP is the outer Helmholtz plane (OHP), which primarily consists of solvated ions with an opposite charge of the electrode. The OHP is the nearest these solvated ions, often referred to as non-specifically absorbed ions, can be drawn to the electrode via electrostatic forces.[143,144]

Next, the diffuse layer, as described by Gouy and Chapman, comprises loosely alternating layers of cations and anions counteracting the exponential decay of the potential and corresponding electrostatic force, away from the electrode, maintaining charge neutrality throughout the EDL. The diffuse layer, whose thickness depends on the total ionic concentration, extends from the OHP into the bulk of the electrolyte solution. On the far side of the diffuse layer is the bulk electrolyte, whose structure isn't affected by the electrode potential (φ_0).[133,143,144]

The total charge density of the entire EDL, including IHP, OHP and diffuse layer, is equal and opposite to that of the electrode.[143] During the eCO_2R, the working electrode is negatively biased, causing the EDL, formed as a consequence, to be enriched with solvated cations (Figure 3.4). The eCO_2R is an inner-sphere reaction, where the adsorption and bond rearrangement of the CO_2 and reaction intermediates occur within the IHP. Because of this, the electrocatalytic conversion of CO_2 is influenced by the potential-dependent structure of the solvent and behaviour of

electrolyte ions, reaction-induced concentration gradients and the EDL structure. As a result, previous studies have turned their attention towards the influence of different electrolytes, in an attempt to boost the eCO_2R. They have found that electrolyte concentration, species (type of cation), buffer capacity and pH value directly influence the local reaction conditions, which in turn impacts the electrocatalytic performance and the overall eCO_2R.[146–148] For example, large-size alkali cations have been observed to promote the activity and Faradaic efficiency of the eCO_2R on a number of catalysts.[127,145,149]

3.1.4 Reaction pathways for the two-electron eCO_2R

As previously mentioned, a wide variety of value-added chemicals can be produced by the eCO_2R. Table 3.1 provides an overview of the most common half-reactions in neutral, aqueous media and their respective equilibrium potential.[34,66,150] Note that the eCO_2R requires the transfer of multiple electrons, which thermodynamically is highly unlikely to occur in a single step. According to an extension of the Marcus theory, the required activation energy to simultaneously transfer two electrons is already four times higher than that of a single electron transfer. Consequently, it is energetically more favourable to store charge in a reaction intermediate species.[151] The eCO_2R is therefore considered to be a multistep proton-electron reaction where n electrons and protons are transferred in at least n electrochemical steps, whether or not coupled to m chemical steps.[143]

Table 3.1 Possible eCO_2R reactions towards value-added chemicals.[34,66]

eCO_2R half-reactions	Potential V vs RHE at pH 7
$CO_2\,(g) + e^- \rightarrow CO_2^{*-}$	-1.48
$CO_2\,(g) + 2H^+ + 2e^- \rightarrow HCOOH\,(l)$	-0.25
$CO_2\,(g) + 2H^+ + 2e^- \rightarrow CO\,(g) + H_2O\,(l)$	-0.10
$CO_2\,(g) + 4H^+ + 4e^- \rightarrow HCHO\,(l) + H_2O\,(l)$	-0.07
$CO_2\,(g) + 6H^+ + 6e^- \rightarrow CH_3OH\,(l) + H_2O\,(l)$	0.02
$CO_2\,(g) + 8H^+ + 8e^- \rightarrow CH_4\,(g) + 2H_2O\,(l)$	0.17
$2CO_2\,(g) + 12H^+ + 12e^- \rightarrow C_2H_4\,(g) + 4H_2O\,(l)$	0.08
$2CO_2\,(g) + 12H^+ + 12e^- \rightarrow C_2H_5OH\,(l) + 3H_2O\,(l)$	0.09

Both the eCO_2R towards CO and FA are two-electron transfer reactions, which implies that they occur in at least two electrochemical steps with one (or more) reaction intermediate(s). Nowadays, three possible reaction pathways have been identified for the eCO_2R towards FA.[43] Figure 3.5 provides an overview of these possible reaction pathways for the eCO_2R towards $HCOO^-$ or HCOOH on Sn-based electrocatalysts in aqueous media. A first reaction pathway is presumed to proceed via a monodentate or bidentate reaction intermediate, where the intermediate is bound to the Sn-based electrode either through one oxygen atom or two oxygen atoms, respectively. These intermediates can be formed either through reaction with $^\bullet H$ via CO_2 insertion into the metal-hydrogen bond (Figure 3.5A) or via direct protonation with H^+ from the electrolyte (upper pathway Figure 3.5B). Alternatively, a $CO_2^{\bullet-}$ radical could react with a neighbouring proton or water to form $HCOO^-$ or HCOOH (Figure 3.5B).[43]

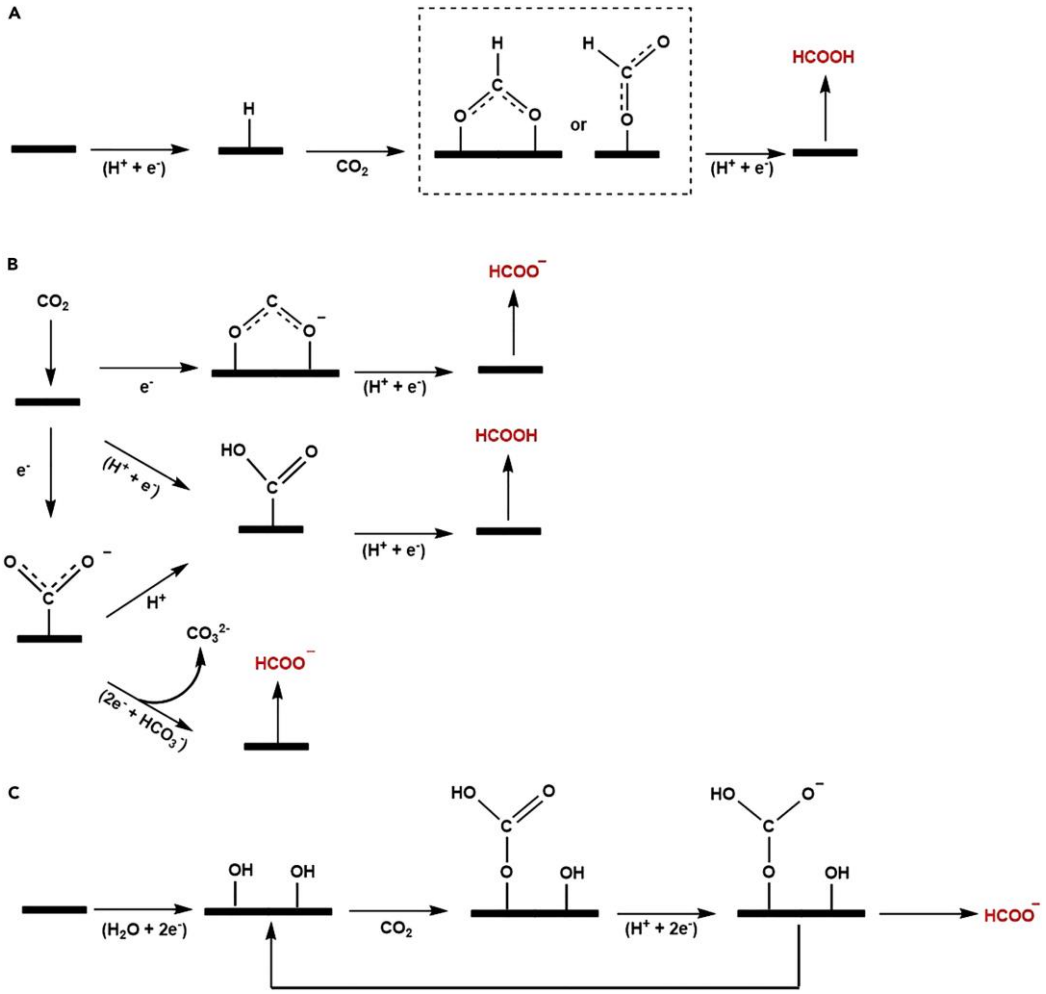

Figure 3.5 Possible reaction pathways for the eCO_2R to $HCOO^-$ or HCOOH on Sn-based electrocatalysts in aqueous media.[43]

Lastly, the formation of surface-bound Sn carbonate (Figure 3.5C) was proposed as a key chemical step in the eCO_2R towards FA on Sn-based electrodes.[152] Bocarsly *et al.* argue that prior to the eCO_2R, the presence of surface SnO_2 species enables the formation of Sn^{2+} oxyhydroxide through proton reduction. Subsequent reaction with CO_2 results in the formation of surface-bound carbonate, which is converted to $HCOO^-$ via a two-electron and one proton transfer. After desorption of the final product,

the Sn-based electrocatalyst is returned to its Sn^{2+} oxyhydroxide state.[43,152] This metastable Sn^{2+} oxyhydroxide is proposed by multiple researchers as the active site for the eCO_2R towards FA on Sn-based electrodes. Nevertheless, no universal consensus concerning the active site of Sn-based electrocatalysts has currently been reached in state-of-the-art literature. Nonetheless, as described in section 4.1.4 which provides an in-depth overview of the research concerning this topic, it is obvious that oxides play an important role in the electrocatalytic performance of Sn-based electrocatalyst. Therefore, in this dissertation, Sn oxides are synthesised and utilised as electrocatalyst for the eCO_2R towards formate in the experimental chapters 5 – 7.

Another matter of debate is the rate-limiting step of the eCO_2R reaction mechanism towards FA. Multiple elementary steps such as the adsorption of CO_2 along with an electron transfer over the electrocatalyst, the proton transfer to $CO_2^{\bullet-}$ for the formation of $^{\bullet}OCHO$, the proton-coupled electron transfer (PCET) to form $^{\bullet}OCHO$, or the desorption of the final product have been considered to be the RDS. Recently, Deng *et al.* found the formation rates of formate to be invariant with deuteration and pH of the electrolyte over Sn. Moreover, they elucidated the RDS to be the adsorption of CO_2 onto the electrocatalyst's surface, which will therefore be assumed throughout this dissertation.[153]

3.1.5 The Sabatier principle

According to French chemist and Noble laureate, Paul Sabatier, *"an ideal catalyst must bind to the reactant at an intermediate strength which is neither too weak nor too strong"*.[154]

In order to understand the Sabatier principle, we have to take a look at the underlying thermodynamic fundamentals. The Gibbs free energy difference (ΔG) between the reactant and product of an electrochemical reaction is defined by thermodynamics and independent of the electrocatalyst. Whenever the applied potential is equal to the half-cell potential, the free energies of the reactant and product become equal and the system is in equilibrium. An electrochemical reaction transpires once the electrode potential is shifted away from this equilibrium so that the resulting free energy of the product becomes lower than that of the reactant. The resulting free energy landscape between the reactant and product is tuned by the electrocatalyst.[130,151]

As previously mentioned, most reaction pathways for the eCO_2R towards formate or formic acid (Figure 3.6) have a single (or key) intermediate, whose Gibbs free energy (ΔG_{RI}) depends on the electrocatalyst surface to which it is adsorbed. An ideal electrocatalyst provides an ideal free energy landscape where the free energy of the reaction intermediate is equal to the free energy of the reactant and product at equilibrium ($\Delta G_{RI} = 0$).[130]

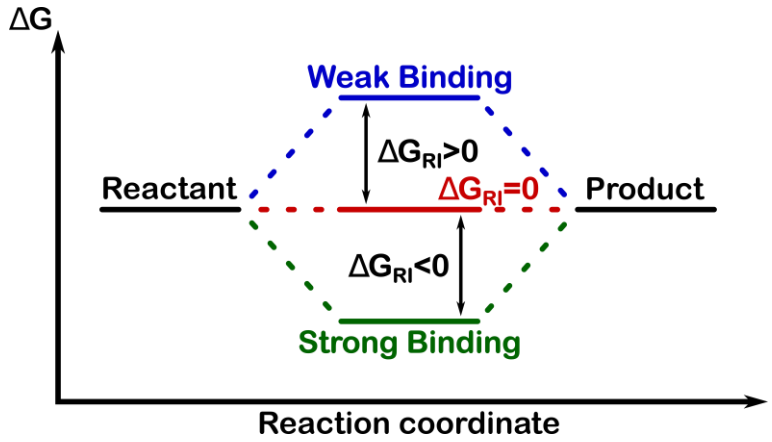

Figure 3.6 Thermodynamic free energy landscape of an electrochemical reaction with one intermediate, for different binding strengths (ΔG_{RI}) of the reaction intermediate. (Redrawn from ref. [130])

Looking at the thermodynamic free energy landscape in figure 3.6, we can explain the underlying thermodynamics of the Sabatier principle by considering the ΔG_{RI}, comparing the free energy of the reaction intermediate to that of the reactant and product. Whenever the reaction intermediate is bound too weakly to the electrocatalyst ($\Delta G_{RI} > 0$), the first step is thermodynamically unfavourable. Oppositely, when the reaction intermediate is bound too strongly ($\Delta G_{RI} < 0$), the second step is thermodynamically disfavoured. Assuming that the overall reaction efficiency is determined by the most thermodynamically unfavourable step, an ideal electrocatalyst provides an energy free landscape with no thermodynamically unfavourable elementary step.[130]

Both two-electron transfer eCO_2R products, namely CO and FA are reported to have one key intermediate, being $^{\bullet}$COOH and $^{\bullet}$OCHO, respectively.[153] This implies that the Sabatier principle should be applicable to predicting the ideal electrocatalyst for the eCO_2R towards

FA, with the ideal electrocatalyst being on top of the so-called volcano plot, which represents the measured exchange current as a function of the calculated intermediate binding energy.[34,127]

When plotting the partial current density to FA (J_{HCOOH}, mA cm^{-2}), as a descriptor for the rate of the eCO_2R reaction, versus the •OCHO binding energy, a volcano shaped plot with a maximum is obtained, according to Sabatier's principle. Figure 3.7A shows this volcano plot, using the •OCHO binding energy as a key descriptor for the eCO_2R towards FA at an applied potential of -0.9 V vs RHE.[155] Figure 3.7B depicts the reaction energy for formate formation on Sn(200), Sn(101), Bi(012), Bi(003) and Bi_ySn_{64} without applying an external potential.[71]

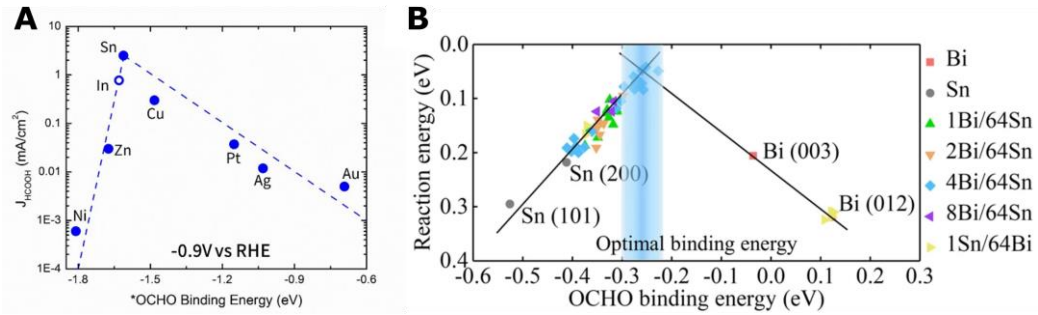

Figure 3.7 A) Volcano plot using the •OCHO binding energy as a key descriptor for the eCO_2R towards FA at -0.9 V vs RHE,[155] B) reaction energy for $HCOO^-$ formation on Sn, Bi and Bi_ySn_{64} surfaces, without externally applied potential.[71]

According to the volcano plots by Feaster *et al.* and Li *et al.*, metals such as Au, Ag, Pt and Cu provide a weak binding energy for the •OCHO intermediate, while Ni and Zn bind •OCHO too strongly. Sn and Bi are located near the top of the volcano plot, indicating that they have a close to optimal binding energy for the •OCHO key intermediate.[71,127,155]

3.2 Figures of merit

By default, electrocatalysts are compared to each other using several figures of merit, such as Faradaic efficiency (FE), energy efficiency (EE), current density (J), partial current density, cell voltage (E), overpotential (η), stability and the electrochemically active surface area (ECSA). Despite the fact that there will always be a trade-off between all of these key parameters, each and every one of these figures of merit should be considered while evaluating the overall performance of the electrochemical process.[156,157] Additionally, as expressed by Seger *et al.*, it is of utmost importance for these figures of merit to be properly measured and unambiguously reported. For example, stability measurements under mild conditions may provide a misleading overestimation of the actual electrocatalyst stability (Section 4.3; Stability evaluation). According to them, the performance of any new electrocatalyst should be evaluated and described using a matrix of figures of merit, including but not limited to, Faradaic efficiency, overpotential, current density and stability.[142] While high FE's ensure the selective production of industrially valuable products and simultaneously reduce product separation costs,[47] high current densities provide a higher productivity per electrode area and greater CO_2 conversion.[158–160] Additionally, low cell voltages or overpotentials and a high EE minimize electricity consumption and losses.[55,161] In this section, all of these figures of merit will be introduced and discussed.

3.2.1 Cell voltage and overpotential

Up until this point we have only focused on the cathodic reduction of CO_2 towards formate, whereas a complete electrochemical cell consists of a cathode and an anode, with a cathodic reduction reaction and an anodic oxidation reaction, respectively.[133] In this dissertation, the oxygen evolution reaction (OER, Eq. 3.2) is utilised as counter reaction.[162]

$$2H_2O \rightarrow O_2 + 4e^- + 4H^+ \qquad \text{(Eq. 3.2)}$$

A difference in electric potential can be measured between the cathode and anode in an electrochemical cell. This difference is called the cell voltage or cell potential (E_{cell}), measured in volts (V), and is a measure of the available energy to drive charge externally between the electrodes. The cell potential at standard conditions (E^0_{cell}, 25 °C, 1 atm) is, by convention, calculated according to equation 3.3 from the standard reduction potentials of the half-reactions.[132,133]

$$E^0_{cell} = E^0_{cathode} - E^0_{anode} = E^0_{reduction} - E^0_{oxidation} \qquad \text{(Eq. 3.3)}$$

In order to calculate the cell potential in a real electrochemical system, deviating from standard conditions, the Nernst equation (Eq. 3.4 and 3.6) is used.

$$E_{cell} = E^0_{cell} - \frac{RT}{nF}\ln\frac{a_{red}}{a_{ox}} \qquad \text{(Eq. 3.4)}$$

Where E^0_{cell} is the standard cell potential, R is the ideal gas constant (8.3145 J mol^{-1} K^{-1}), T is the temperature, n is the amount of transferred

electrons, F is the Faraday constant (9.6485 x 10^4 C mol^{-1}), and a is the activity of the reduced and oxidized species, respectively. The activity of certain species (a_i) is related to their physical concentration (C_i) through the activity coefficient (γ_i, Eq. 3.5). In practice, however, this activity coefficient is found to be close to unity at low concentrations and thus for gases, the activity is considered equal to the partial pressure, for solids, the activity is considered to be 1 and for liquids, the activity is replaced by the concentration in solution. Furthermore, the natural logarithm (ln) is often converted to $\log_{10}$ to yield Nernst equation 3.6.[132,133,163]

$$a_i = \gamma_i \cdot C_i \qquad \text{(Eq. 3.5)}$$

$$E_{cell} = E^0_{cell} - \frac{0.0592}{n} \log \frac{C_{red}}{C_{ox}} \qquad \text{(Eq. 3.6)}$$

An overview of the complete electrochemical cell for the eCO_2R towards formic acid and the standard reduction potentials for both half-reactions allows us to calculate the standard cell potential.

Cathode: $CO_2 + 2H^+ + 2e^- \rightarrow HCOOH$ E^0 = -0.25 V vs RHE

Anode: $2H_2O \rightarrow O_2 + 4e^- + 4H^+$ E^0 = 1.23 V vs RHE

Overall reaction: $2CO_2 + 2H_2O \rightarrow 2HCOOH + O_2$

$$E^0_{cell} = E^0_{reduction} - E^0_{oxidation} = -0.25\,V - 1.23\,V = -1.48\,V$$

From this standard cell potential, the change in Gibbs free energy can be calculated using equation 3.7.[132,133]

$$\Delta G^0 = -nFE^0_{cell} \qquad \text{(Eq. 3.7)}$$

$$\Delta G^0 = -nFE^0_{cell} = -4 \cdot -1.48 \cdot F = 5.92F = 571\ kJ\ mol^{-1}$$

Since the change in Gibbs free energy is positive, the reaction doesn't proceed spontaneously, but rather needs an external input of electricity, i.e. current or potential, which in turn is converted into chemical energy.[132,133]

As previously mentioned, the free energies of the reactant and product become equal and in equilibrium whenever the applied potential is equal to the standard equilibrium potential. An electrochemical reaction only occurs at a certain rate whenever an additional potential is applied. This additional potential is called the overpotential (η), which is defined as the difference between the applied potential (E) and the equilibrium potential (E_{eq}), obtained from the Nernst equation, of the intended eCO_2R half-reaction (Eq. 3.8).[127,130,132,133,163]

$$\eta = E - E_{eq} \qquad \text{(Eq. 3.8)}$$

Generally, one tries to keep this overpotential as low as possible, to obtain a high energy efficiency (Section 3.2.2) and to diminish *in situ* SnO_2 reduction (Section 4.1.4), among other things.

3.2.2 Faraday's laws of electrolysis

The conversion of electrical energy into chemical energy, in order to oxidise or reduce species, is called electrolysis.[132] Faraday's laws of electrolysis state that (I) the amount of chemical change, induced by a current at an electrode-electrolyte interface, is proportional to the quantity of electricity

used and (II) that the amount of chemical changes produced by the same quantity of electricity in different substances are proportional to their equivalent weights. The quantity of electricity that will cause a chemical change of one equivalent weight unit has been designated as the constant of Faraday (F), which is equal to 9.6485309 x 10^4 C mol^{-1}. Faraday's law can be written as equation 3.9, with Q being the charge (in coulombs), n the amount of product formed (in moles), z the amount of transferred electrons in the half-reaction, and F the constant of Faraday.[163]

$$Q = nzF \qquad \text{(Eq. 3.9)}$$

Since CO_2 can be converted into a wide variety of products, multiple reactions can take place simultaneously, dividing the input electrical energy across multiple reaction products. A considerable amount of the input charge can be consumed by the competing HER.

$$2H_2O + 2e^- \rightarrow 2H_2 + 2OH^- \qquad \text{(Eq. 3.10)}$$

The Faradaic efficiency (FE) is a measure for the selectivity towards the desired product and is expressed in equation 3.11, as the percentage of electrons (charge) consumed for the formation of the desired product. Where n is the amount of moles formed of the desired product (FA), z is the number of transferred electrons (e.g. n = 2 for the eCO_2R towards FA), and Q is the total charge passed during the electrolysis.[127,164]

$$FE = \frac{electrons\ (charge)\ used\ for\ the\ desired\ product}{Total\ charge\ passed}$$

$$FE = \frac{nzF}{Q} \qquad \text{(Eq. 3.11)}$$

Additionally, the energy efficiency (EE), calculated from the equilibrium potential, overpotential and FE, describes the overall energy utilization towards the desired product.[164]

$$EE = \frac{E_{eq}}{E_{eq} + \eta} \cdot FE \qquad \text{(Eq. 3.12)}$$

From equation 3.12, it is clear that in order to obtain a high EE, a low overpotential and high FE must be achieved. From an industrial point of view, a high FE ensures less downstream processing, while a low overpotential and high EE minimise the required energy input.

3.2.3 Electrochemically active surface area and current density

The electrolysis of CO_2 is typically carried out either chronopotentiometrically or chronoamperometrically, by applying a constant current or potential, respectively, and measuring the other as a function of time. Both current (I) and voltage (V, potential) are related to one another via Ohm's law.

$$V = I \cdot R \qquad \text{(Eq. 3.13)}$$

The overall current density (J) for the eCO_2R is typically calculated by dividing the current by the geometric surface area of the working electrode. Furthermore, the partial current density for a specific product (J_i) is acquired by multiplying the current density by the FE for this desired product.[132,133,164]

Currently, electrocatalytic activity is generally described using four metrics: geometric activity, which is the current density normalized to the geometric surface area of the electrode (mA cm_{geo}^{-2}); mass activity, which is the current per mass of electrocatalyst (mA $mg_{catalyst}^{-1}$); turnover frequency (TOF), which is the amount of electrons produced/consumed per active site per second; and specific activity, which is the current normalized to the real electrochemically active surface area of the electrocatalyst (mA $cm_{catalyst}^{-2}$).[165]

Since electrocatalysis is in essence a surface phenomenon, an adequate determination of the ECSA is of utmost importance to assess electrocatalyst activity. The ECSA of an electrocatalyst is usually measured by underpotential deposition (UPD), CO stripping or the non-faradaic double layer capacitance (C_{dl}).[165] In this dissertation, the ECSA is derived from the electrochemical double layer capacitance (C_{dl}) of the catalytic surface.

Chapter 4

Sn-based electrocatalyst stability: a crucial piece to the puzzle

In the following chapter, a wide variety of Sn-based electrocatalysts with various morphologies will be discussed. Insights concerning their most predominant degradation mechanisms and the importance of a rational electrocatalyst design and mitigation strategies to obtain prolonged electrocatalyst stability are highlighted.

This chapter has been published as K. Van Daele *et al.*, "Sn-Based Electrocatalyst Stability: A Crucial Piece to the Puzzle for the Electrochemical CO_2 Reduction toward Formic Acid," *ACS Energy Lett.*, vol. 6, no. 12, pp. 4317–4327, Dec. 2021.
(https://doi.org/10.1021/acsenergylett.1c02049)
And it has been updated with the latest state-of-the-art research.

4.1 A deep dive into the stability of Sn-based electrocatalysts

Throughout the past decades, Sn-based electrocatalysts have developed from bulk foils into rationally designed, highly selective Sn-based electrocatalysts.[66] Even though Sn-based electrocatalysts have become more advanced in terms of morphology and composition, we will demonstrate in this chapter that they have also become more prone to degradation since considerably more degradation mechanisms come into play during the eCO_2R on these rationally designed electrocatalysts as compared to bulk Sn electrodes. Therefore, obtaining a prolonged electrocatalyst stability has become even more important in order to retain their enhanced selectivity and activity, attributed to these rationally designed electrocatalysts, throughout long-term operation.

4.1.1 Bulk Sn-based electrocatalysts

Studies, developed by Chiacchiarelli *et al.,* on a bulk Sn electrode in a 0.5 M $KHCO_3$ electrolyte rotating disk electrode (RDE) assembly identified the main routes by which electrocatalytic performance is hindered.[166] Through their analysis three main routes are highlighted as primary causes for deactivation: (I) cathodic degradation of the ECSA, (II) deposition of non-catalytic species (e.g. reaction intermediates or metallic species from the electrolyte) on the surface of the electrode (poisoning), and (III) anodic degradation of the catalyst through the formation of gas bubbles which prevent the cathodic polarization. Several SEM images were taken prior and post reaction to analyse variations in surface morphology and

composition in an attempt to elucidate degradation mechanisms occurring on the electrocatalyst. Accordingly, grain size and orientation were found to strongly influence the tendency to present weight loss or weight gain, due to formation of SnH_4 (g), or due to deposition of contaminants, respectively. They noted that the tendency of Sn electrodes to corrode was linked to [001] and [110] orientations, as these seemed to present faster rates of reaction and rougher surfaces.[166]

4.1.2 Nanostructured monometallic Sn-based electrocatalysts

Zhao *et al.* highlighted how monometallic Sn-based electrocatalysts display varying FE's towards FA production based on catalyst layer thickness, ratio of edge, corner and planar sites and improved electrochemically active surface area. According to their research, a high ECSA enables reactivity at lower overpotentials, avoiding HER.[66] Hence, studies such as the one developed by Ma *et al.* focusing on the synthesis of Sn nanostructures with a high surface area (90.1 $m^2\ g^{-1}$), large porosity (0.74 $cm^3\ g^{-1}$) and enriched with grain boundaries are of increasing interest.[167] Furthermore, Zhang *et al.* demonstrated a particle size dependency for the FE_{FA} on reduced nano-SnO_2/graphene electrodes. They reported a maximised FE_{FA} of 93.6% on 5 nm SnO_2 nanocrystals and concluded that this optimum is most likely due to an optimised binding energy of the $CO_2^{\bullet-}$ reaction intermediate and the suppression of the competing HER.[100]

Aside from providing an enhanced ECSA and thus more active sites, nanostructured electrocatalysts exhibit lower onset potentials for the

eCO_2R towards FA and consequently yield a higher selectivity.[168] Additionally, nanostructured materials exhibit an increased stability because of their greater tolerance towards poisoning from heavy metal impurities in the electrolyte as compared to their bulk counterparts. Thanks to their increased ECSA, nanostructured electrocatalysts are able to withstand higher concentrations of impurities or contaminations.[169] However, in order to maintain these enhancements in both selectivity and activity, nanoparticle specific degradation mechanisms, such as agglomeration, particle detachment, Ostwald ripening, reshaping, pulverisation and dissolution must be inhibited.

He *et al.* reported the agglomeration of uniformly-dispersed SnO_2 nanoparticles supported on a three-dimensional porous carbon sheet. After 10 h of electrolysis at a current density of 29 mA cm^{-2}, the FE_{FA} decreased from 92% to 80%.[120] In another work, Wu *et al.* observed a significant decrease from 90% to 50% in the FE_{FA} of Sn nanoparticles during a 60 h electrolysis.[73] Transmission electron microscopy (TEM) images (Figure 4.1) revealed the pulverisation of these Sn nanoparticles, leading to both morphological and particle size changes. The original 100 nm carbon supported spherical Sn particles were found to rapidly transform into smaller irregular particles after merely 3 h of electrolysis, which further decreased (albeit at a decreasing pulverisation rate) over the course of the experiment to around ≈3 nm after 30 h of electrolysis. Furthermore, a pulverisation-induced increase in Ohmic resistance was observed, leading to a decrease of the cathodic potential and a consequently decreasing

Faradaic efficiency. The process of pulverisation appeared to continue until a critical particle size was reached. For Sn particles this critical size was calculated to be approximately 3 nm, which was experimentally confirmed by SnO_2 nanoparticles (≈3 nm) supported on a gas diffusion electrode that exhibit an excellent stability of 174 h, maintaining a FE_{FA} of 70% and a low current density of ≈12 mA cm^{-2}.[73]

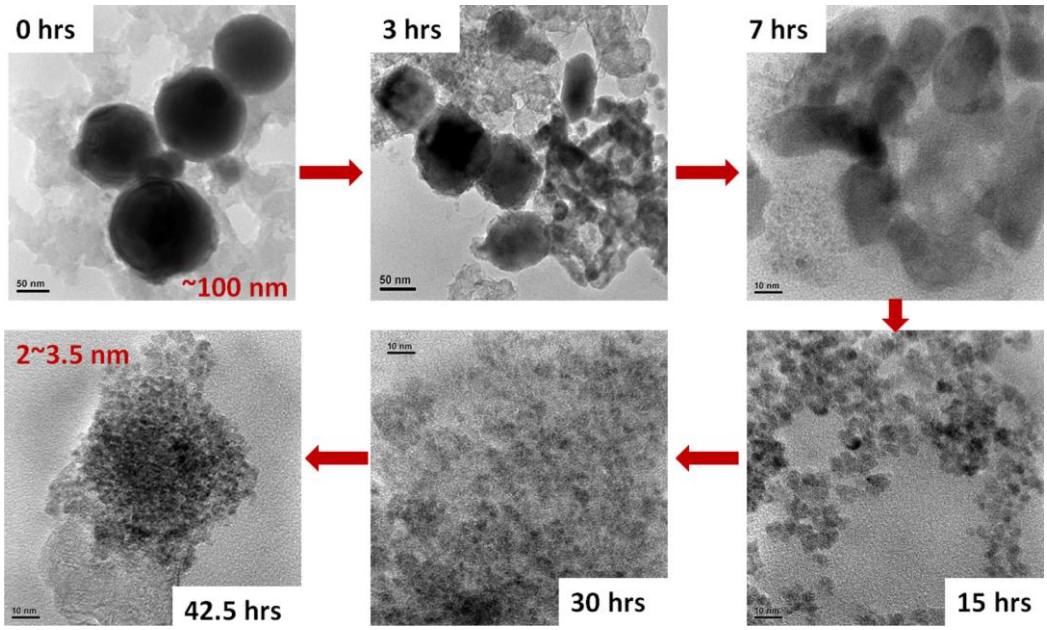

Figure 4.1 TEM images of the morphology and size evolution of 100 nm Sn particles during a long-term operation.[73]

Wu *et al.* attributed this pulverisation to hydrogen diffusion-induced stress. The hydrogen ad-atom, which is initially formed by proton reduction and adsorption during CO_2 electrolysis, is reported to diffuse into the bulk of the Sn electrode creating stress and subsequent pulverisation of the Sn particles.[73] However, Kim *et al.* proposed that the hydrogen diffusion-induced pulverisation insufficiently accounts for the

pulverisation of SnO_2 electrocatalysts. Their experimental results clearly show that Sn is leached from SnO_2 nanoparticle electrocatalysts due to the electrochemical reduction of SnO_2 to Sn. The leaching of Sn creates defects and fractures on the SnO_2 particle surface, which in turn promotes pulverisation and degradation.[75]

4.1.3 Multimetallic Sn-based electrocatalysts

When considering multimetallic electrocatalysts, it is well known that combining different metals allows tailoring of the surface composition and thus control over the relative binding strength of relative intermediaries, which can help control selectivity towards CO or formic acid.[66] In literature, several Sn-based bi- and tri-metallic electrocatalysts have been reported.[45,70,75,85,88,96,104,108,117,155-160]

According to the Sabatier principle, maximum activity is achieved when key intermediates neither bind too strong nor too weak to the active electrocatalytic site. As previously mentioned, Feaster *et al.* report that $^{\bullet}OCHO$ is most likely the key descriptor for the reduction of CO_2 to $HCOO^-$ as a clear correlation is observed between $^{\bullet}OCHO$ binding energies and $HCOO^-$ activity. Moreover, metallic polycrystalline Sn was found to have a near-optimal binding energy of the $^{\bullet}OCHO$ key intermediate by appearing at the top of the volcano plot, making it highly challenging to further improve its binding energy by combining tin with other metals.[155] Nevertheless, Ju *et al.* have shown that the ratio of Sn/Cu on the electrocatalyst surface determines if eCO_2R intermediates will bind to the

surface via the carbon atom (•COOH) or via the oxygen atom (•OCHO), resulting in the production of CO or $HCOO^-$, respectively.[176] According to a Bader analysis by Zheng *et al.*, alloying Sn with Cu results in a charge transfer from Sn to Cu. As the structure of the $CuSn_3$ alloy is different from both Cu and Sn, the origin of this improved selectivity towards formic acid originates from a combination of geometric and electronic effects. The most important effect being that the binding of COOH•, H• and OCHO• are all weakened on these CuSn alloys and thus selectivity towards formic acid is enhanced.[82] Following DFT simulations on Bi-Sn(101) and Sn(101) surfaces, Wen *et al.* concluded that the electron states of Sn (both p and d orbitals) are upshifted away from the Fermi level, because of orbital interaction in Bi-Sn bimetallic electrocatalysts. This results in a favourable adsorption of the •OCHO intermediate on Bi-Sn surfaces compared to a Sn surface and thus an enhanced conversion of CO_2 to formic acid.[77] By introducing a second or third metal, synergistic metal-metal interactions enhance the eCO_2R performance towards formic acid.[82,174] Thus, developing structures that can prevent dissolution of a metal from the surface of the catalyst or alterations to the surface composition by diffusion of metal atoms from the surface to the bulk or the reverse is of crucial importance for maintaining FE stability throughout time.

4.1.4 Sn oxides in a quest to find the electrocatalytic active site

Other attempts at finding the most selective and active Sn-based electrocatalyst for the eCO_2R towards formic acid targeted Sn oxides, as more and more evidence emphasises the importance of an oxide layer.

At present, multiple Sn species, ranging from Sn^{4+}, Sn^{2+}, Sn^{0}, and metastable Sn^{2+} oxyhydroxide have been proposed as the electrocatalytic active site for the eCO_2R towards FA on Sn-based electrodes. Unfortunately, as previously mentioned, no universal consensus concerning the active site of Sn-based electrocatalysts has currently been reached in state-of-the-art literature.[139,152,177–180]

Based on DFT calculations, Cui *et al.* found that CO_2 binds weakly on a Sn(112) surface, which is generally found to be the most active for C-O bond breaking, making it highly improbable for the eCO_2R on metallic Sn to start from an adsorbed CO_2 species. Instead, they argue that CO_2 will react with an H ad-atom, which is formed by proton reduction and adsorption.[178] In a later study, however, Cui *et al.* highlighted the importance of an oxide layer and demonstrated that CO_2 adsorption is feasible on a SnO/Sn(112) surface by formation of a carbonate species, as depicted in figure 4.2. They argued that, the presence of a SnO_x monolayer gives rise to the formation of hydroxyls, through a two-electron proton reduction from the native SnO_x species to yield a metastable Sn^{2+} oxyhydroxide species, which enables the surface to react with CO_2 to form surface-bound $HCO_3^{\bullet-}$ species. Following the transfer of 2 electrons and a proton, these surface bound Sn carbonate species are electrochemically reduced to yield formate, which quickly desorbs, returning the surface to Sn^{2+} oxyhydroxide.[152,179] Damas *et al.* support this reaction mechanism, and state that Sn oxides indeed play an important role in CO_2 activation.[139] Likewise, DFT studies by Li and Deng *et al.* validated the

crucial role of H_2O dissociation to form a hydroxylated Sn layer into which the CO_2 molecules can be inserted.[181,182]

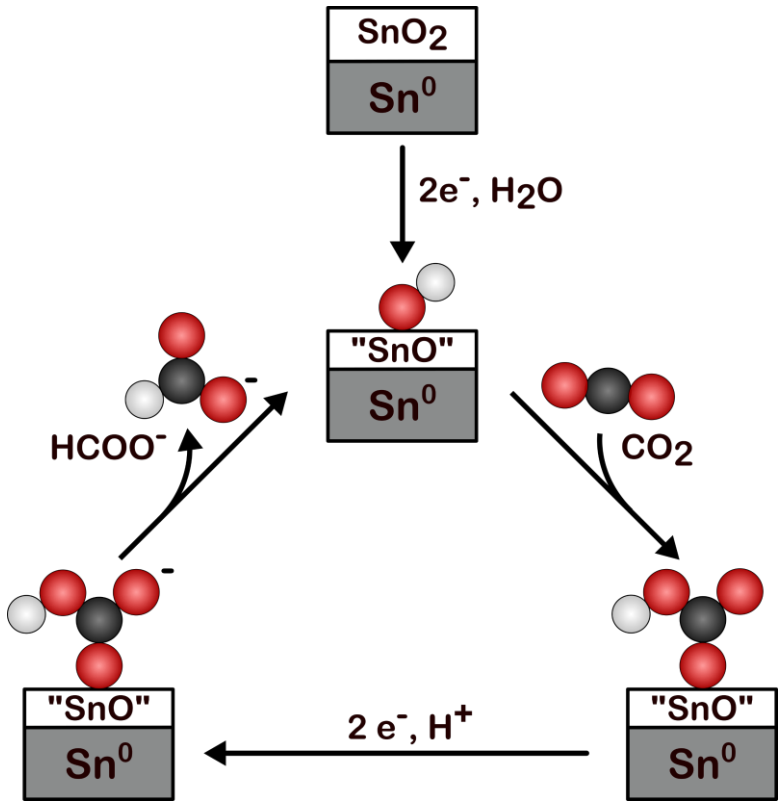

Figure 4.2 Schematic diagram of the proposed mechanism for the electrocatalytic CO_2 reduction to formic acid on a Sn/SnO_x electrocatalyst, redrawn from ref.[152]

The influence these surface oxides species have on the electrocatalytic performance of Sn-based catalysts was further investigated via DFT calculations by An *et al.*[122] In their work, they reported an excellent electrocatalytic performance for both metallic Sn and Sn oxide surfaces for the eCO_2R towards formic acid and found that Sn oxides/metal Sn interfaces aid in suppressing the competing HER. Furthermore, a suitable ratio of $Sn^0/Sn^{2+}/Sn^{4+}$ on the electrode surface could result in a synergistic effect, since the presence of tetravalent tin (Sn^{4+}) was found to reduce the

overpotential, while the presence of divalent tin (Sn^{2+}) improves formic acid selectivity.[122] Similarly, Ning *et al.* demonstrated through DFT calculations that formate production is energetically favoured on *in situ* formed SnO_2/Sn Mott-Schottky heterojunctions, compared to pristine SnO_2 and Sn.[180]

Utilising *ab initio* density functional theory (DFT) calculations, Salvini *et al.* reported that SnO_2(110) surfaces are not inherently electrocatalytically active for the eCO_2R towards FA or competing HER. However, as soon as a metallic bilayer is formed at the SnO_2 surface, by *in situ* reduction, the electrocatalyst becomes selective for the eCO_2R towards FA. Acknowledging that under eCO_2R operating conditions, both oxidized and zerovalent Sn species are detected by in operando measurements, Salvini *et al.* argued that the observed signals of these oxidized species originate from the subsurface layers, while a thin Sn^0 surface layer selectively catalyses the eCO_2R towards FA. Furthermore, there calculation revealed that for a thick layer of reduced Sn^0, the eCO_2R towards FA and the HER become thermodynamically competitive and the electrocatalytic selectivity of the Sn-based catalyst is decreased.[177] This implies that there is a critical balance between the need for some metallic Sn to be present and too much Sn^0 being present, resulting in excessive HER.

Even though there is no general consensus on the electrocatalytic active Sn site, it is clear that oxides play an important role. As a result, *in situ* reduction to metallic Sn should be taken into account as an additional

degradation mechanism. Dutta *et al.* have used in operando Raman spectroscopy and X-ray absorption spectroscopy (XAS) to observe changes in the oxidation state of SnO_2 under eCO_2R operating conditions. At cathodic potentials, Sn^{4+} in SnO_2 nanoparticles on a rGO support can be reduced to Sn^{2+}, which is presumed to be selective towards formic acid production, or metallic Sn where the competing hydrogen evolution reaction is favoured. Furthermore, the experimental stability range of SnO_2 appears to surpass the thermodynamic stability region of the Pourbaix diagram (Figure 4.3), as both Raman spectroscopy and selectivity indicated the presence of a metastable SnO_2 phase in a wide potential range, yielding the highest FE towards formic acid.[183,184]

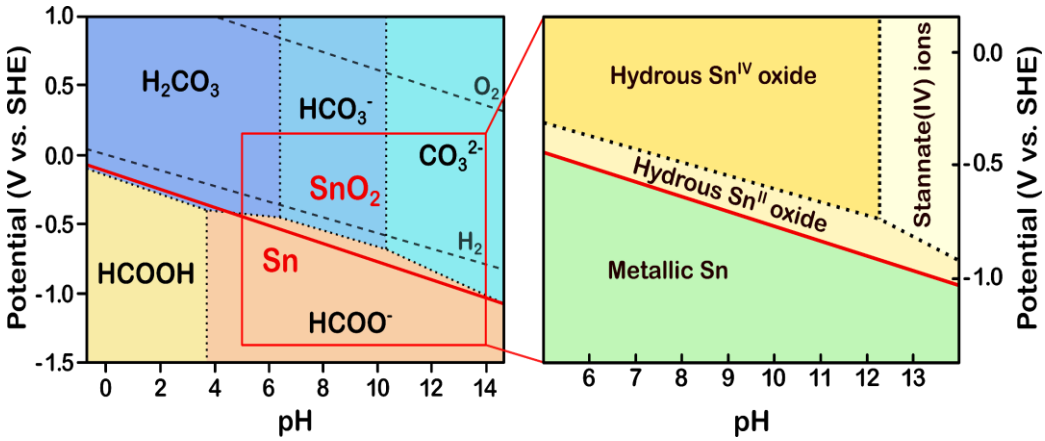

Figure 4.3 Combined Pourbaix diagram of Sn-water, considering various Sn oxidation states and the carbonate-water system with the dominant carbonate species, redrawn from ref.[184,185]

Baruch *et al.* have used *in situ* attenuated total reflectance infrared spectroscopy (ATR-IR) to proof the presence of a metastable oxide layer with hydroxylated structures at the interface on Sn-based cathodes at

reducing potentials. Experiments conducted on bulk $Sn_6O_4(OH)_4$ and SnO_2 nanoparticles exhibited similar results, suggesting that Sn^{2+} oxyhydroxide is indeed the catalytic active species.[152] The importance of an oxide layer was also studied by Zhang *et al.*,[186] and Chen and Kanan.[187] Both studies reported a decrease in FE_{FA} after removal of the native oxide layer via etching, underlining the importance of Sn oxides for the selective eCO_2R towards formic acid.[186,187]

In situ SnO_2 reduction often goes hand in hand with morphological changes, both leading to electrocatalyst degradation. Carbon black supported SnO_2 nanoparticles (≈100 nm), reported by Xiang *et al.*, have a FE of 80% for formic acid. However, after 6 h of electrolysis the particle size and shape significantly changed to particles of 200-500 nm, while *ex situ* XRD measurements confirmed the conversion from polycrystalline SnO_2 to polycrystalline Sn due to electrochemical reduction.[188]

Furthermore, *in situ* SnO_x reduction at high cathodic potentials appears to only be harmful when the oxide is fully reduced to metallic Sn. Several partially reduced Sn oxide electrocatalysts have been shown in literature to still be active for the eCO_2R towards formic acid. For example, Han *et al.* described that although a fragment of their SnO_2 nanoparticles, incorporated into a 2D titania nanosheet lamella assembly (TNS-2.0-SnO_2), is electrochemically reduced to Sn^0, the resulting Sn/SnO_x electrocatalyst still performed adequately in the eCO_2R towards formic acid. A FE_{FA} of 73% and a current density of approximately 10 mA cm^{-2}

at -1.6 V vs. RHE were successfully maintained for 16 hours.[104] Furthermore, Luc *et al.* determined the optimal thickness of a partially oxidized SnO_x shell for a bimetallic $Ag_{78}Sn_{24}$ core-shell electrocatalyst to be ≈1.7 nm. A high selectivity of 80% towards formic acid with a partial current density of 16 mA cm^{-2} at -0.8 V vs. RHE and stability of 24 h were reported, after which only a slight SnO_x reduction to metallic Sn was observed using *ex situ* XPS.[92]

In addition, Ye *et al.* recently reported a hierarchical $Sn_{2.7}Cu/SnO_x$ core/shell electrocatalyst with a high current density of 243.1 mA cm^{-2} at -0.55 V vs. RHE, while maintaining a stable FE of approximately 90% towards formic acid for 40 h.[88] *In situ* extended X-ray absorption fine structure (EXAFS) measurements reveal partial reduction of the SnO_x shell at -0.93 V vs. RHE, which is confirmed by *ex situ* XPS analysis. A full *ex situ* characterisation by high-resolution transmission electron microscopy (HRTEM) visibly confirmed shrinkage of the amorphous SnO_x shell from 3.2 nm to 2.7 nm. Remarkably, the SnO_x shell can be reconstructed *in situ*, during CO_2 electrolysis, due to migration of redundant core Sn atoms outwards into the amorphous SnO_x shell. This was confirmed because crystalline SnO_2 species, originating from the spontaneous *ex situ* oxidation of this crystalline Sn, were found embedded in the amorphous SnO_x shell.[88]

Finally, the morphology of mesoporous SnO_2 structures is largely preserved during CO_2 electrolysis-induced SnO_x reduction. A nanoporous Sn/SnO_2

(np-Sn/SnO_2) composite electrocatalyst with a high selectivity (>70%) for formic acid over a wide potential range (-0.8 to -1.4 V vs. RHE) was reported to be stable over 58 hours at -0.8 V vs. RHE by Liu *et al.* However, despite insignificant morphological changes to its mesoporous structure, XPS analysis revealed an increase in the portion of Sn^0 from 21.8% to 30%, after eCO_2R, due to the reduction of Sn^{4+} to Sn^0.[80] Similar results were obtained with hierarchical mesoporous SnO_2 nanosheets on carbon cloth (SnO_2/CC). Li *et al.* noticed a well preserved mesoporous structure without any morphological changes after 24 hours of electrolysis with a current density of 50 mA cm^{-2} at -1.6 V vs. Ag/AgCl and a selectivity of 87% for formic acid. Nevertheless, after electrolysis, the XRD pattern revealed new peaks which could be attributed to metallic Sn, suggesting *in situ* SnO_2 reduction.[91]

Based upon the preceding discussion, it is evident that surface oxides play a crucial role in the electrocatalytic performance of Sn-based electrocatalysts and their selectivity towards FA. In this dissertation, the electrocatalytic active site of Sn-based electrocatalysts is therefore assumed to be the frequently reported metastable Sn^{2+} oxyhydroxide, which is obtained after the initial *in situ* reduction of SnO_2. To this extent, all synthesised electrocatalysts (Chapters 5 – 7) in this dissertation comprise fully oxidised SnO_2 in order to study and enhance their electrocatalytic performance and stability.

4.2 Rational electrocatalyst design

Despite the fact that Sn-based electrocatalysts will always be susceptible to degradation at high cathodic potentials during the eCO_2R, rational electrocatalyst design has been shown to elongate electrocatalyst lifetime. An overview of the most predominant degradation pathways, reported in literature and discussed in section 4.1, is given in figure 4.4.

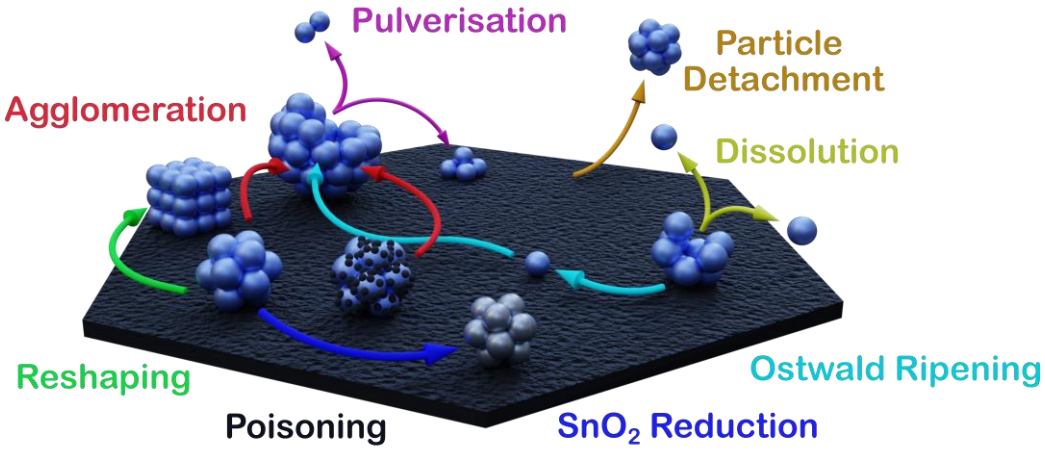

Figure 4.4 Overview of the most predominant degradation pathways for Sn-based electrocatalysts.[189]

Unfortunately, nearly all degradation pathways depicted in figure 4.4 are considered irreversible as they bring about permanent morphological changes. The only exceptions being (partial) electrocatalyst recovery after poisoning or in situ SnO_2 reduction.

Catalyst poisoning by reaction intermediates or impurities originating from the electrolyte, electrolyser components or CO_2 feed, is partially recoverable by renewing the electrolyte solution or briefly reversing the polarity of the electrolyser.[190–194] In their research, Luc *et al.* revealed the

reversible nature of Sn catalyst poisoning caused by sulphur dioxide (SO_2) impurities. In the presence of 1% SO_2, the FE_{FA} dropped because of the thermodynamically more favourable SO_2 reduction. However, contrary to Cu catalysts, these SO_2 impurities caused no permanent selectivity alterations on Sn and Ag catalysts.[194]

The reversibility of *in situ* SnO_2 reduction to metallic Sn under harsh cathodic operating conditions has been studied on reduced graphene-oxide supported Sn^{4+} oxide nanoparticles (SnO_2NPs@rGO) (Figure 4.5a), by Dutta *et al.*[184]

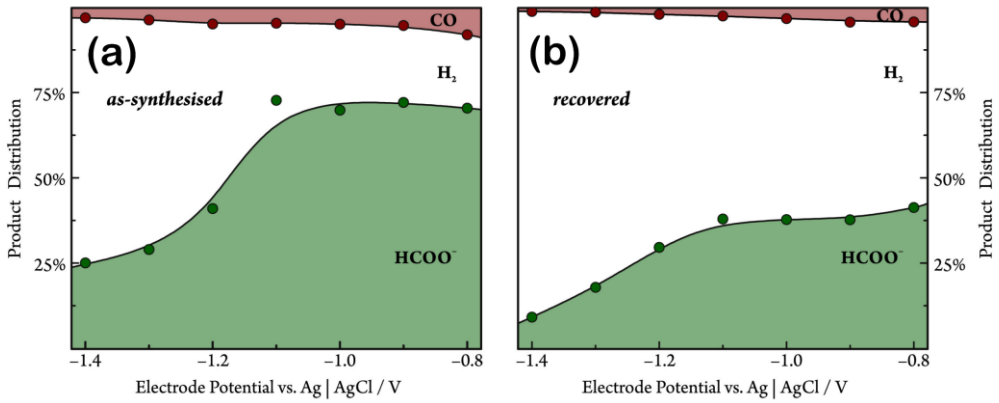

Figure 4.5 Product distribution as-synthesised (a) and recovered (b) SnO_2NPs@rGO electrocatalyst.[184]

They found that SnO_2 nanoparticles, which had previously undergone complete reduction to Sn^0, could only be partially recovered as Sn^{4+} and that their high initial selectivity was almost completely and irreversibly lost, as shown in figure 4.5b.[184]

In order to prolong electrocatalyst lifetimes, rational electrocatalyst design, to prevent or reduce catalyst degradation, will thus be of great importance.

In literature, several mitigation strategies are being used and suggested, which are discussed in more detail below.[195]

At present, the most established mitigation approach to reduce morphological degradation mechanisms such as agglomeration, particle detachment, dissolution, leaching and Ostwald ripening, is the particle confinement strategy.[196,197] This has also been proven in literature to some extent for Sn-based electrocatalysts.

For example, Lei *et al.* reported an increased stability over 50 hours for Sn quantum sheets confined in graphene, relative to 15 nm Sn nanoparticles mixed with graphene, 15 nm Sn nanoparticles and bulk Sn which all exhibited poor stability during this period. The confined Sn quantum sheets showed a very stable current density of 21 mA cm^{-2} at -1.8 V vs. SCE, while the FE_{FA} remained larger than 85%.[84] To further enhance electrocatalyst stability, Kim *et al.* synthesized a leaching-resistant SnO_2/γ-Al_2O_3 nanocatalyst. Remarkably, they achieved stability over 152 hours while maintaining a Faradaic efficiency of 65% towards FA and a current density of 21.7 mA cm^{-2}. The leaching-resistant SnO_2/γ-Al_2O_3 nanocatalyst was found to retain its morphology, crystallinity, size and electrochemical performance after electrolysis due to the strong interaction between the electrocatalyst and its supporting material.[75]

As evidenced previously, *in situ* reduction of Sn oxides to metallic Sn is another crucial degradation pathway which should be mitigated in order for Sn-based electrocatalysts to become industrially feasible. Aside from

lowering the operating potential and thus overpotential, a possible strategy to overcome this stability issue could be the co-electrolysis of CO_2 with low concentrations of oxygen (O_2) or other oxidants. He *et al.* revealed in their study on copper catalysts that this co-electrolysis results in an increased surface coverage of adsorbed hydroxyl species.[198] When looking at Sn-based electrocatalysts, this could be considered beneficial and possibly prevent *in situ* SnO_2 reduction to metallic Sn. Nonetheless, further research should be devoted to this topic to confirm this hypothesis.

Other mitigation strategies mentioned in literature include: (I) a modification of the electronic structure, which could prevent reaction intermediate poisoning by directly adjusting the binding energy of reaction intermediates[195] or result in lower overpotentials, which in turn attenuates other degradation pathways such as *in situ* SnO_2 reduction or pulverisation. Lowering overpotentials (by means of dopants or other methods), furthermore, limits the required amount of electricity and increases the energy efficiency of the overall process. (II) Single atom fixation, which has been proven to increase electrocatalyst stability by fixing metal atoms within the support material.[195] Several multidentate nitrogen ligand-stabilized single-atom electrocatalysts have been reported in literature for the eCO_2R towards CO.[199] Aside from providing a beneficial intermediate stabilisation and an easy charge transfer, single-atom electrocatalysts appear to be more resistant to poisoning since metallic impurities could be more easily deposited on the carbon support material rather than on the active electrocatalyst site.[195,199]

4.3 Stability evaluation

Given the importance of Sn-based electrocatalyst stability, as demonstrated above, this also entails the need for a robust, unambiguous and standardised stability evaluation, which has also been articulated in recent literature.[200–203] However, despite the proposal of several methods and techniques to assess the stability and degradation mechanisms of electrocatalysts, a unified approach has not been implemented to this date. In our own research (Chapters 5 - 7), long-term (24 h) measurements are performed to obtain an initial assessment of the electrocatalyst stability.[204–207] In the following paragraphs an overview off several well-known electrochemical evaluation methods and accelerated degradation tests, that have been used for years to determine and predict the lifetime of electrocatalysts in fuel cell, water electrolyser and chlor-alkali electrolysis research, are summarised.

Nowadays, prolonged chronoamperometric (CA) or chronopotentiometric (CP) measurements,[208] combined with *ex situ* characterisation techniques such as XRD, XPS and electron microscopy,[209] are becoming common practice to investigate the electrocatalytic stability. However, as suggested by Birdja *et al.*, electrocatalyst stability should preferably be reported by means of partial current density (whether or not normalized by the ECSA), for the targeted product, and not as FE_{FA}, current (density) or cell potential as a function of time. The usage of partial current density as a key descriptor for electrocatalyst stability embodies the important trade-off between activity (current density) and selectivity (FE), and

furthermore, provides valuable insights into the production rate of a specific product, which is more relevant.[201] Electrocatalyst activity, selectivity and stability are all highly dependent on the local reaction environment (local pH conditions, mass transfer, etc.)[210] and experimental parameters (duration, sampling frequency, etc.).[201] For future eCO_2R research it will thus become increasingly more important to test state-of-the-art electrocatalysts under more realistic and industrially relevant operating conditions, utilising a unified stability evaluation protocol.[210]

Given that long-term CA or CP measurements are extremely time consuming (several days to weeks or months), accelerated degradation/durability tests (ADT) could provide a time efficient indication of electrocatalyst lifetime. During an ADT, system durability (or part of the system) is evaluated by applying extreme conditions such as high current densities, elevated temperature or pressure, high electrolyte concentration, the introduction of CO_2 stream contaminants (N_2, NO_x, SO_x, H_2S, hydrocarbons etc.) or potential/current cycling. ADTs have already been proven to be essential for the development of, for example, proton exchange membrane fuel cells (PEMFC), as they enable a stability assessment of several components (such as the electrocatalyst, GDE, electrocatalyst binder and membrane) within a short period of time.[203] Exploring ADT protocols used for other electrochemical processes such as water electrolysis, chlor-alkali electrolysis and fuel cells, Nwabara *et al.* were able to validate several ADT protocols for CO_2 electrolysis.[203] In their research, two methods; (I) total charge passed and (II) electrolyte molarity

were tested. When passing the same total charge in a shorter timescale (by increasing the applied current density and thus decreasing electrolysis time), an exponential degradation rate was observed with respect to the applied current density. Moreover, an increase in electrolyte molarity revealed a limiting conductivity after which cathode degradation accelerated.[203] Other ADT protocols such as elevated temperature or pressure, the introduction of CO_2 feed contaminants or stress testing via potential/current cycling could also provide valuable information concerning the electrocatalytic stability, but only become important once a base stability of 48 h at >200 mA cm^{-2} and a FE_{FA} of >80% has been achieved.[203]

In addition, every type of electrocatalyst lifetime evaluation should be accompanied by *ex situ* or *in situ* characterisation techniques, irrespective of the evaluation protocol. In order to unravel all Sn-based electrocatalyst degradation mechanisms, the development and implementation of several complementary techniques, such as *in situ* liquid-phase transmission electron microscopy (LP-TEM),[211] operando electrochemical X-ray Absorption Spectroscopy (XAS) and *in situ* Raman spectroscopy is paramount.[212]

Combining several of the previously mentioned testing protocols, Popović *et al.*[202] recently proposed a unified stability evaluation. Although their guidelines were mainly suggested for copper electrocatalysts, their proposed standardized tests can be extended to other electrocatalysts for

the eCO_2R. First, a 12-24 h electrolysis experiment with hourly on-line gas product distribution measurements should be performed. Subsequently, start-stop conditions should be simulated by performing a 1 h electrolysis, followed by 200-1000 potential cycles from OCV to the operating potential at a scan rate between 50-100 mV s^{-1} and a final 1 h electrolysis, in order to compare the selectivity before and after potential cycling. Both experiments should be accompanied by *ex-* or *in situ* morphological characterisations.[202] This proposal can be extended to Sn-based electrocatalysts by including liquid product analysis for FA by means of HPLC or NMR. Finally, one could vary the method of potential cycling from triangular wave cycling to square wave cycling to increase the applied stress on the electrocatalyst.

An alternative approach to perform electrocatalyst stability measurements, is to simulate electrolyser operating conditions. Recently published gastight rotating disk electrode (RDE) setups[213,214] can allow for the evaluation of product selectivity and (partial) current density over prolonged measurements, while accurately controlling mass transfer to and from the electrode surface. For membrane electrode assemblies (MEA's), the floating electrode technique can be employed to study electrode performance under industrially relevant current densities.[215,216] These techniques have been successfully used in the past to study the stability of other electrocatalytic reactions.

Besides the above suggested approaches, the calculation of a stability number (S-number) allows for an easy quantification and comparison of

electrocatalyst stability.[217] In the past, two similar metrics have independently been proposed for electrocatalyst benchmarking. Kim *et al.*[218] proposed an activity-stability factor (ASF), while Geiger *et al.*[217] suggested the S-number. Although both metrics were first used to describe the stability of iridium-based electrocatalysts during the oxygen evolution reaction (OER), they can easily be expanded to the eCO_2R. For the OER on iridium-based electrocatalysts, the S-number is defined as the ratio between the amount of evolved oxygen and the amount of iridium lost into the electrolyte. Applied to the eCO_2R towards formic acid on a Sn-based electrocatalysts, the S-number can be defined as the amount of produced formic acid molecules per Sn atoms lost into the electrolyte, making it an excellent surface area or catalyst loading independent measure, complementary to the previously discussed techniques, since it doesn't take into account all possible degradation mechanisms.

As exemplified above, several excellent figures of merit, techniques and even standardised stability evaluation protocols, with their own advantages and disadvantages, have already been proposed. However, in order to bring the electrocatalytic CO_2 reduction towards formic acid on Sn-based electrocatalysts towards an industrial feasibility, we propose a combination of multiple stability experiments to be carried out in an electrolyser under industrially relevant operating conditions ($>$100 mA cm^{-2}). Initially, a 48 h stability measurement should be performed with hourly gaseous and liquid product analysis, to benchmark the base Sn-based electrocatalyst performance (FE_{FA}, partial current

density, etc.) and stability. Subsequently, several ADT protocols should be carried out with a 1 hour electrolysis (with gaseous and liquid product quantification) and an *ex situ* an *in operando* (whenever possible) morphological characterisation, before and after every ADT. Hereby, a benchmark electrocatalyst performance and characterization are obtained prior to subjecting the electrocatalyst to an ADT, while the post-ADT one hour electrolysis and *ex situ* morphological characterisation provide valuable information regarding the electrocatalyst degradation and major degradation pathways. These ADT tests include the following: (I) Start-stop conditions should be simulated using potential cycles from OCV to operating potential at a scan rate of 50-100 mV s^{-1}, as the eCO_2R would preferably be powered by intermittent renewable energy sources. Furthermore, (II) a 'total charge passed' ADT should be performed, multiplying the current density (as obtained during the 48h stability measurement) in order to pass the same charge in a shorter timescale. By doing so, more stress will be applied to all components of the electrochemical system and we are able to identify their durability. Finally, (III) several other ADTs, such as elevated temperature or pressure, high electrolyte concentration, and the introduction of CO_2 stream contaminants, are excellent additions to evaluate state-of-the-art Sn-based electrocatalysts under more realistic and industrially relevant operating conditions, which are required once targeting pilot scale electrolysers at higher TRLs.

4.4 Conclusion

State-of-the-art Sn-based electrocatalysts have been reported to reach a FE_{FA} approaching 100% at industrially relevant current densities (>200 mA cm^{-2}). Unfortunately, their electrocatalytic stability (<2400 h) is still inadequate to transpose research towards pilot scale and higher TRLs. Nonetheless, Sn-based electrocatalysts are believed to be a viable option as proof of concept closed "electricity-formate-electricity" loops are currently being demonstrated in literature, reaching an energy efficiency of 30%. Electrocatalyst stability appears to be the final piece to the puzzle as lifetimes in the range of several thousands of hours should be reached. The eCO_2R towards formic acid is expected to reach pilot scale, in the coming years, once this prolonged stability has been attained.

In search for an industrial electrocatalyst, rational Sn-based electrocatalyst design has moved away from bulk Sn, towards advanced nanostructures such as nanoparticles, alloys, core-shell nanoparticles, oxides, sulfides, etc. While this rational design has proven to be beneficial in terms of selectivity and activity, it has also introduced a large array of degradation pathways. A continuation of this rational electrocatalyst design, utilising several mitigation strategies could prolong Sn-based electrocatalyst stability to industrially relevant lifetimes. Furthermore, the need for an adequate stability evaluation and a unified stability testing protocol, has become higher than ever if we want to transpose our research from a laboratory environment to an industrial scale.

In recent literature, several excellent standardised stability evaluation protocols have been proposed. However, needless to say, the electrochemical performance (activity, selectivity and stability) of Sn-based electrocatalysts is highly dependent on the local reaction environment (local pH conditions, mass transfer, etc.), which in turn is influenced by the reactor design (configuration, GDE, membrane, anode, electrolyte, etc.) and experimental parameters (duration, sampling frequency, etc.). When assessing Sn-based electrocatalyst stability, one should thus consider the entirety of the system (electrolyser design/configuration, GDE including cathode electrocatalyst, membrane, anode and electrolyte) and not only focus on optimisation of the Sn-based electrocatalyst, as instability could be introduced by other components than the Sn-based electrocatalyst.

In order to bring the electrocatalytic CO_2 reduction towards formic acid on Sn-based electrocatalysts towards an industrial feasibility, future research should focus on an adequate stability evaluation by means of the discussed metrics, techniques and protocols. Excellent Sn-based electrocatalysts and CO_2 electrolysers are currently being designed by the scientific community. Unfortunately both Sn-based electrocatalysts and electrolysers are being optimised side by side, potentially missing out on a joint optimum.

In the following experimental chapters (Chapters 5 to 7) we focussed solely on enhancing the stability of Sn-based electrocatalysts by examining the possibilities of the particle confinement strategy and investigating the

influence of carbon on the stability and electrochemical performance of Sn-based electrocatalysts. Moreover, we performed an in-depth study concerning the major degradation mechanisms of several self-synthesised Sn-based electrocatalysts and explored pulsed-eCO_2R to further enhance their stability. However, since electrocatalytic degradation was noticed before 24 h, 48 h measurements or ADTs, as proposed in this chapter, weren't performed as the major degradation pathways could already be identified and addressed by performing experiments on a shorter time scale.

Chapter 5

SnO_2 containing nitrogen doped ordered mesoporous carbon electrocatalysts

Driven by rational electrocatalyst design, SnO_2 containing nitrogen doped ordered mesoporous carbon electrocatalysts are synthesised, combining selective SnO_2 with an N-OMC carbon capture medium for the eCO_2R towards FA. The influence of introducing a SnO_2 precursor during the N-OMC synthesis is investigated, while simultaneously elucidating the influence of the N-OMC carbon capture medium and SnO_2 species on the electrochemical performance and studying their electrocatalytic stability and degradation pathways.

This chapter has been submitted as K. Van Daele *et al.*, "Synergy or Antagonism? Exploring the Interplay of SnO_2 and an N-OMC Carbon Capture Medium for the Electrochemical CO_2 Reduction Towards Formate" to *ACS Applied Energy Materials*

5.1 Introduction

Previously, in Chapter 3 (3.1.4 Reaction pathways for the two-electron eCO2R), three possible reaction pathways for the eCO_2R towards FA, all of which are initiated by the adsorption of CO_2 on the electrocatalyst's surface, were discussed.[43,66] Deng *et al.* further uncovered the rate-determining step (RDS) of these reaction pathways to be this first step, the adsorption of CO_2 onto the electrocatalytic active site.[153] Consequently, in order to enhance the overall eCO_2R, the interaction, i.e. adsorption, between the slightly acidic CO_2 molecules and electrocatalyst surface has to be improved in order to fend off the competing hydrogen evolution reaction (HER) and to yield a high selectivity and productivity. In literature, this is frequently achieved by incorporating nitrogen functional groups into carbon support materials.[219] To this extent, nitrogen-doped (N-doped) porous carbon materials are frequently used for efficient CO_2 capture, since the introduction of nitrogen into the carbon matrix increases the surface polarity and basicity, which results in an enhanced CO_2 adsorption.[219–221] Driven by rational electrocatalyst design (Chapter 4), introducing SnO_2, as selective electrocatalyst towards FA, during the synthesis of N-doped carbons should allow to simultaneously functionalize the N-OMC carbon capture medium, facilitate the rate-determining CO_2 adsorption for the eCO_2R towards FA and stabilise the SnO_2 electrocatalytic active sites by particle confinement.[123,197]

In the state-of-the-art, several other SnO_x N-doped carbon electrocatalysts with selectivities reaching up to 80% towards FA have been

reported.[123,222,223] Zhang *et al.,* for example, decorated nitrogen-doped multiwalled carbon nanotubes (N-MWCNTs) with SnO_2 nanoparticles (SnO_2/N-MWCNTs), achieving a FE_{FA} of 46% at an applied potential of -0.9 V vs. Ag/AgCl, compared to only 10% for the supporting N-MWCNTs material, indicating that the incorporation of SnO_2 nanoparticles shifts the eCO_2R selectivity towards formate.[224] These observations were verified by Birdja *et al.*, who revealed the ability of the metal centre of metalloprotoporphyrins to tune the selectivity towards FA. In their research, they found that the FE_{FA} increased with different metal centres, such as In and Sn.[225] Furthermore, Zhao *et al.*, modified an N-doped carbon nanofiber with Sn species to obtain a tuneable electrocatalytic performance towards either CO or formate, depending on the structure of the incorporated Sn species. In their research, they revealed that atomically dispersed Sn species drive the CO_2 conversion towards CO, while Sn nanoparticles promote the electrocatalytic conversion of CO_2 towards FA with a selectivity of 62%.[226] Moreover, Duarte *et al.* reported a tuneable selectivity towards the desired eCO_2R product by altering the embedded transition metal in their metal-nitrogen-doped carbon electrocatalyst. With a partial current density of 70 mA cm^{-2}, their Sn-N-C catalyst achieved a FE of 70% towards FA.[227] Finally, Fu *et al.*, described an electrochemically exfoliated graphene supported 2D confined core-shell structured SnO_2 nanoparticle electrocatalyst, encapsulated into N-doped carbon. The combination of nitrogen dopants and a strong particle confinement effect resulted in a high FE_{FA} of 81.2% at -1.2 V.[123]

In this chapter, N-doped ordered mesoporous carbons (N-OMCs) are functionalised for the eCO_2R towards FA by introducing SnO_2 during the synthesis, yielding SnO_2-N-OMCs. Contrary to previous research, we want to explore the interplay between SnO_2, which is well-known to be selective for the eCO_2R towards FA, and an N-OMC carbon capture medium as support material, which facilitates the rate-determining CO_2 adsorption and could stabilise the SnO_2 active sites through particle confinement. We investigated the influence of introducing a SnO_2 precursor during the N-OMC synthesis, while simultaneously elucidating the influence of the N-OMC carbon capture medium and SnO_2 species on the electrochemical performance and studying their electrocatalytic stability and degradation pathways. Furthermore, we unravelled whether combining SnO_2 with an N-OMC carbon capture medium has a synergistic effect, because of the enhanced CO_2 adsorption, on the eCO_2R. For this purpose, seven different (SnO_2-)N-OMC electrocatalysts were prepared with varying SnO_2 contents, included during various synthesis steps, and with a variable specific surface area (S_{BET}). This allows us to simultaneously investigate the influence of introducing SnO_2 species on the morphology of the N-OMC and more importantly, the influence of the N-OMC support material and SnO_2 species on the electrochemical performance for the eCO_2R towards FA. With a FE_{FA} of 59% for SnO_2-N-OMC (6) and 61% for SnO_2-N-OMC (2), they approached the state-of-the-art (Table 1.1) for Sn-based N-doped carbon electrocatalysts in terms of performance under industrially relevant currents. Furthermore, the SnO_2-N-OMC electrocatalysts require a lower overpotential, courtesy of the N-OMC support, for the selective ($\pm$ 60%)

conversion of CO_2 towards FA at the industrially relevant current density of 100 mA cm^{-2}, compared to these state-of-the-art Sn-based electrocatalysts. Additionally, the 24 h stability of these best performing SnO_2-N-OMC electrocatalysts is explored and their most predominant degradation mechanisms are identified, allowing future research to be steered more precisely towards more stable Sn-based electrocatalysts.

5.2 Experimental

5.2.1 Chemicals

The following chemicals were used as received, without any further purification: acetone (99.5+%, a.r., Chem-Lab), ammonium peroxydisulfate (98%, Alfa Aesar), aniline (99.8%, pure, Acros Organics), 2,3-dihydroxynaphthalene (≥98.0%, Sigma-Aldrich), D520 NAFION® solution (Ion Power), glycerol (a.r., Fisher Scientific), hydrochloric acid (37%, a.r., Chem-Lab), hydrochloric acid (37%, Honeywell chemicals), hydrofluoric acid (40%, VWR chemicals), hydrogen peroxide (35%, Merck), nitric acid (67-70%, Avantor - J.T.Baker), ICP Multi-element standard solution IV (Merck), pluronic® P-123 (PEG-PPG-PEG, average Mn ~5.800, Sigma-Aldrich), potassium hydrogen carbonate (99.5+%, v.p., Chem-Lab), potassium hydroxide (85+%, pellets a.r., Chem-Lab), 2-propanol (99.8+%, iso-propanol a.r., Chem-Lab), sodium hydroxide (99+%, pellets a.r., Chem-Lab), tetraethyl orthosilicate (98%, Acros Organics), tin(II) chloride.2aq (98+%, a.r., Chem-Lab), tin plasma standard solution (Sn 1000ppm, Specpure, Alfa Aesar).

5.2.2 Physicochemical Characterization

Nitrogen physisorption was performed at 77 K, utilising a Quantachrome Quadrasorb SI (Quantachrome Instruments, Boynton Beach, FL, USA) automated surface area & pore size analyzer. Prior to all N_2 physisorption measurements, all samples were degassed at 200 °C for 16 h. The specific surface area (S_{BET}) was calculated using the Brunauer-Emmett-Teller (BET) equation and Quantachrome QuadraWin software.

X-ray Powder Diffraction (XRD) was evaluated using a Bruker D8 ECO powder diffractometer with a LYNXEYE XE-T detector and Cu K-Alpha radiation. SBA-15 samples were probed from 0.5 – 20° 2ϑ, while all (SnO_2-)N-OMC samples were measured from 20 – 80° 2ϑ and compared with the crystallography open database (COD) #1534785 for tetragonal SnO_2.

Raman spectroscopy was performed using a Micro-Raman Horiba (Xplora Plus Microscope) equipped with a 532 nm green laser. Raman spectra were recorded from 750 – 2000 cm^{-1} Raman shift in order to investigate the degree of graphitization. All samples were measured, coated on a glass slide to avoid interference of the carbon based gas diffusion electrode.

X-ray Photoelectron Spectroscopy (XPS) was performed on a PHI-VersaProbe III, equipped with an Al Kα (1486.6 eV) monochromatic X-ray source. An area of Ø 100 µm was measured, using a pass energy of 26 eV for the high-resolution (HR) spectra and an automatic neutralizer. The

wt% is calculated from the atomic concentrations, based on internal standards in the PHI MultiPak software. The high resolution C1s, O1s, N1s and Sn3d5 XPS spectra were processed using the PHI MultiPak software.

Inductively Coupled Plasma Optical Emission Spectroscopy (ICP-OES) was performed on a PerkinElmer Optima 8300 after digestion of the samples in a Milestone Ethos UP microwave digestion system. All (SnO_2-)N-OMC samples were analyzed in twofold. To this extent, 10 mg of each sample was weighed out in a Teflon microwave vessel after which 2 mL of H_2O_2, 8 mL of HNO_3 and 3 mL of HF were added to each vessel. The vessels were left overnight and underwent microwave digestion the following day. After the first digestion, an additional 1 mL of H_2O_2 and 2 mL of HF were added and the microwave digestion was repeated a second time. Finally, 2 mL of HNO_3 and 1 mL of H_2O_2 were added for a third microwave digestion and the digested content of the vessels was transferred and diluted to 50 mL. Before the ICP-OES analysis, the samples were diluted 10 times with 5% HNO_3 to avoid an excessive acid concentration. A blank sample of acids and a calibration series ranging from 5 ppb to 10 ppm of tin and multi-element standard were used for analysis.

High Angle Annular Dark-Field Scanning Transmission Electron Microscopy (HAADF-STEM) as well as Energy Dispersive X-ray Spectroscopy (EDS) has been performed using an aberration-corrected cubed ThermoFisher Scientific Titan transmission electron microscope operating at 200 kV, equipped with a Super X EDS detector. HAADF-

STEM was performed *ex situ* after the electrochemical measurements, by scraping the samples of the GDE, suspending them in ethanol and dropcasting them on Ultra-Thin Film (UTF) carbon-coated Cu TEM grids.

5.2.3 Uncompensated Resistance Determination

The uncompensated resistance R_u (Ohmic drop), was determined by means of a current interrupt measurement, prior to the electrochemical CO_2 reduction experiments. A potential of -4 V vs. Ag/AgCl was applied before triggering the current interrupt circuit and measuring the potential decay over a time period of 2 ms. The uncompensated resistance was obtained from a linear regression between 0 s and 500 µs in the Metrohm Autolab Nova 2.1.5 Software for electrochemical research. All reported potentials were corrected for this resistance after measurement and converted to the RHE scale.

5.2.4 Electrochemical CO_2 Reduction

Gas diffusion electrodes (GDEs) are prepared by spray coating a 25 cm^2 Sigracet 39 BB GDE with an ink made from the synthesized electrocatalyst powders. For one deposition with a target electrocatalyst loading of 1.5 ± 0.1 mg cm^{-2}, the ink consists of 75 mg of the as-synthesized (SnO_2-)N-OMC electrocatalyst, dispersed with 0.375 g of a 5 wt% Nafion solution in approximately 10 mL of a 1:1 Milli-Q (18.2 MΩ·cm @ 25 °C):IPA solution. A large 25 cm^2 GDE is manually spray coated, utilising a Fengda FE-183K airbrush with a 5 mm needle. In order to prevent flooding and assist drying, the GDE is heated to 60 °C while maintaining a moderate air flow

(pressure), speed and distance to assure a homogeneous electrocatalyst coverage. Afterwards, the GDE is divided into 6 smaller GDEs, which are used as cathodes in a small flow-by electrolyzer with a geometric electrochemically active surface area of 1 cm^2.

Electrocatalytic CO_2 reduction experiments of both 1 and 24 hours were conducted by applying a current density of -100 mA cm^{-2} to the aforementioned flow-by electrolyzer. The 0.5 M $KHCO_3$ catholyte is fed single pass at a flow rate of 2 mL min^{-1}, while the 2 M KOH anolyte is recycled at an equal flow rate. A Ni foam is used as counter electrode (anode), while a Nafion 117 membrane and Ag/AgCl reference electrode make up the other components of the electrochemical reactor. Liquid samples were taken after 15 minutes and after 1 hour to determine the FE% towards formate by means of HPLC. For the long-term 24 h electrolysis experiments, additional samples were taken in the course of the first 6 hours and once again after 24 h. The reported data were reproduced and an average value is reported for all FE_{FA} and iR-compensated potentials.

5.3 Synthesis

5.3.1 Preparation of the SBA-15 hard template

In a typical SBA-15 synthesis, 1.8 g Pluronic® P-123 and 1.8 g glycerol were stirred overnight in 69 g of a 1 M hydrochloric acid (HCl) aqueous solution, at 35 °C, in a polypropylene (Nalgene®) bottle. Next, 3.87 g tetraethyl orthosilicate (TEOS) was added dropwise to the mixture under

vigorous stirring. Subsequently, the mixture was kept at 35 °C for an additional 24 h under static conditions. Afterwards, a hydrothermal treatment was performed at 100 °C for 24 h. Finally, the solid product was collected by filtration, washed with distilled water until pH 4-5 and dried overnight at 80 °C. The resulting white powder was calcined at 550 °C for 6h (1°C min^{-1}) in flowing air, in order to remove the organic structure directing agent (SDA).[228,229]

5.3.2 Fabrication of the SnO_2-N-OMC electrocatalyst

SnO_2 N-doped ordered mesoporous carbon (SnO_2-N-OMC) materials were prepared using a two-step procedure (Figure 5.1), inspired by and adapted from Wang *et al.*[230] and Sheng *et al.*,[228] respectively. The SnO_2 precursor ($SnCl_2.2H_2O$) was included either completely during addition of the aniline or 2,3-dihydroxynaphthalene or divided between both steps, as depicted in Figure 5.1. A detailed overview of the performed syntheses can be found in Table 5.1.

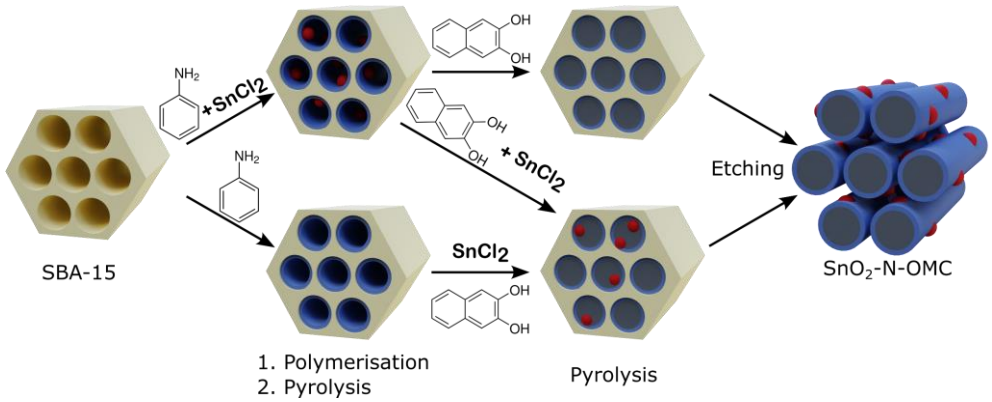

Figure 5.1 Synthesis method SnO_2 nitrogen-doped ordered mesoporous carbon electrocatalysts.

As a first step, aniline was polymerized inside the pores of the SBA-15 hard template. The amount of aniline employed in this step was chosen in order to cover the SBA-15 surface with an aniline monolayer.[228] Therefore, approx. 0.5 g of the SBA-15 hard template was added to ±200 mL of the 0.5 M HCl aqueous solution and stirred for 15 minutes. Afterwards, the appropriate amount of aniline, calculated from the mass and specific surface area (S_{BET}) of the SBA-15 hard template and cross-sectional area (43 $Å^2$) and density (1.02 g cm^{-3}) of aniline, was added and the whole mixture was stirred for 1 h in an ice bath.

Table 5.1 Detailed overview (SnO_2-)N-OMC Syntheses

Catalyst	Hard Template	Aniline (mL)	APS (g)	2,3-DHN (g)	$SnCl_2.2H_2O$ (g)	Step
N-OMC (1)	SBA-15 (1)	0.182	0.5454	0.7000	0	/
SnO_2-N-OMC (1)	SBA-15 (2)	0.185	0.5557	0.6982	0 0.1	Aniline 2,3-DHN
SnO_2-N-OMC (2)	SBA-15 (3)	0.179	0.5364	0.6491	0.4 0	Aniline 2,3-DHN
SnO_2-N-OMC (3)	SBA-15 (4)	0.182	0.5454	0.6366	0.3 0.1	Aniline 2,3-DHN
SnO_2-N-OMC (4)	SBA-15 (5)	0.221	0.6618	0.7788	0 0.4	Aniline 2,3-DHN
SnO_2-N-OMC (5)	SBA-15 (6)	0.179	0.5374	0.6778	0.1 0.3	Aniline 2,3-DHN
SnO_2-N-OMC (6)	SBA-15 (7)	0.168	0.5035	0.6323	0.2 0.2	Aniline 2,3-DHN

Finally, a 1.2 molar excess of the radical initiator ammonium peroxydisulfate (APS), dissolved in ±50 mL of the 0.5 M HCl aqueous solution, was added and the mixture was stirred for 24 h in an ice bath. Afterwards, the solvent was removed in a rotary evaporator and the sample

was dried in an oven at 100 °C. The sample was then placed into the tubular furnace where it underwent a pyrolysis for 3 h at 900 °C (3.3 °C min^{-1}) under constant Argon (Ar) flow (1 cm^3 s^{-1}). In the second step of the synthesis, the remaining pore volume of the SBA-15 was loaded with carbon. The required amount of 2,3-dihydroxynaphthalene (2,3-DHN) was calculated using the remaining pore volume of the SBA-15 hard template and the density of 2,3-DHN (1.33 g cm^{-3}). The as obtained grey solid from the first step was mixed with the appropriate amount of 2,3-DHN, in acetone as a solvent, and allowed to stir at room temperature for 24 h. After evaporation of the solvent, the composite material was thermally treated for 2 h at 300 °C (3.3 °C min^{-1}) under a continuous Ar flow (1 cm^3 s^{-1}), before washing the sample 3 times with acetone, collecting the sample by filtration and drying it overnight. A final pyrolysis was then performed at 900 °C (3.3 °C min^{-1}) for 5 h under an Ar atmosphere (1 cm^3/s). Finally, the silica template was removed by suspending the as obtained black solid in a 2 M sodium hydroxide aqueous solution while stirring for 8 h at 100 °C under reflux. The SnO_2-N-OMC material in the form of a black solid was collected by filtration and dried at 100 °C.[228,229]

5.4 Results and discussion

5.4.1 Physicochemical characterization

Similar to the SBA-15 hard template (physicochemical characterization in SI, Figure S5.1), N-OMC materials are known to have a well-ordered high specific surface area.[228,229] The effect of incorporating SnO_2 species during the synthesis on the specific surface area and structure of the N-OMC

support material was investigated by nitrogen physisorption, utilising the BET equation to calculate the specific surface area. The adsorption-desorption isotherms of all (SnO_2-)N-OMCs, as depicted in Figure 5.2, are classified as a composite Type IVa + Type II isotherm with a clear hysteresis. Type IVa isotherms are indicative of mesoporous adsorbents and typically end in a final, nearly horizontal, saturation plateau near $P/P_0 = 1$. Type II isotherms, on the other hand, are characterized by the unrestricted monolayer-multilayer adsorption on nonporous or macroporous adsorbents, resulting in the absence of a plateau near $P/P_0 = 1$. Given that the adsorbed amount appears to increase infinitely when $P/P_0 = 1$, indicating either interparticle adsorption or the presence of macropores, but hysteresis does manifest, pointing towards mesopores, all samples were classified as a composite Type IVa + Type II isotherm.

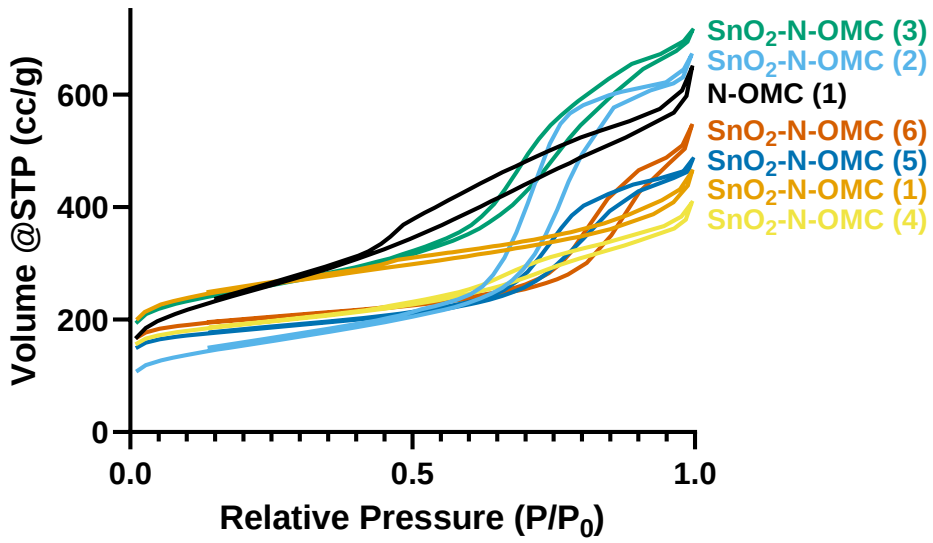

Figure 5.2 Nitrogen adsorption-desorption isotherms (SnO_2-)N-OMC electrocatalysts.

According to the recommendation in the IUPAC technical report, the total pore volume of such a composite Type IVa + Type II isotherm cannot accurately be evaluated since the isotherm is not horizontal near $P/P_0 = 1$. Nevertheless, the pore volume was derived from the adsorbed amount close to unity (i.e. $P/P_0 \approx 0.95$) by means of the Barrett, Joyner and Halenda (BJH) method to at least get an indication.[231] The specific surface areas, corresponding pore volumes and sizes are summarized in Table 5.2. The BET surface area and pore size distribution plots are provided in the supporting information (Fig. S5.2).

Table 5.2 Morphological properties of the (SnO_2-)N-OMC electrocatalysts

Catalyst	S_{BET}	Pore volume ($cm^3\ g^{-1}$)*	Pore size (nm)**
N-OMC (1)	856	0.88	-
SnO_2-N-OMC (1)	952	0.63	-
SnO_2-N-OMC (2)	547	0.96	7.0
SnO_2-N-OMC (3)	925	1.05	4.5
SnO_2-N-OMC (4)	722	0.56	-
SnO_2-N-OMC (5)	689	0.70	4.1
SnO_2-N-OMC (6)	767	0.74	3.9

*The pore volume was derived from the adsorbed amount close to unity (i.e. $P/P_0 \approx 0.95$) by means of the Barrett, Joyner and Halenda (BJH) method to get an indication since it is conventionally not determined for composite Type IVa + Type II isotherms.

**Not all pore sizes could be determined using the BJH method because of the composite Type IVa + Type II isotherms.

Based on the adsorption-desorption isotherms, N-OMC (1) displays a type H2 hysteresis, indicating blocked pores. Furthermore, SnO_2-N-OMC (1) and SnO_2-N-OMC (4) appear to be the only two samples with a less neatly

ordered mesoporous structure, nonetheless having a high specific surface area, as their isotherms have a higher resemblance to a Type II isotherm for nonporous or macroporous materials. Nonetheless, both SnO_2-N-OMC (1) and SnO_2-N-OMC (4) isotherms contain hysteresis, indicating the presence of cylindrical (meso)pores, larger than ~4 nm.[231] Interestingly, these are the only two SnO_2-N-OMC samples where the entirety of the $SnCl_2$ precursor was added simultaneously with the 2,3-dihydroxynaphthalene. All other SnO_2-N-OMC adsorption-desorption isotherms have a closer resemblance to a Type IVa isotherm, indicating well-ordered mesoporous materials. These observations seem to imply that it is important to at least add a part of the $SnCl_2$ precursor simultaneously with the aniline and that adding the entire $SnCl_2$ precursor during the 2,3-DHN step appears to hinder the formation of a neatly ordered mesoporous carbon structure. Visual confirmation of the ordered mesoporous carbon structure was obtained via electron microscopy (Fig. S5.3) and confirmed these initial observations.

For Type II and Type IVa isotherms, the linearity of the BET plot is limited to a part of the isotherm, most commonly in the relative pressure range of ~0.05 – 0.30. However, for our SnO_2-N-OMC materials, this BET range is shifted towards lower relative pressures due to the high adsorption energy of the nitrogen on the graphitized carbon.[231] The as-synthesized SnO_2-N-OMC materials have a varying surface area, pore volume and pore size. Here, it is again apparent that both the SnO_2-N-OMC (1) and SnO_2-N-OMC (4) electrocatalysts have a less neatly ordered mesoporous

structure since both samples accommodate the lowest pore volume. Nevertheless, according to these physisorption results, all SnO_2-N-OMC electrocatalysts possess a high surface area (> 500 m^2 g^{-1}) and a high volume of (meso)pores, which is promising for their role as a CO_2 capturing agent. This variety in S_{BET}, which is (partially) inherent to the SnO_2-N-OMC synthesis, allows us to explore the influence of the N-OMC support material on the electrochemical performance of the SnO_2 species for the eCO_2R towards formate.

Information related to the degree of graphitization (i.e. the ratio of the areas of the D and G bands) and knowledge concerning the crystalline structure, chemical nature and space group symmetry were obtained by Raman spectroscopy and XRD, respectively.

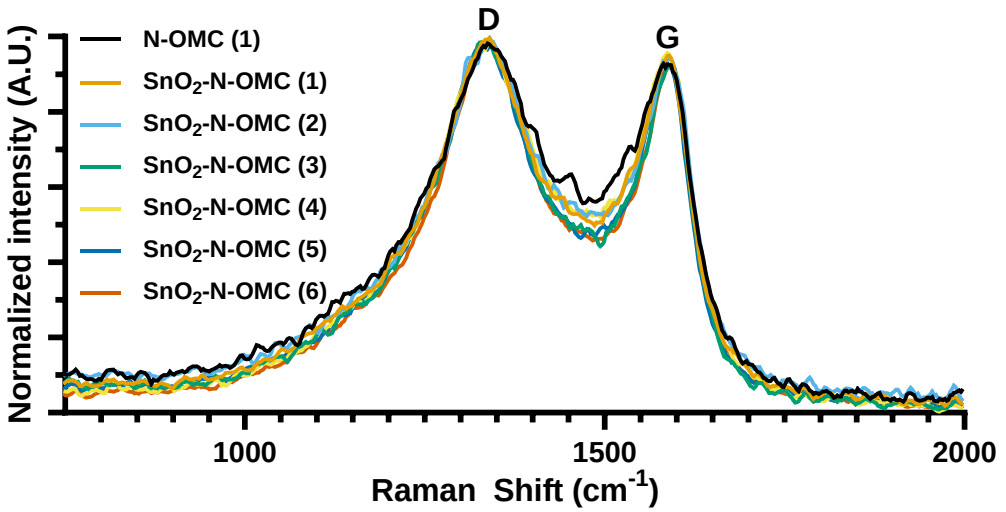

Figure 5.3 Normalized Raman spectra of the as-synthesized (SnO_2-)N-OMC electrocatalysts, recorded between 750 and 2000 cm^{-1} with a 532 nm green laser.

The normalized Raman spectra (Figure 5.3) display two broad peaks at 1350 cm^{-1} and 1600 cm^{-1}, the former usually referred to as the D-band,

originating from edge defects of the graphitic domain, and the latter identified as the G-band, which is assigned to planar vibration of sp^2 carbon atoms in an ideal graphitic layer.[228,232,233] Since the ratio of the areas of the D and G bands (I_D/I_G), which is inversely proportional to the degree of graphitization, is >1 and comparable for all samples, we can conclude that all SnO_2-N-OMC electrocatalysts have a clear graphitic character, despite amorphous segments, and that the addition of an SnO_2 precursor during the N-OMC synthesis had no major influence on the resulting degree of graphitization of the N-OMC.[228]

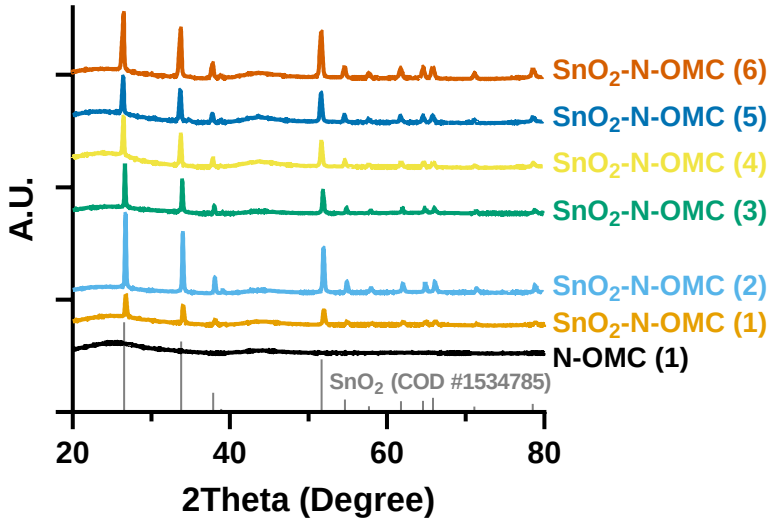

Figure 5.4 Wide angle X-ray diffractogram of the as-synthesized (SnO_2-)N-OMC catalysts, compared with the Crystallography Open Database (COD) #1534785 for tetragonal SnO_2.

The wide angle diffractograms (Figure 5.4) display the typical diffraction pattern with peaks at 2ϑ = 26.5°, 33.8°, 37.9°, 38.9°, 42.6°, 51.7°, 54.7°, 57.7°, 61.8°, 64.6°, 65.8°, 71.1° and 78.5°, present in all SnO_2-N-OMC samples. These peaks are attributed to reflections of the (110), (101), (200), (111), (120), (211), (220), (002), (130), (112), (301), (202) and (321) planes,

respectively, of tetragonal SnO_2 (COD #1534785).[234,235] Additionally, two broad and weak peaks are observed in the N-OMC diffractogram at approximately 25° and 43.5° 2ϑ, which correlate to amorphous carbon and are likewise observed in the diffractograms of the SnO_2-N-OMC catalysts.[236] Again, no distinctive differences are observed in terms of the crystalline structure and chemical nature of the SnO_2 species, which are all confirmed to be tetragonal SnO_2. This allows for differences in the electrochemical performance to be attributed solely to the morphology of the SnO_2 species, SnO_2 loading and influences of the N-OMC support material.

5.4.2 Electrochemical CO_2 reduction

The electrochemical performance of the (SnO_2-)N-OMC electrocatalysts was investigated in a small flow-by electrolyzer with a geometric surface area of 1 cm^2 (Figure S5.4). By performing a 1 h chronopotentiometric experiment at a constant applied current density of 100 mA cm^{-2}, the average iR-compensated cathodic operating potential (Figure 5.5a) and FE_{FA} (Figure 5.5b) were determined.

Several trends are observed when looking at the electrocatalytic performance of the (SnO_2-)N-OMCs. First, the pristine nitrogen doped ordered mesoporous carbon material (N-OMC (1)) has a low average FE_{FA} of 8% and a continuously increasing cathodic potential over the course of 1 h, indicating that on its own it is not suited for the electrochemical reduction of CO_2 to formate. Interestingly, this trend of an increasing cathodic potential appears to diminish by combining the N-OMC with

SnO_2 species, as evidenced by the potential-time curves of the SnO_2-N-OMC electrocatalysts. SnO_2-N-OMC (1) has the lowest amount of SnO_2 and already exhibits a significantly smaller slope, compared to the blank N-OMC. Moreover, upon further increasing the SnO_2 content, a constant cathodic potential is achieved. Therefore, this continuously increasing cathodic potential is hypothesized to originate from the blocking of active sites due to inefficient conversion of adsorbed CO_2 by the N-OMC or the competing HER which increases the local pH, resulting in less protons and an increasing potential to maintain a constant current at low FE_{FA}.

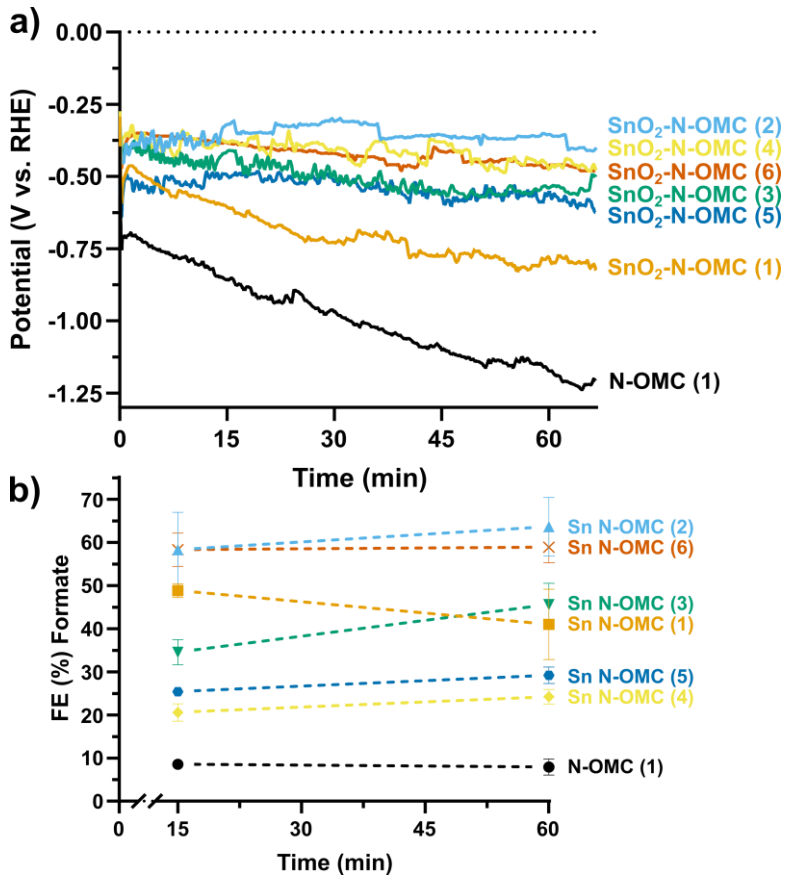

Figure 5.5 a) average iR-compensated potential (V vs. RHE) and b) average FE% towards formate with error bars, plotted as a function of time at a constant current density of 100 mA cm^{-2} for 1 h.

Second, the addition of SnO_2 species boosts the electrocatalytic selectivity towards formate from 8% for the blank N-OMC (1) to 59% and 61% for the SnO_2-N-OMC (6) and SnO_2-N-OMC (2) electrocatalysts, respectively, as such approaching the state-of-the-art of comparable materials (Table 1.1). The combination of high current densities and low overpotentials with a selectivity of around 60% puts our materials at the same level or above the state-of-the-art in the field. The SnO_2 species are thus far more active for the eCO_2R towards FA and appear to predominantly determine the electrochemical performance, suppressing the electrochemical behavior of the N-OMC which was initially expressed by the continuously decreasing potential and a low selectivity towards formate.

In terms of selectivity, a wide variety, ranging from an average 22% for SnO_2-N-OMC (4) to 61% for SnO_2-N-OMC (2), was obtained by incorporating equal amounts of SnO_2 precursor during different steps of the N-OMC synthesis.

ICP-OES and XPS analysis (Table 5.3 and Figure S5.5), however, revealed that while equal amounts of Sn precursor were added in most of the syntheses, most of the Sn wasn't retained in the final material, providing a widely varying amount of SnO_2 that was actually included. Moreover, upon comparing the Sn content, as determined by ICP-OES and XPS, it becomes clear that most of the Sn is present on the surface of the SnO_2-N-OMC electrocatalyst material and not incorporated inside the mesoporous carbon structure.

Table 5.3 Average composition of the (SnO_2-)N-OMC electrocatalysts in wt%, as determined by a) ICP-OES and b) XPS (in duplicate)

Catalyst	Sn[a] (wt%)	Sn[b] (wt%)	C[b] (wt%)	N[b] (wt%)	O[b] (wt%)
N-OMC (1)	0.06 ± 0.02	0.00 ± 0.00	90.27 ± 0.48	2.06 ± 0.19	7.67 ± 0.67
SnO_2-N-OMC (1)	0.24 ± 0.03	-	-	-	-
SnO_2-N-OMC (2)	1.15 ± 0.01	2.47 ± 0.18	90.91 ± 0.68	0.32 ± 0.13	6.30 ± 0.37
SnO_2-N-OMC (3)	0.55 ± 0.09	-	-	-	-
SnO_2-N-OMC (4)	0.69 ± 0.10	3.33 ± 0.41	87.79 ± 0.05	0.98 ± 0.09	7.90 ± 0.28
SnO_2-N-OMC (5)	1.13 ± 0.13	-	-	-	-
SnO_2-N-OMC (6)	0.57 ± 0.10	4.44 ± 0.27	86.00 ± 0.03	0.22 ± 0.04	9.34 ± 0.26

Low and high magnification HAADF-STEM imaging combined with EDS elemental mapping confirmed the presence of a wide variety of SnO_2 species, ranging from large irregular SnO_2 species to differently sized SnO_2 nanoparticles, as depicted in figure S5.6, all of them having the rutile tetragonal SnO_2 structure (space group: $P4_2/mnm$). These SnO_2 species are too large to fit inside the N-OMC pores and are thus mostly found at the outer part of the mesoporous carbon support. In addition, crystalline and non-crystalline atomic clusters, which have a significantly higher contrast compared to their background in high resolution HAADF-STEM images, lay among the N-OMC matrix. EDS elemental mapping of these clusters only showed carbon and silicon signals from the N-OMC, without a clear presence of Sn. This spectroscopy based result can be attributed to the small size of these clusters and their sensitivity under the electron beam, which allowed us to only use very short acquisition times. However, the analysis of the high resolution data of these crystalline clusters (Figure

S5.6B) confirms that, similar to the bigger SnO_2 species (Figure S5.6C, F),[226] the interatomic distances are in agreement with the d-spacings of rutile SnO_2, a strong indication that they are Sn-based.

SnO_2-N-OMC (2) and SnO_2-N-OMC (6), respectively, enclose considerably larger irregular SnO_2 species and differently sized SnO_2 nanoparticles, than the least performing electrocatalyst, SnO_2-N-OMC (4). Considering that Zhao *et al.* reported atomically dispersed Sn species to promote the eCO_2R towards CO and Sn nanoparticles are more selective towards formate, it is obvious that the large irregular SnO_2 species and/or the SnO_2 nanoparticles of different sizes are crucial and dominate the electrochemical performance of the SnO_2-N-OMC electrocatalysts when formate is the target product.[226] The moderate electrochemical performance of the other three SnO_2-N-OMC electrocatalysts (1, 3 and 5) highlights that the morphology of the SnO_2 species appears to be more important than the SnO_2 loading. Nonetheless, these SnO_2-N-OMC electrocatalysts seemingly have less selective SnO_2 species, compared to the best performing SnO_2-N-OMCs, resulting in a lower FE_{FA}.

In summary, the observed electrochemical performance of the SnO_2-N-OMC electrocatalysts is a result of the combined behavior of the N-OMC (S_{BET} surface area, N-dopant, conductivity, etc.) support and the different SnO_2 species. As demonstrated, the N-OMC material independently is not suited for the selective eCO_2R towards FA, which is why the amount and morphology of the SnO_2 species make the largest contribution to the electrochemical performance (especially selectivity) of the SnO_2-N-OMC

electrocatalysts. Furthermore, the enhanced CO_2 adsorption by virtue of the N-OMC support material appears to positively influence the overpotential, when comparing the required overpotential for the SnO_2-N-OMC electrocatalysts with the state-of-the-art in Table 1.1. As a result, all SnO_2-N-OMC electrocatalysts demand a lower overpotential for the conversion of CO_2 towards FA at the industrially relevant current density of 100 mA cm^{-2}. The N-OMC support material itself, requires the largest overpotential, as depicted in Figure 5.5a, presumably caused by the poor conversion of the more easily adsorbed CO_2. However, we have demonstrated that we are able to significantly increase the FE_{FA} and lower the overpotential, utilising a minimal amount of SnO_2 species, with the most selective morphologies being large irregular SnO_2 species and heterogeneous SnO_2 nanoparticles. An optimal combination of both the SnO_2 species and the N-OMC carbon capture medium could thus result in a synergistic effect for the eCO_2R towards FA.

The long-term electrocatalytic performance and degradation pathways of the two best performing electrocatalysts (SnO_2-N-OMC (2) and SnO_2-N-OMC (6)) were evaluated by performing a 24 h chronopotentiometric experiment at an applied current density of 100 mA cm^{-2}, combined with *ex situ* HAADF-STEM imaging. After starting at a similar FE_{FA} of approximately 60%, the SnO_2-N-OMC (2) and SnO_2-N-OMC (6) electrocatalysts start to display a difference in stability after only 2 h of electrolysis at 100 mA cm^{-2}, as depicted in Figure 5.6. Whereas the FE_{FA} of SnO_2-N-OMC (2) increases to an average of 64% over the course of the

first 6 hours, the selectivity of the SnO_2-N-OMC (6) decreases to 28% after 6 h and even further to 12% at –0.95 V vs. RHE after 24 h. Eventually, after 24 h of operation, the FE_{FA} of SnO_2-N-OMC (2) decreases to an average of 43% at an operating potential of -0.60 V vs. RHE.

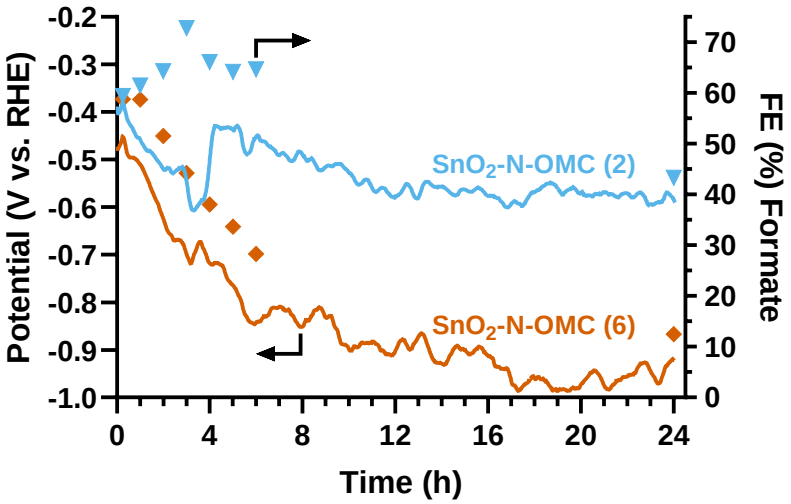

Figure 5.6 average iR-compensated potential (V vs. RHE) and FE% towards formate of the SnO_2-N-OMC (2) and SnO_2-N-OMC (6) electrocatalysts, plotted as a function of time at a constant current density of 100 mA cm^{-2} for 24 h.

Ex situ HAADF-STEM imaging of both electrocatalysts after 24 h of electrolysis (Figure 5.7A, B) reveals the morphological degradation of the large SnO_2 species, which are pulverized and agglomerated, similar to the deterioration reported by Wu *et al.*[73] The dissimilar long-term electrocatalytic performance can be ascribed to a combination of morphological (pulverization and agglomeration) and chemical (*in situ* SnO_2 reduction towards metallic Sn) deterioration. The loss of selectivity of the SnO_2-N-OMC (2) electrocatalysts due to the *in situ* SnO_2 reduction, is temporarily offset by the pulverization providing additional SnO_2 active sites for the eCO_2R towards FA. In the case of SnO_2-N-OMC (6), the

initial SnO_2 species were already significantly smaller than the ones present in SnO_2-N-OMC (2), leading towards less pulverization (and more agglomeration) and consequently to less fresh SnO_2 sites being formed to offset the *in situ* SnO_2 reduction and more rapid loss in selectivity as a result (Figure 5.6).

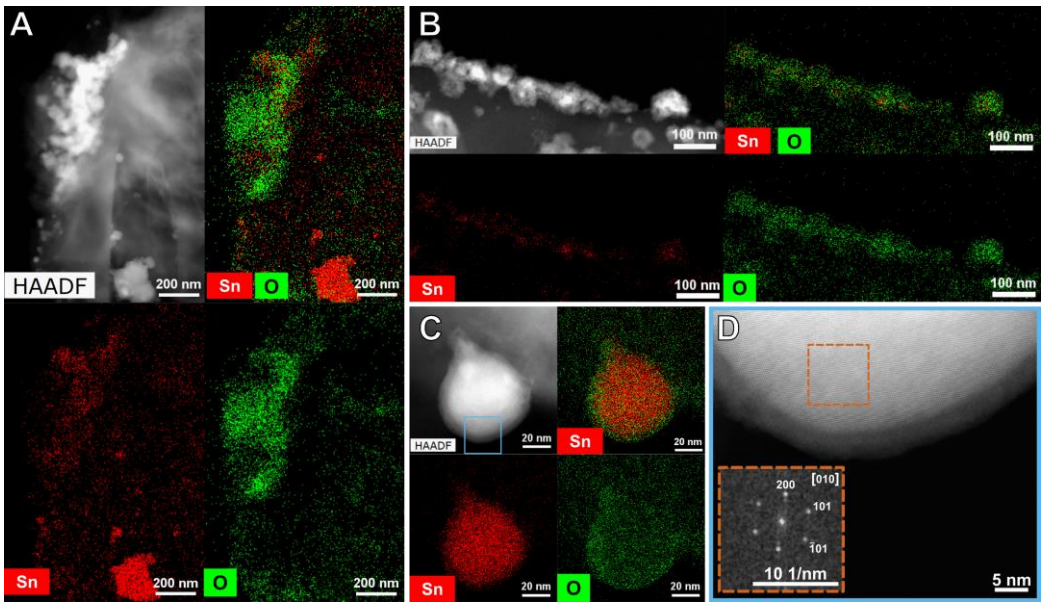

Figure 5.7 HAADF-STEM images and EDS elemental maps quantified for atomic % of A) SnO_2-N-OMC (2), B) SnO_2-N-OMC (6) after 24 h of electrolysis at 100mA cm^{-2} and C, D) HAADF-STEM images with the corresponding FT pattern and EDS elemental maps quantified for atomic % of a partially re-oxidized in situ reduced Sn nanoparticle in SnO_2-N-OMC (2).

This *in situ* SnO_2 reduction to metallic Sn (space group: $I4_1/amd$), as observed by *ex situ* HAADF-STEM imaging and the corresponding Fourier Transform pattern, combined with quantified (for atomic %) EDS elemental mapping (Figure 5.7C, D) in both SnO_2-N-OMC electrocatalysts after 24 h of electrolysis, is determined to be the most detrimental degradation pathway, resulting in the direct loss of selectivity. While

morphological stability of the Sn-based electrocatalyst is important in the long run, chemical stability to withstand *in situ* SnO_2 reduction appears to be more crucial as this directly correlates to a more severe loss of selectivity.

5.5 Conclusion

In conclusion, we have demonstrated that including SnO_2 during the N-OMC synthesis has no significant effect on the N-OMC morphology, as long as part of the SnO_2 precursor is added simultaneously with the aniline. Including a SnO_2 precursor during different stages of the N-OMC synthesis resulted in a wide variety of SnO_2 species, ranging from large irregular SnO_2 species to differently sized SnO_2 nanoparticles and Sn-based atomic clusters. More importantly, we have successfully demonstrated that we are able to significantly increase the FE_{FA} utilising a minimal amount of SnO_2, with the most selective morphologies being large irregular SnO_2 species and SnO_2 nanoparticles. Moreover, the SnO_2-N-OMC electrocatalysts require a low overpotential, courtesy of the N-OMC support, for the selective ($\pm$ 60%) conversion of CO_2 towards FA at the industrially relevant current density of 100 mA cm^{-2}. As such, they perform better or at least as good as the current state-of-the-art. Finally, the long-term electrocatalytic stability and degradation pathways of the two best performing electrocatalysts (SnO_2-N-OMC (2) and SnO_2-N-OMC (6)) were unravelled by combining 24 h chronopotentiometric experiments at an applied current density of 100 mA cm^{-2} with *ex situ* HAADF-STEM. While the FE_{FA} of SnO_2-N-OMC (6) decreased from 59% to 12% over the course

of 24 h, the SnO_2-N-OMC (2) electrocatalyst displayed a smaller loss in FE_{FA} from 61% to 43%. This loss of selectivity was attributed to the *in situ* SnO_2 reduction, which in the case of the latter electrocatalysts is more offset by the pulverization of large SnO_2 species, revealing 'fresh' and selective SnO_2 active sites for the eCO_2R towards FA. While morphological stability of the Sn-based electrocatalyst is thus important in the long run, chemical stability to withstand *in situ* SnO_2 reduction appears to be more crucial for future Sn-based electrocatalysts as this directly correlates to a severe loss in selectivity. Our exploration of the interplay between SnO_2 and the N-OMC carbon capture medium support material revealed that an optimal combination of both the SnO_2 species and the N-OMC carbon capture medium could thus result in a synergistic effect for the eCO_2R towards FA, especially when utilization of the N-OMC support material and incorporation of the SnO_2 species is optimized to morphologically stabilize the SnO_2 active species. Hence, future research concerning Sn-based electrocatalysts should focus on improving the morphological and chemical stability in order to yield industrially relevant Sn-based electrocatalysts for the eCO_2R towards FA. Therefore, in chapter 6, pomegranate-structured SnO_2 and SnO_2@C electrocatalysts are synthesised, utilising the particle confinement strategy, in an attempt to acquire a better performing and more stable electrocatalyst than the SnO_2-N-OMC electrocatalysts. The use of the carbon shell is hypothesised to act as a protective layer, physically inhibiting morphological degradation and diminishing the *in situ* SnO_2 reduction.

5.6 Supporting information

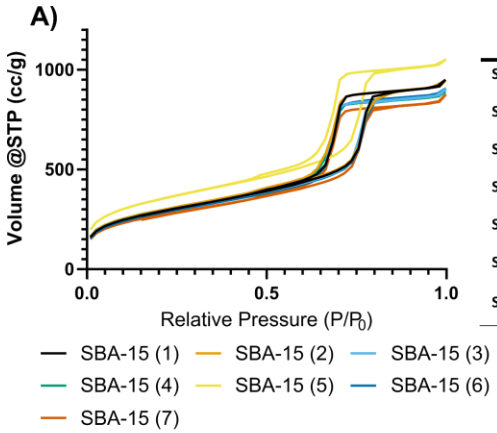

Catalyst	S_{BET} ($m^2\ g^{-1}$)	Pore volume ($cm^3\ g^{-1}$)	Pore size (nm)
SBA-15 (1)	1023	1.4	5.5
SBA-15 (2)	1040	1.4	5.4
SBA-15 (3)	1017	1.3	5.3
SBA-15 (4)	1038	1.3	5.1
SBA-15 (5)	1226	1.6	5.2
SBA-15 (6)	995	1.3	5.4
SBA-15 (7)	950	1.3	5.4

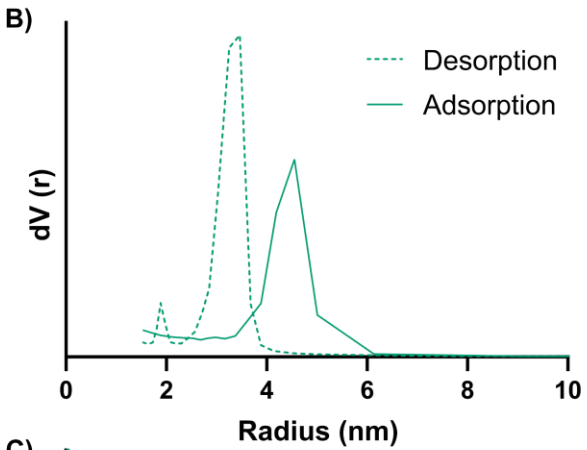

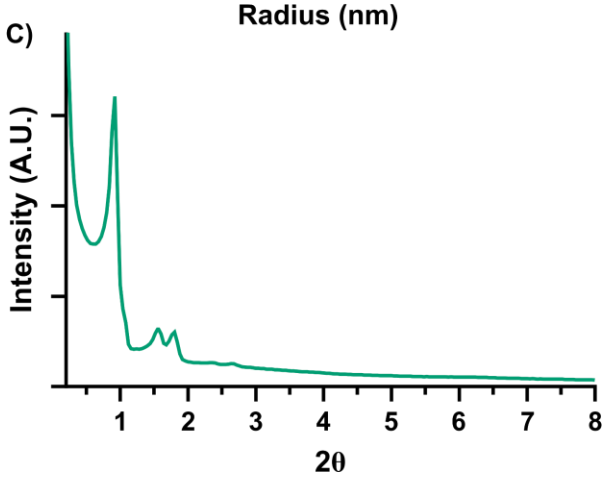

Figure S5.1 Physicochemical characterization SBA-15 with A) nitrogen adsorption-desorption isotherms of all SBA-15 samples, B) BJH pore size distribution of SBA-15 (4) and C) Low Angle XRD of SBA-15 (4).

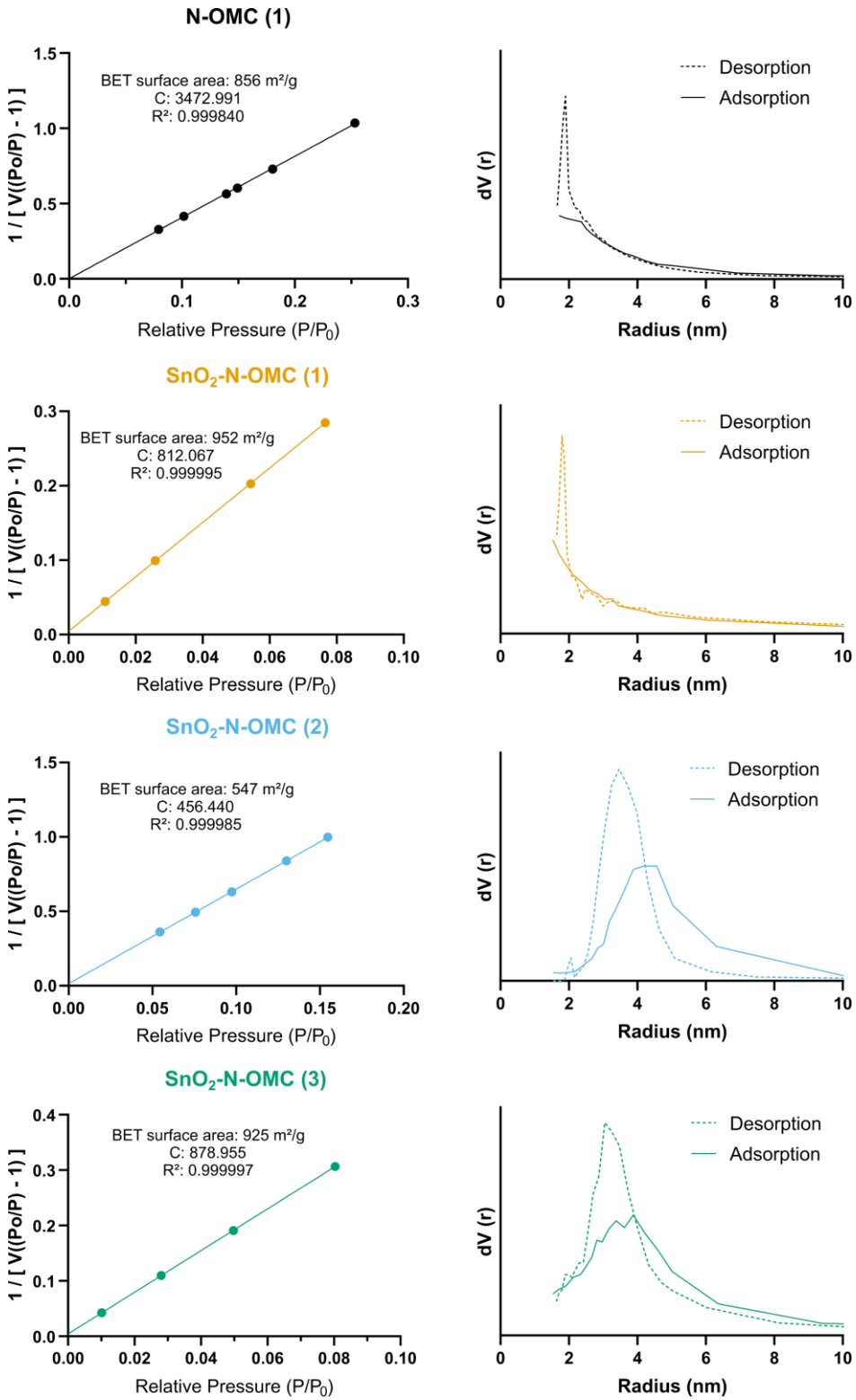
N-OMC (1)
BET surface area: 856 m²/g
C: 3472.991
R²: 0.999840
1 / [V((Po/P) - 1)]
Relative Pressure (P/P0)
Desorption
Adsorption
dV (r)
Radius (nm)
SnO2-N-OMC (1)
BET surface area: 952 m²/g
C: 812.067
R²: 0.999995
1 / [V((Po/P) - 1)]
Relative Pressure (P/P0)
Desorption
Adsorption
dV (r)
Radius (nm)
SnO2-N-OMC (2)
BET surface area: 547 m²/g
C: 456.440
R²: 0.999985
1 / [V((Po/P) - 1)]
Relative Pressure (P/P0)
Desorption
Adsorption
dV (r)
Radius (nm)
SnO2-N-OMC (3)
BET surface area: 925 m²/g
C: 878.955
R²: 0.999997
1 / [V((Po/P) - 1)]
Relative Pressure (P/P0)
Desorption
Adsorption
dV (r)
Radius (nm)

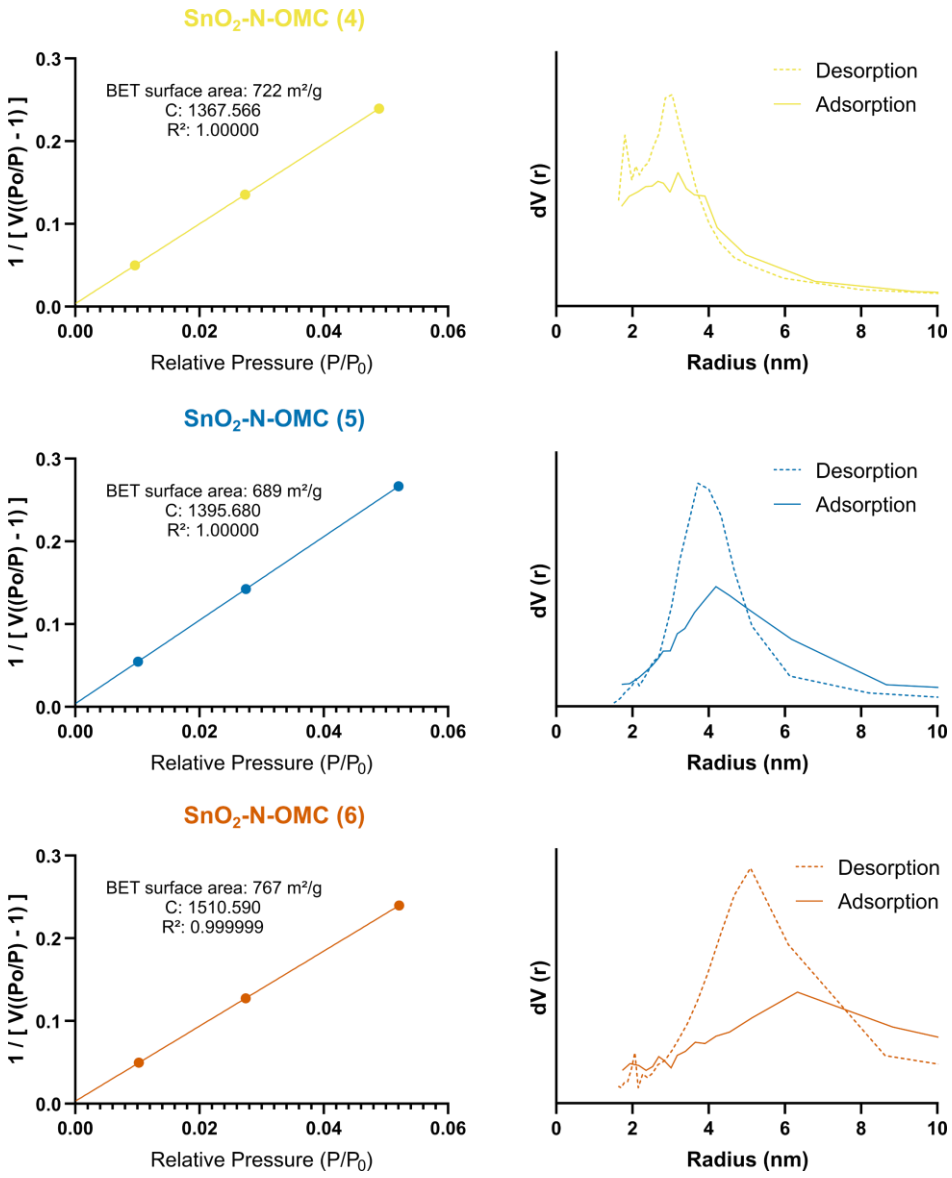

Figure S5.2 BET surface area and pore size distribution plots of all (Sn-)N-OMC electrocatalysts.

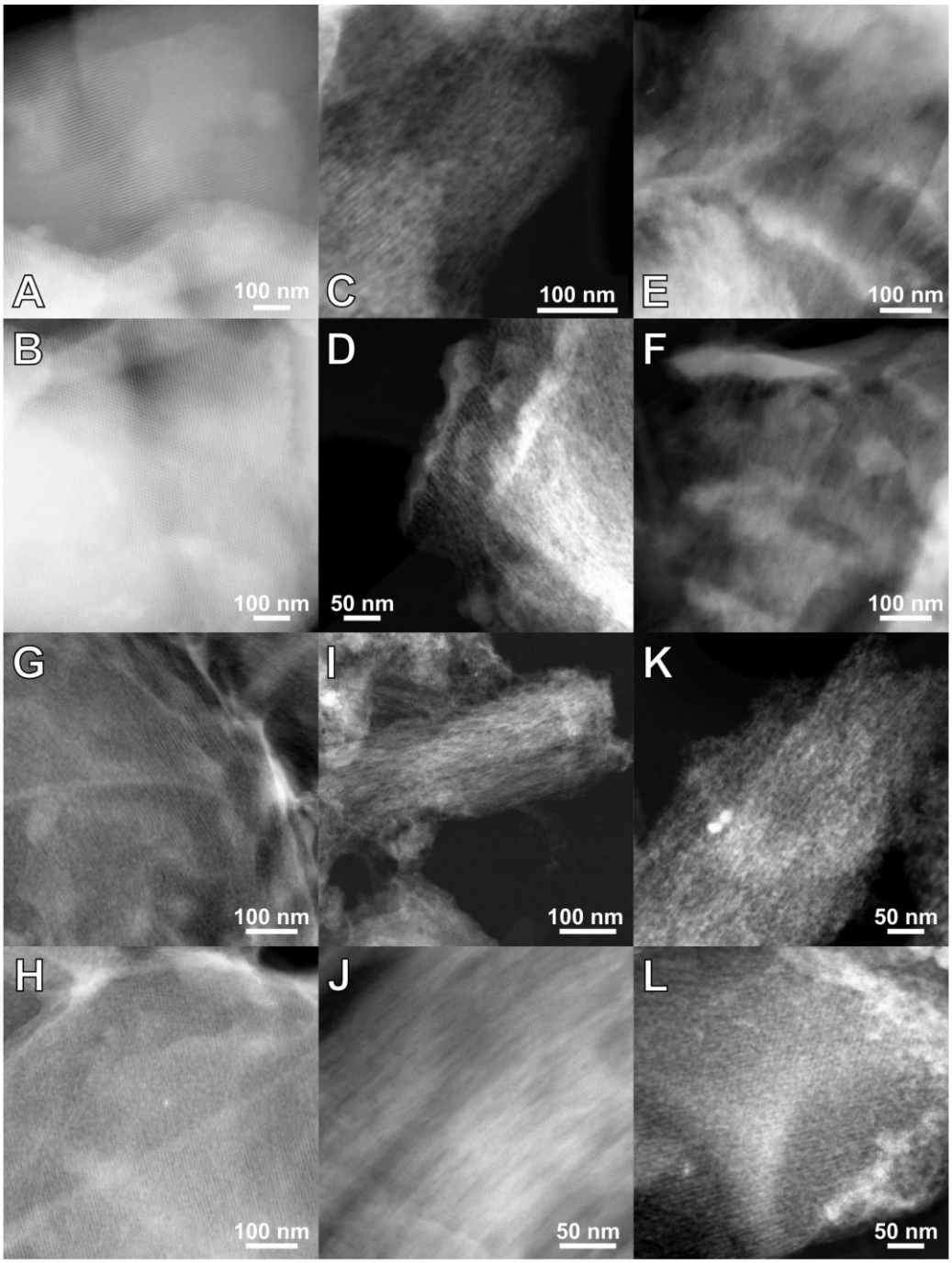

Figure S5.3 HAADF STEM images of A, B) SBA-15; C, D) N-OMC (1); E, F) SnO_2-N-OMC (1); G, H) SnO_2-N-OMC (2); I, J) SnO_2-N-OMC (4) and K, L) SnO_2-N-OMC (6).

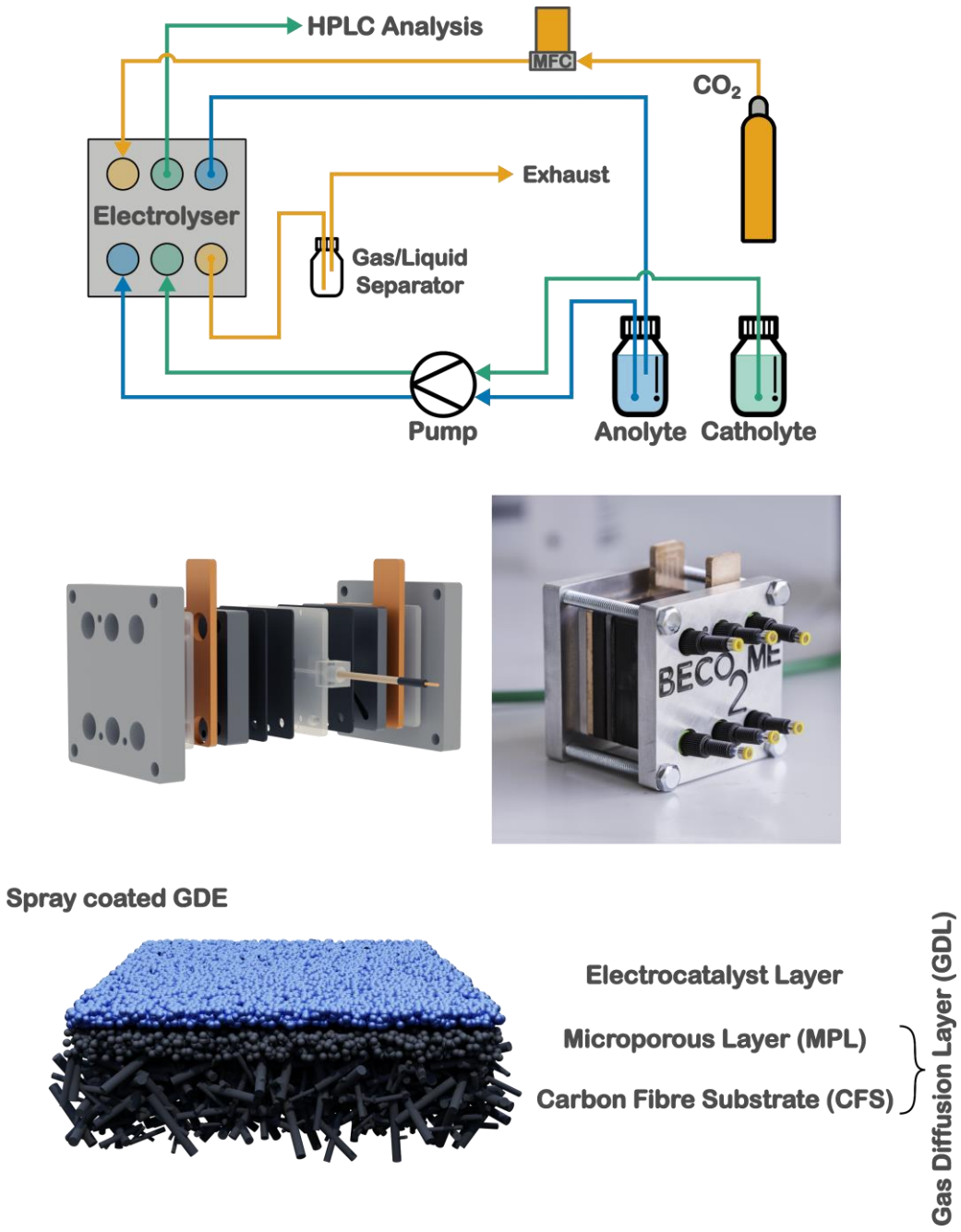

Figure S5.4 eCO_2R electrolyser setup and Gas Diffusion Electrode (GDE) schematic

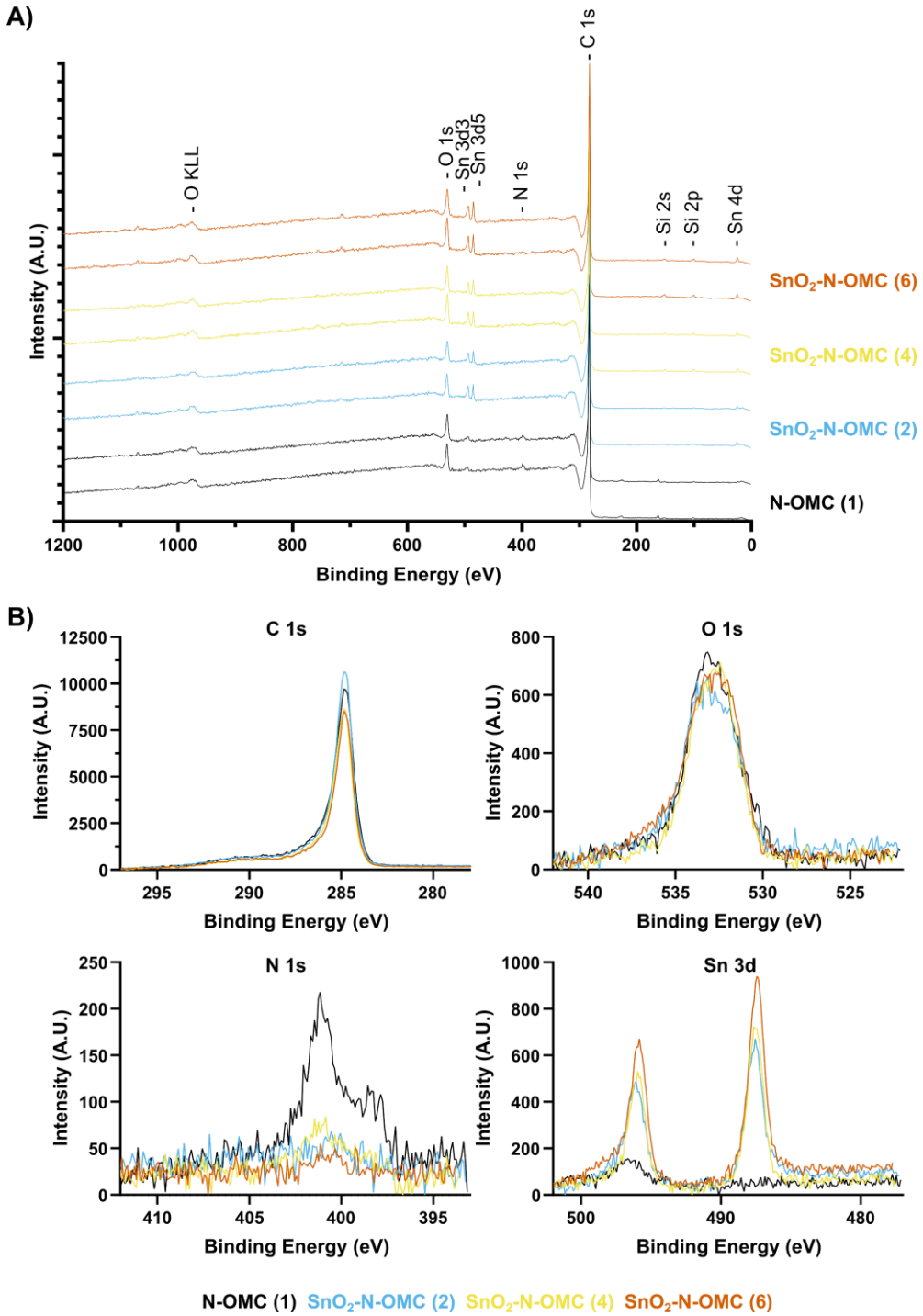

Figure S5.5 XPS spectra N-OMC (1), SnO_2-N-OMC (2), SnO_2-N-OMC (4) and SnO_2-N-OMC (6), with A) duplicate survey of all (Sn-)N-OMC electrocatalysts and B) high resolution spectra of C 1s, O 1s, N 1s and Sn 3d.

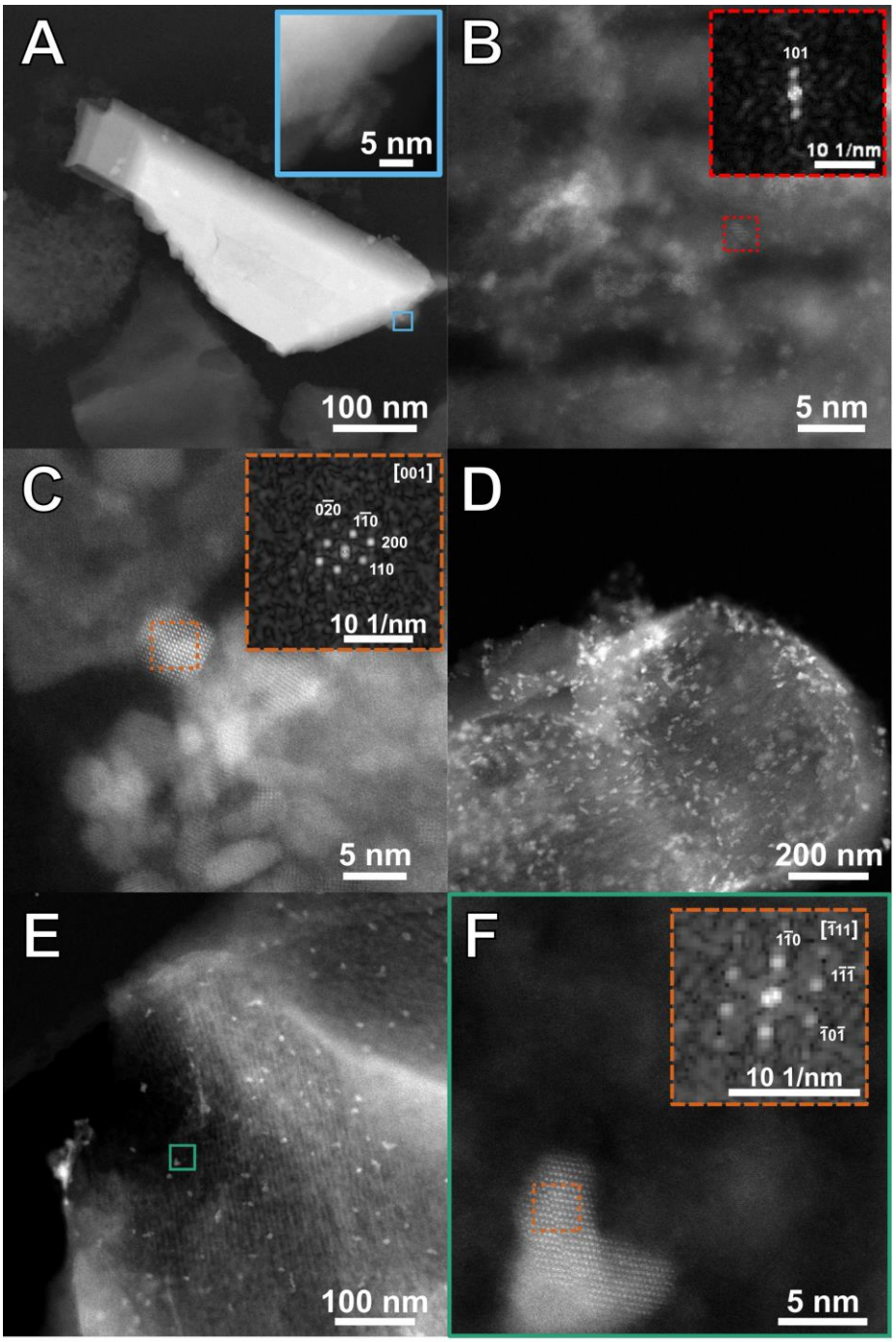

Figure S5.6 HAADF-STEM images and the corresponding Fourier Transform (FT) patterns of A) an irregular large SnO_2 species and B) atomically dispersed species, presumed to be Sn-based and C) SnO_2 nanoparticles in SnO_2-N-OMC (2); D, E and F) SnO_2 nanoparticles in SnO_2-N-OMC (6).

Chapter 6

Pomegranate-structured SnO_2 and SnO_2@C electrocatalysts

Utilising the particle confinement strategy, pomegranate-structured SnO_2 and SnO_2@C electrocatalysts are synthesised in an attempt to acquire a better performing and more stable electrocatalyst than the SnO_2-N-OMC electrocatalysts. The influence of the carbon shell on electrocatalyst stability is investigated and the degradation pathways are elucidated by 24 h CO_2 electrolysis and an in-depth physicochemical characterisation.

This chapter has been published as K. Van Daele *et al.*, "Enhanced Pomegranate-Structured SnO_2 Electrocatalysts for the Electrochemical CO_2 Reduction to Formate," *ChemElectroChem*, vol. 202201024, pp. 1–9, Feb. 2023.
(https://doi.org/10.1002/celc.202201024)

6.1 Introduction

The development and exploration of the SnO_2-N-OMC electrocatalysts, in Chapter 5, has contributed to our understanding of the influence of the N-OMC carbon capture medium supporting material on the eCO_2R towards formate. The enhanced CO_2 adsorption, by virtue of the N-OMC support material, appeared to positively influence the overpotential, when comparing the required overpotential for the as-synthesised SnO_2-N-OMC electrocatalysts with the state-of-the-art in Table 1.1. As a result, all SnO_2-N-OMC electrocatalysts demanded a lower overpotential for the conversion of CO_2 towards FA at the industrially relevant current density of 100 mA cm^{-2}. Furthermore, valuable insights into the selectivity and degradation pathways of SnO_2 species were gained. *Ex situ* HAADF-STEM revealed the morphological degradation of the SnO_2 species, i.e. segregation/pulverisation and agglomeration, and the *in situ* SnO_2 reduction towards metallic Sn which appeared to be the most detrimental for the FE_{FA}. Unfortunately, from an industrial perspective, these SnO_2-N-OMC electrocatalysts and synthesis method are not viable as their selectivity and stability is insufficient, the synthesis method is too convoluted and has a too low yield. Nonetheless, an optimal combination of both SnO_2 species and the N-OMC carbon capture medium could result in a synergistic effect for the eCO_2R towards FA, especially when utilisation of the N-OMC support material and incorporation of the SnO_2 species is optimized to morphologically stabilize the SnO_2 electrocatalytic active species through particle confinement.

Recently, the strategic use of a thin carbon shell which encapsulates the electrocatalytic nanoparticle has been highlighted by Yoo *et al.*[237,238] to enhance the stability during electrocatalysis. Acting as a protective layer, the thin carbon shell is reported to physically inhibit agglomeration and it has also been demonstrated to prevent surface oxidation. In this chapter, pomegranate-structured SnO_2 (Pom. SnO_2) and -SnO_2@Carbon (Pom. SnO_2@C) electrocatalysts were synthesised and tested for the eCO_2R reduction towards formate. Prior to this work, Wen *et al.*[239] used these pomegranate-structured SnO_2 and pomegranate SnO_2@C nanocomposites, combined with Cu particles, as anodes for lithium-ion batteries. However, due to their increased surface area, compared to commercial SnO_2 nanoparticles, and the possibility to synthesise them with and without an encapsulating carbon shell, we deemed them interesting electrocatalysts for the eCO_2R towards formate. With an initial selectivity of 83 and 86% towards formate and an operating potential of -0.72 V and -0.64 V vs. RHE, respectively, the pomegranate SnO_2 and –SnO_2@C electrocatalysts are able to compete with the state-of-the-art. Ultimately, given the importance of electrocatalyst stability, long-term experiments (24 h) were performed and their degradation was fully charted.

6.2 Experimental

6.2.1 Chemicals

The following chemicals and commercial electrocatalyst were used as received, without any further purification: d-glucose (anhydrous,

biotechnology grade, VWR Life Science), D520 NAFION® solution (Ion Power), ethanol (99.8%, abs. p., Chem-Lab), potassium hydrogen carbonate (99.5+%, v.p., Chem-Lab), potassium hydroxide (85+%, pellets a.r., Chem-Lab), 2-propanol (99.8+%, iso-propanol a.r., Chem-Lab), sodium tin(IV) oxide trihydrate (98%, Alfa Aesar), Tin(IV) oxide (nanopowder, ≤ 100 nm avg. part. size, Sigma-Aldrich).

6.2.2 Synthesis of the pomegranate-structured SnO_2 and SnO_2@C electrocatalysts

Pom. SnO_2 and SnO_2@C electrocatalysts were prepared via a method adapted from Wen *et al.*,[239] by dissolving 20 mmol sodium stannate ($Na_2SnO_3.3H_2O$) in 100 mL of a 1 M aqueous glucose solution. After 1 hour of sonication, the solution was transferred into two teflon-lined stainless steel autoclaves and placed in an oven at 180 °C. After 4 hours, the autoclaves were rapidly cooled down to room temperature and the precipitates were collected via centrifugation. Subsequently, the obtained precipitates were washed three times with deionized water and ethanol. After drying overnight at 100 °C, pomegranate-structured SnO_2 and SnO_2@C electrocatalysts were acquired through a final heat treatment at 550 °C (2 °C min^{-1}) for 4 h under air and argon atmosphere, respectively.[239]

6.2.3 Physicochemical characterization

Nitrogen (N_2) physisorption was performed at 77 K with a Quantachrome Quadrasorb SI (Quantachrome Instruments, Boynton Beach, FL, USA) automated surface area & pore size analyzer. Prior to

the measurements, all samples were degassed for 16 h at 200 °C. The specific surface area was calculated using the Brunauer-Emmett-Teller (BET) equation.

X-ray Powder Diffraction (XRD) was measured on a Bruker D8 ECO powder diffractometer with a LYNXEYE XE-T detector and Cu K-Alpha radiation. All samples were probed from 0 – 80° or 20 – 80° 2ϑ and compared with the crystallography open database (COD) #1534785 for tetragonal SnO_2, #4124667 for SnO, #9008570 for Sn and #9012230 for graphite.

Scanning Electron Microscopy (SEM) measurements have been carried out using a ThermoFisher Scientific Quanta FEG 250 equipped with an ETD detector, operated at an acceleration voltage of 10 and 20 kV.

High and Low Angle Annular Dark-Field Scanning Transmission Electron Microscopy (HAADF-STEM and LAADF-STEM) as well as Energy Dispersive X-ray Spectroscopy (EDS) has been performed using an aberration-corrected cubed Thermo Fisher Scientific Titan microscope operating at 300 kV and equipped with a Super X EDS detector. EDS analysis was performed by acquiring at least 200 frames at a higher current of 150 pA to ensure sufficient signal. HAADF-STEM was realized using a collection angle between 46 and 215 mrad, while LAADF-STEM was realized using a collection angle between 19 and 74 mrad, to be able to visualize the carbon shell near the SnO_2@C electrocatalysts.

EDS experiments for Pomegranate SnO_2@C samples were performed using Si_3N_4 grids to be able to correctly map the carbon signal in the sample.

X-ray Photoelectron Spectroscopy (XPS) was performed on a PHI-VersaProbe III, using an Al Kα (1486.6 eV) monochromatic X-ray source. An area of Ø 100 µm was measured, using a pass energy of 26 eV for the high resolution (HR) spectra and an automatic neutraliser. The PHI MultiPak software was used for processing the Sn 3d XPS spectra.

6.2.4 Electrochemically Active Surface Area and uncompensated resistance determination

The electrochemically active surface area (ECSA) was derived from the electrochemical double layer capacitance (C_{dl}) of the catalytic surface, measured on pristine electrocatalyst coated gas diffusion electrodes, prior to the electrochemical CO_2 reduction. Multiple cyclic voltammetry experiments were performed, in a non-faradaic region, at scan rates of 80, 120, 160, 200, 240, 280 and 320 mV s^{-1}. A linear regression was plotted between the capacitive current density differences in the middle of the potential window and the scan rate.

The uncompensated resistance R_u (Ohmic drop), was determined prior to all electrochemical CO_2 reduction experiments, by means of a current interrupt measurement. To his extent, a constant potential of -4 V vs. Ag/AgCl was applied before triggering the current interrupt circuit and measuring the potential decay over a time period of 2 ms. The uncompensated resistance is then obtained from a linear regression

between 0 s and 500 µs in the Metrohm Autolab Nova 2.1.5 Software for electrochemical research. All potentials were corrected for this resistance.

6.2.5 Electrochemical CO_2 reduction

Commercial SnO_2 nanoparticles and the as-synthesised pomegranate-structured SnO_2 and SnO_2@C electrodes were prepared by spray coating (Chapter 5) a Sigracet 39 BB gas diffusion electrode (GDE) with an ink made from the obtained electrocatalyst powders. For each deposition, 75 mg of the electrocatalyst powder is dispersed with 0.3750 g of a 5 wt% Nafion solution in approximately 10 mL of a 1:1 Milli-Q (18.2 MΩ·cm @ 25 °C):IPA Solution. A GDE of 25 cm^2 is slowly and uniformly spray coated before being divided into 6 smaller GDEs with a projected area of approximately 3 cm^2 and the targeted electrocatalyst loading of 1.5 mg cm^{-2}. These spray coated GDEs were then used as cathodes in a small-flow by electrolyser with a geometric electrochemically active surface area of 1 cm^2.

Chronopotentiometric experiments of 1 hour were conducted in the abovementioned flow-by electrolyser at an applied current density of -100 mA cm^{-2}. The catholyte, 0.5 M $KHCO_3$, was pumped single pass at a flow rate of 2 mL min^{-1}, while the anolyte, 2 M KOH, was recycled at an equal flow rate over a Ni foam anode. Furthermore, a Nafion 117 membrane and Ag/AgCl reference electrode were used. Liquid samples were taken after 15 minutes and after 1 hour to determine the FE% towards formate by means of HPLC. Long-term 24 h chronopotentiometric experiments were

conducted under identical circumstances, where the FE% towards formate was determined after 15 minutes and every hour for the first 6 hours and once again after 24 h. The reported data was reproduced and an average value is reported for all FE% and iR-compensated potentials.

6.3 Results and discussion

6.3.1 Physicochemical characterization

The particle morphology and size distribution of the commercial SnO_2 nanoparticles, pomegranate-structured SnO_2 and SnO_2@C electrocatalysts, prior to the electrochemical CO_2 reduction, were investigated by means of Scanning Electron Microscopy (SEM). As shown in figure 6.1, the commercially available tin(IV) oxide nanopowder has a broad size distribution (≤ 100 nm avg. part. size) and consists of smooth surfaced nanoparticles with varying morphology.

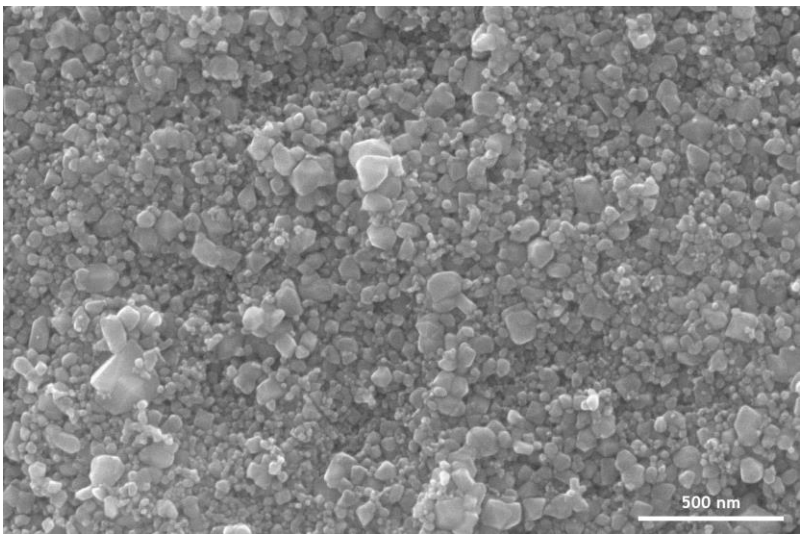

Figure 6.1 Scanning Electron Microscope (SEM) image commercial Tin(IV) oxide nanopowder.

Meanwhile, as shown in figure 6.2, the synthesised pomegranate-structured SnO_2 electrocatalysts are spherical particles with a rough morphology (composed of smaller nanoparticles) and a particle size of approximately 80 nm or smaller.

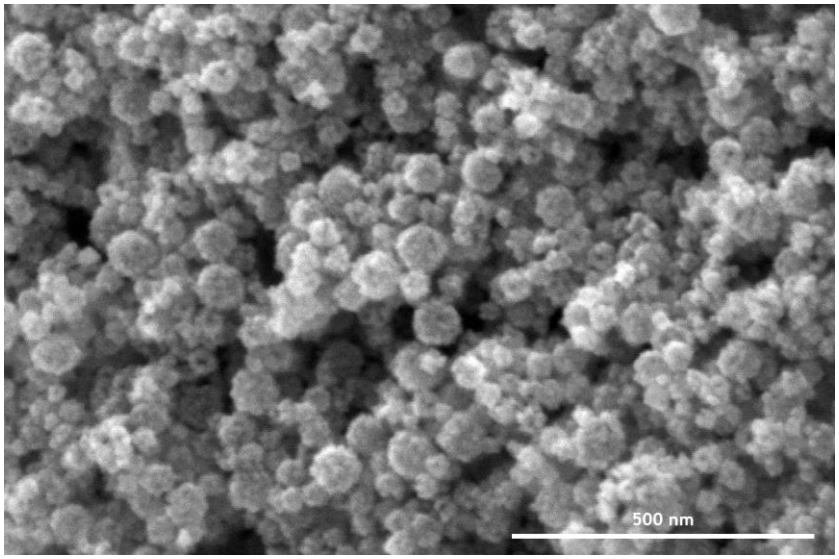

Figure 6.2 SEM image pomegranate-structured SnO_2 electrocatalysts.

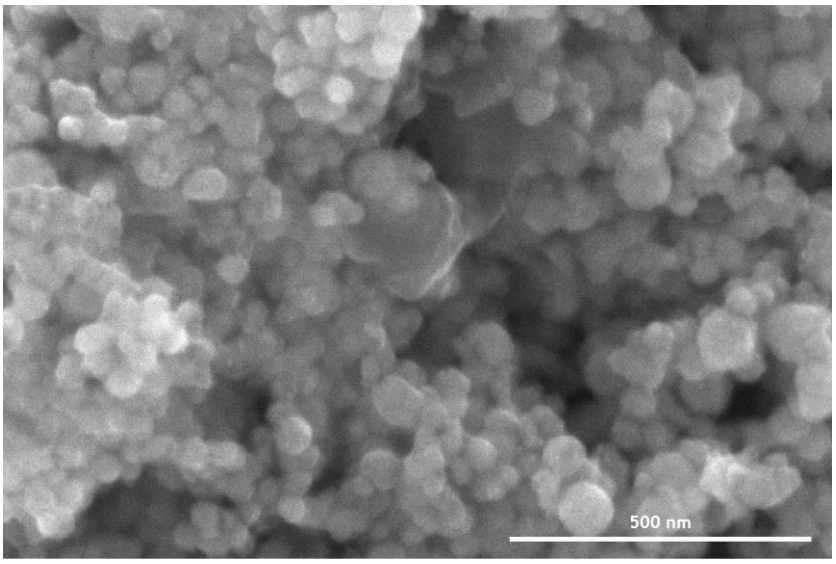

Figure 6.3 SEM image pomegranate-structured SnO_2@C electrocatalysts.

Simultaneously, the pomegranate SnO_2@C (Figure 6.3) nanocomposites appear to be smooth spheres due to the surrounding carbon shell. Furthermore, the particle size distribution of the pomegranate SnO_2@C nanoparticles is similar to the pomegranate SnO_2 electrocatalyst, which is as expected, since both originate from the same batch.

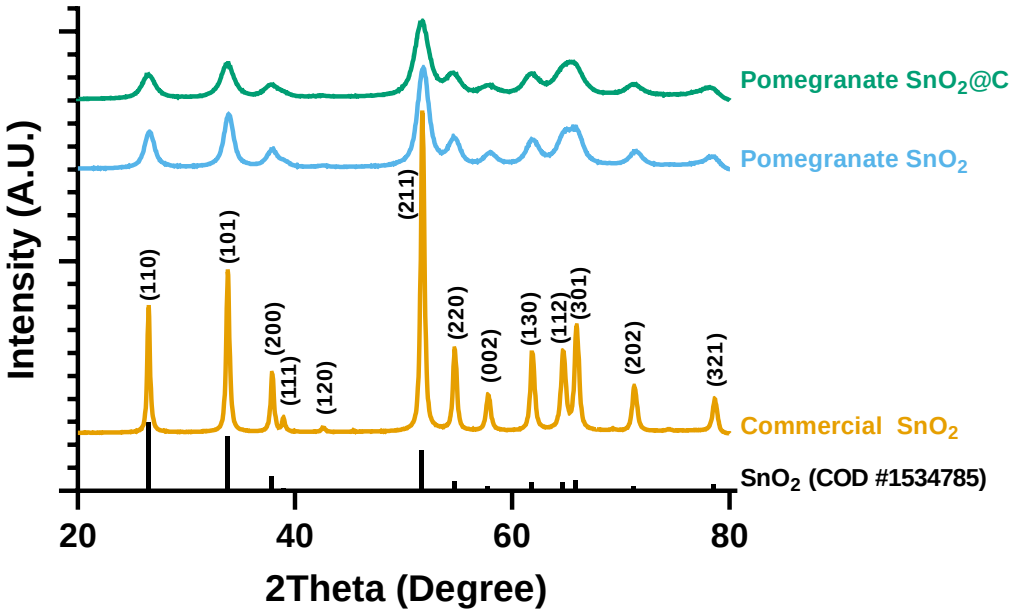

Figure 6.4 XRD diffractogram of the commercial SnO_2 nanoparticles, pomegranate SnO_2 and pomegranate SnO_2@C electrocatalysts, compared with the Crystallography Open Database (COD) #1534785 for tetragonal SnO_2.[234,235]

Additional information concerning the crystalline structure, chemical nature, and space group symmetry of the commercial SnO_2, pomegranate SnO_2, and pomegranate SnO_2@C electrocatalysts was obtained by XRD. The diffractogram (Figure 6.4) displays the typical diffraction pattern with peaks at 2ϑ = 26.5°, 33.8°, 37.9°, 38.9°, 42.6°, 51.7°, 54.7°, 57.7°, 61.8°, 64.6°, 65.8°, 71.1° and 78.5°, present in the commercial SnO_2 nanoparticles

and nearly all present in the pomegranate SnO_2 and pomegranate SnO_2@C electrocatalysts. These peaks are attributed to reflections of the (110), (101), (200), (111), (120), (211), (220), (002), (130), (112), (301), (202) and (321) planes, respectively, of tetragonal SnO_2 (COD #1534785).[234,235] Furthermore, the peak broadening (area) and Scherrer equation enabled us to calculate the particle size of the smaller nanoparticles that make up the larger pomegranate structure. With an average particle size of 7.1 ± 0.9 nm and 6.4 ± 1.3 nm for the Pom. SnO_2 and Pom. SnO_2@C electrocatalyst, respectively, these results are similar to the obtained particle size distribution from HAADF-STEM imaging.

As mentioned in section 4.1.4, currently, no definitive consensus has been reached concerning the active site and selective species for the eCO_2R towards formate on Sn-based electrocatalysts.[152,177–179] Nevertheless, the importance of Sn oxide species, present in our pomegranate-structured electrocatalysts, has been highlighted for the selective eCO_2R towards formate.[80,116,139,183,184,186,187] For example, DFT calculations by An *et al.*[122] found that a suitable ratio of $Sn^0/Sn^{2+}/Sn^{4+}$ results in a synergistic effect. The presence of tetravalent (Sn^{4+}) and divalent (Sn^{2+}) tin were shown to reduce the overpotential and improve formate selectivity, respectively, while the presence of Sn oxides/metal Sn interfaces aids in suppressing the competing HER.[122] While starting from a SnO_2/Sn heterostructure might energetically favour formate production and suppress the HER, SnO_2 electrocatalysts have been demonstrated to be of a dynamic nature, enabling partial *in situ* reduction towards this presumably preferred

SnO_2/Sn Mott–Schottky heterojunction species, which makes for a more straightforward synthesis and warrants our choice of SnO_2 as a starting point.[180]

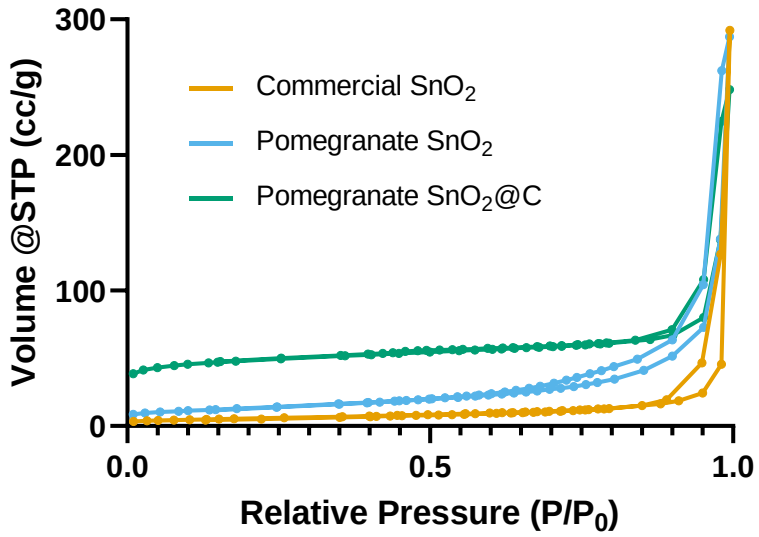

Figure 6.5 Nitrogen physisorption isotherms of the commercial SnO_2 nanoparticles, pomegranate SnO_2 and pomegranate SnO_2@C electrocatalysts.

Insight into the possible electrochemically active surface area was achieved by performing nitrogen (N_2) physisorption and using the Brunauer-Emmett-Teller (BET) equation to calculate the specific surface area. The nitrogen adsorption-desorption isotherms of all samples (Figure 6.5) display a type II isotherm with abundant interparticle porosity, according to the IUPAC classification of physisorption isotherms.[231] With a BET surface area of ≈20 m^2 g^{-1}, the commercial SnO_2 nanoparticles have, ostensibly, the lowest amount of available active sites for the eCO_2R. The previously reported surface roughness of the pomegranate SnO_2 nanoparticles and the heterogeneous carbon shell of the pomegranate SnO_2@C electrocatalyst offer a larger surface area of ≈47 m^2 g^{-1} and ≈180

m^2 g^{-1}, respectively, which in theory should provide more active sites for the electrochemical conversion of CO_2. The BET surface area plots are provided in the supporting information (S6.1 – 6.3).

Next, an indication concerning the electrochemically active surface area (ECSA) is derived from the electrochemical double layer capacitance (C_{dl}) of the catalytic surface (Figure S6.4). The higher C_{dl} of the Pom. SnO_2 (6.84 mF) electrocatalyst than that of the commercial SnO_2 nanoparticles (3.48 mF) indicates a larger ECSA for the Pom. SnO_2, compared to the commercial SnO_2 nanoparticles. Contrary to what was expected based on the BET surface areas, Pom. SnO_2@C yielded the lowest C_{dl} of 2.22 mF. Nevertheless, upon converting the C_{dl} to ECSA (i.e. by dividing the C_{dl} by the specific capacitance), a higher ECSA is expected for Pom. SnO_2@C as compared to the Pom SnO_2 and commercial SnO_2 electrocatalysts, when looking at the specific capacitance for SnO_2 (40 – 60 µF $cm^{-2}_{catalyst}$) and carbon (approx. 10 µF $cm^{-2}_{catalyst}$) and considering the higher contribution of this carbon than the pomegranate structured SnO_2 to the ECSA measurement of the Pom. SnO_2@C electrocatalyst.[165]

6.3.2 Electrochemical CO_2 reduction

Electrocatalytic selectivity for the eCO_2R towards formate was first investigated in a small (1 cm^2) flow-by electrolyser (Figure S5.4) by performing a 1 h chronopotentiometric experiment at a constant current density of 100 mA cm^{-2}. Figure 6.6 shows the operating potentials (V vs. RHE) and FE% towards formate plotted as a function of time for the commercial SnO_2 nanoparticle (SnO_2), pomegranate SnO_2 (Pom. SnO_2),

and pomegranate SnO_2@C (Pom. SnO_2@C) electrocatalysts. With an average potential of -0.55 V vs. RHE, the commercial SnO_2 nanoparticles display an average selectivity (FE%) towards formate of 79%. A slightly more negative potential of -0.72 V vs. RHE could be observed for the pomegranate SnO_2, which exhibit an excellent FE% of 83%. Finally, the pomegranate SnO_2@C nanocomposites display the highest selectivity for the eCO_2R towards formate, i.e. 86%, and an operating potential between the other two samples, i.e. -0.64 V vs. RHE. In terms of selectivity and activity, both the commercial SnO_2 nanoparticle electrocatalyst and Pom. SnO_2 and -SnO_2@C nanocomposite electrocatalysts belong amongst the best Sn-based materials reported thus far for the eCO_2R towards FA (Table 1.1, Chapter 1).[50,66,189]

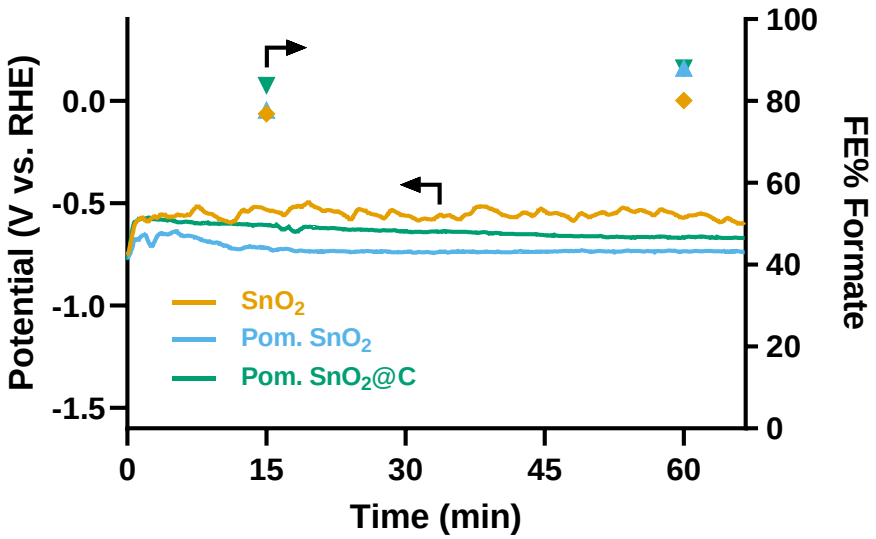

Figure 6.6 Average iR-compensated potential (V vs. RHE) and FE% towards formate plotted as function of time (min) at a constant current density of 100 mA cm^{-2} for 1 h.

However, for the eCO_2R towards formic acid to become industrially relevant, prolonged electrocatalytic stability should be attained.[44,65] Initial

insights concerning the stability of the commercial SnO_2, Pom. SnO_2 and Pom. SnO_2@C electrocatalysts were obtained by performing 24 h chronopotentiometric measurements (100 mA cm^{-2}), combined with post-electrolysis *ex situ* transmission electron microscopy (TEM). Figure 6.7 displays the average iR-compensated operating potential and FE% towards formate plotted as function of time. Here, it is noticed that while the operating potential remains relatively stable at -0.49 V and -0.62 V vs. RHE for the commercial SnO_2 and pomegranate SnO_2 electrocatalysts, respectively, the operating potential of the pomegranate SnO_2@C electrocatalyst continues to become more negative, decreasing from -0.64 V to -0.88 V vs. RHE, over the course of the 24 h experiment. Previously, in chapter 5, a similar trend of a continuously decreasing cathodic potential was observed for the N-OMC carbon capture medium.

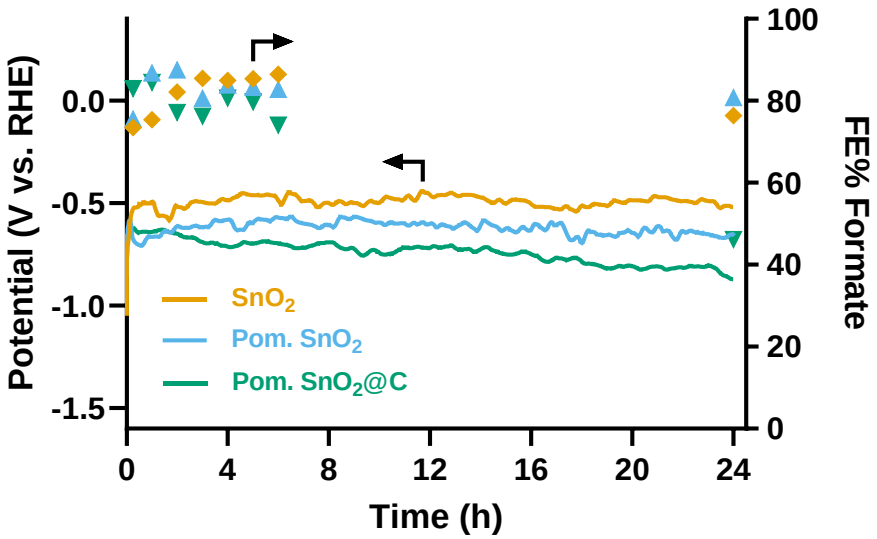

Figure 6.7 Average iR-compensated potential (V vs. RHEl) and FE% towards formate plotted as function of time (h) at a constant current density of 100 mA cm^{-2} for 24 h.

Interestingly, the FE% towards formate of both the commercial SnO_2 and pomegranate SnO_2 are relatively stable at an average of 81% and 83%, respectively, while the FE% of the pomegranate SnO_2@C nanocomposites experiences a decrease from an average 83% (after 15 minutes) to 46% (after 24 hours). These results appear to counter the hypothesis that the carbon shell would increase the electrocatalytic stability, by acting as a protective layer, physically inhibiting particle agglomeration.

After these long-term experiments, the used GDEs were left to dry under air (without washing) and the electrochemical performance of the used electrocatalysts was evaluated again. Figure 6.8 shows the comparison in average FE% towards formate, for a 1 hour electrolysis at 100 mA cm^{-2}, between a newly spray coated and used GDE.

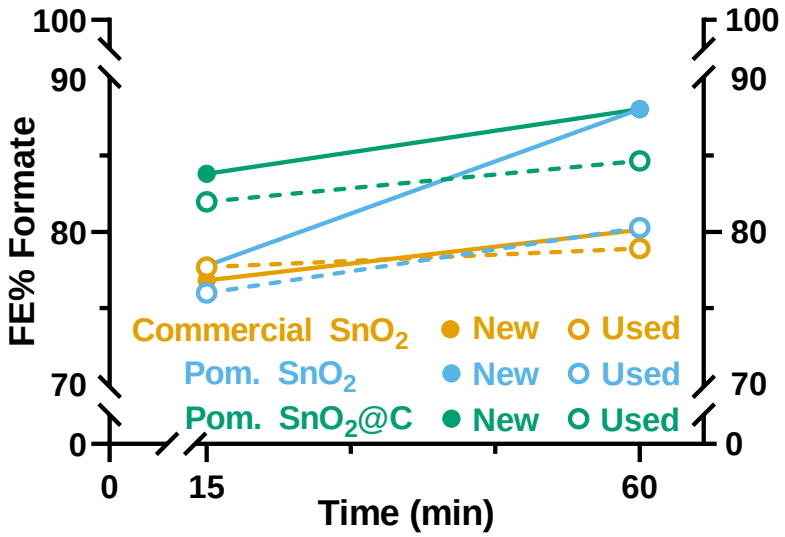

Figure 6.8 Faradaic efficiency towards formate, over a 1 h electrolysis at 100 mA cm^{-2}, of a new and used GDE, spray coated with the commercial SnO_2, Pomegranate SnO_2 (Pom. SnO_2) or Pomegranate SnO_2@C (Pom. SnO_2@C) electrocatalyst.

For all samples the selectivity of the GDE that had previously been used for 24 h is slightly lower, yet comparable to the initial (new) FE%. The loss of selectivity for the Pom. SnO_2@C electrocatalyst could thus, for the most part, be restored to its original FE% by leaving the electrode to dry under air. Out of all the used (24 h) electrocatalysts, the pomegranate SnO_2@C electrocatalyst had the highest selectivity over a time period of one hour, reaching an average recovered FE% of 85%, while the commercial SnO_2 and pomegranate SnO_2 electrocatalysts reached an average of 79 and 80% FE% towards formate, respectively.

To elucidate the loss and recovery of the selectivity of the Pom. SnO_2@C electrocatalyst, *ex situ* HAADF-STEM imaging and EDS elemental mapping were used to investigate the pomegranate SnO_2 (Figure 6.9) and pomegranate SnO_2@C (Figure 6.10) electrocatalysts, before and after 24 h electrolysis.

For the Pom. SnO_2 electrocatalyst, low-magnification HAADF-STEM images, acquired before (Figure 6.9a) and after (Figure 6.9d) electrolysis, show a clear agglomeration of nanoparticles as well as a loss of the characteristic pomegranate shape after 24 h of electrolysis. Additional HAADF-STEM images, demonstrating this degradation, are provided in the supporting information at the end of this chapter. At higher magnification, HAADF-STEM and FFT (Figure 6.9b) show that the pomegranate SnO_2 nanostructures, prior to electrolysis, are composed of smaller, randomly oriented, crystalline SnO_2 nanoparticles, as previously indicated by the XRD diffractogram. Furthermore, EDS elemental

mapping confirms the presence of Sn and O on both Pom. SnO_2 samples, prior to (Figure 6.9c) and after (Figure 6.9f) 24 h eCO_2R and drying in air. Even though the FE% towards formate remains relatively stable, clear nanoparticle segregation/pulverization and agglomeration could be observed in figure 6.9e in comparison to Fig. 6.9a. These phenomena have previously been reported in chapter 5 for the SnO_2-N-OMC electrocatalysts and by He *et al.* and Wu *et al.*,[73,120] where this change in the particles' physicochemical properties always resulted in a loss of FE%.

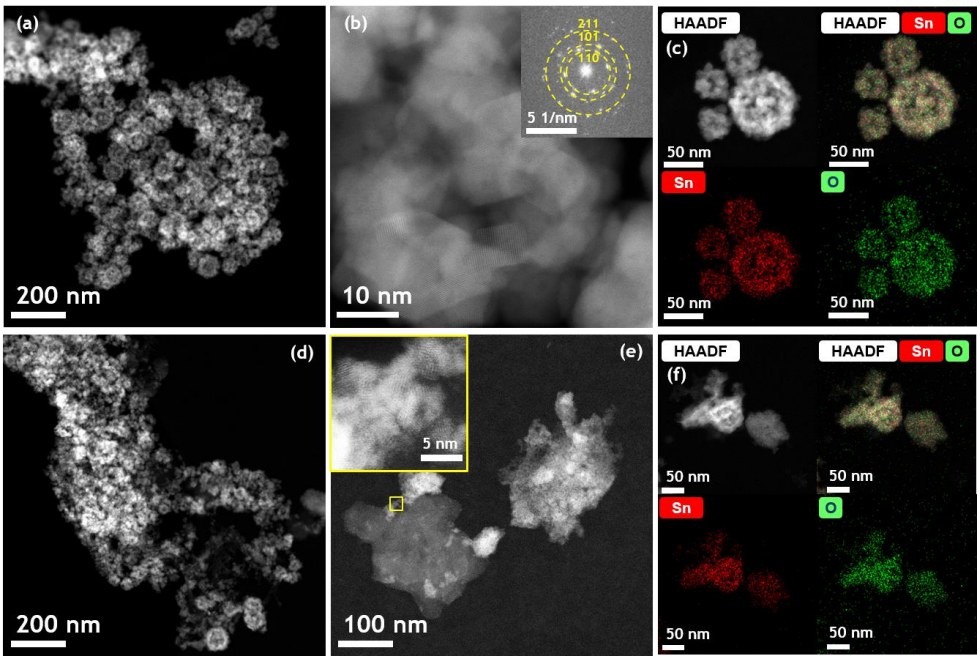

Figure 6.9 HAADF-STEM image of Pomegranate SnO_2 nanoparticles before (a) and after (d) electrochemical CO_2 reduction. High-resolution HAADF-STEM image from which it can be verified that the pomegranate nanostructures are formed by SnO_2 nanoparticles, which is further confirmed by the crystalline structure observed in the FFT (b). HAADF-STEM image of the segregation and agglomeration of small SnO_2 nanoparticles after current application (e), and HAADF-STEM images and EDS maps of the nanoparticles before (c) and after (f) the electrochemical experiment. EDS confirms the presence of Sn and O on both samples.

Here, no significant loss of selectivity was observed after 24 h. Nonetheless, the effects of this irreversible morphological degradation may start to appear in the FE% in the long run (>24 h). Therefore, further investigation is necessary to unravel the effect of these morphological changes on the long-term stability and selectivity of the pomegranate SnO_2 electrocatalyst. Accelerated degradation tests combined with *ex situ* characterisation are a promising method for efficient and rapid investigation.[189]

In the case of the Pom. SnO_2@C electrocatalyst, low magnification HAADF-STEM images and EDS maps before (Figure 6.10a) and after (Figure 6.10d) electrolysis show similar pomegranate structures, indicating that the heterogeneous layer of carbon covering the particles seems to successfully prevent particle agglomeration/segregation. Supplementary HAADF-STEM images from before and after 24 h of eCO_2R are provided in the supporting information at the end of this chapter. A careful selection of the acquisition semi-angle in dark field mode of the electron microscope was necessary for the correct visualization of the carbon layer because the high contrast from the SnO_2 nanoparticles masks the carbon signal at high convergence semi-angles. Therefore, Low Angle Annular Dark-Field Scanning Transmission Electron Microscopy (LAADF-STEM) mode was used to reveal the carbon coverage (in light grey, as indicated by the yellow arrows) over the pomegranate SnO_2 particles before (Figure 6.10b, c) and after (Figure 6.10e, f) 24 h electrolysis, showing that it's quite heterogeneous and no complete carbon coverage was obtained. These

results show that although a loss in porosity could not be entirely prevented, the heterogeneous carbon shell was able to moderately suppress particle agglomeration. Since even a partially covering heterogeneous carbon shell is able to, to a certain extent, protect the pomegranate SnO_2 nanoparticles from irreversible morphological changes, further improvements to the electrocatalysts stability could be achieved by perfecting the synthesis procedure and achieving a fully covering, homogenous carbon shell. The temporary loss in selectivity over the course of a 24 h electrolysis, therefore, appears to be caused by a degradation pathway other than segregation and/or agglomeration.

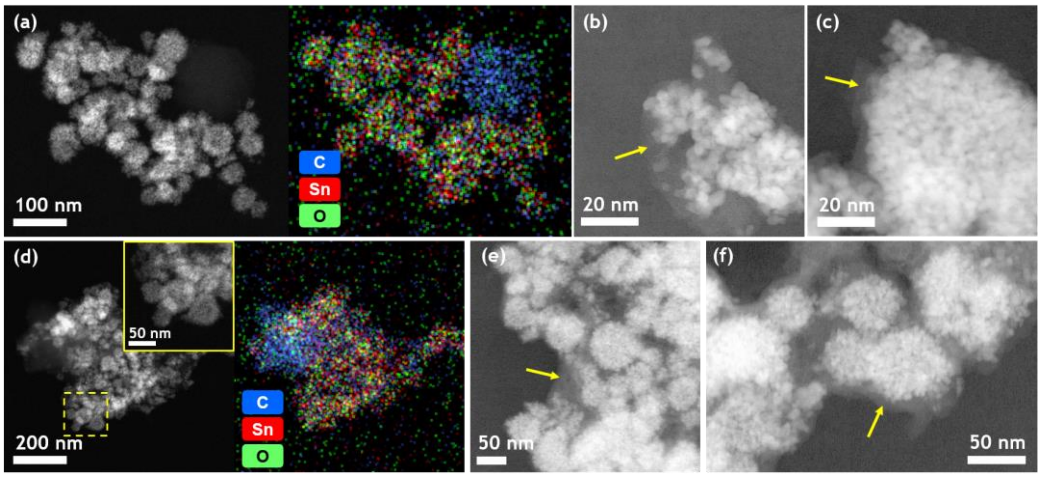

Figure 6.10 HAADF-STEM image and EDS map of the Pomegranate SnO_2@C particles before (a) and after (d) electrochemical CO_2 reduction where similar particle morphology is observed (inset of magnified area marked in yellow), indicating that the carbon shell helps to better retain the original morphology. EDS maps show a heterogeneous distribution of carbon over both samples. LAADF-STEM images of the sample before (b, c) and after (e, d) current application show the heterogeneous carbon coverage in light grey, as indicated by the yellow arrows, over the pomegranate SnO_2 particles.

Given these results, particle segregation/pulverisation and agglomeration are highly unlikely to be the cause of the observed temporary decrease in FE% for the Pom. SnO_2@C electrocatalyst. Other possible explanations could be the loss of GDE hydrophobicity, resulting in flooding and salt crystallization, *in situ* SnO_2 reduction, or poisoning of the electrocatalyst.[189,195,202,240] While a small amount of perspiration, through the GDE, was noticed during all 24 h measurements, we found that this could not be the sole explanation for the temporary decrease of selectivity of the pomegranate SnO_2@C electrocatalyst. Furthermore, no excessive salt crystallization was observed and the electrocatalysts were able to largely recover their initial selectivity by drying under air without any washing. Since electrocatalyst poisoning generally originates from reaction intermediates or impurities from the electrolyte, electrolyser components, or CO_2 feed,[194] we deemed it highly unlikely for this to exclusively occur with the Pom. SnO_2@C electrocatalyst. Nonetheless, the covering, heterogeneous carbon shell may change the local environment of the electrocatalyst compared to the commercial SnO_2 and Pom. SnO_2 electrocatalyst, which could result in the possible trapping of reaction intermediates or other changes in the carbon shell of the Pom. SnO_2@C.[241] Given that the loss of selectivity was largely recovered by leaving the used Pom. SnO_2@C GDE to dry under air, *in situ* reduction of SnO_2 to metallic Sn^0 under the harsh cathodic operating conditions and subsequent re-oxidation in air appears to be the main cause of the temporary loss of selectivity, similar to the SnO_2-N-OMC electrocatalysts in chapter 5.[177]

To confirm our hypothesis, additional *ex situ* physicochemical characterization for both electrocatalysts was performed on both pristine spray coated GDEs and used electrodes. Firstly, *ex situ* XRD (Figure 6.11), after 24 h of electrolysis, clearly indicates a change in the oxidation state of the pomegranate SnO_2 nanocomposites when comparing the Pom. SnO_2 and Pom. SnO_2@C diffractogram from before and after the eCO_2R, respectively.

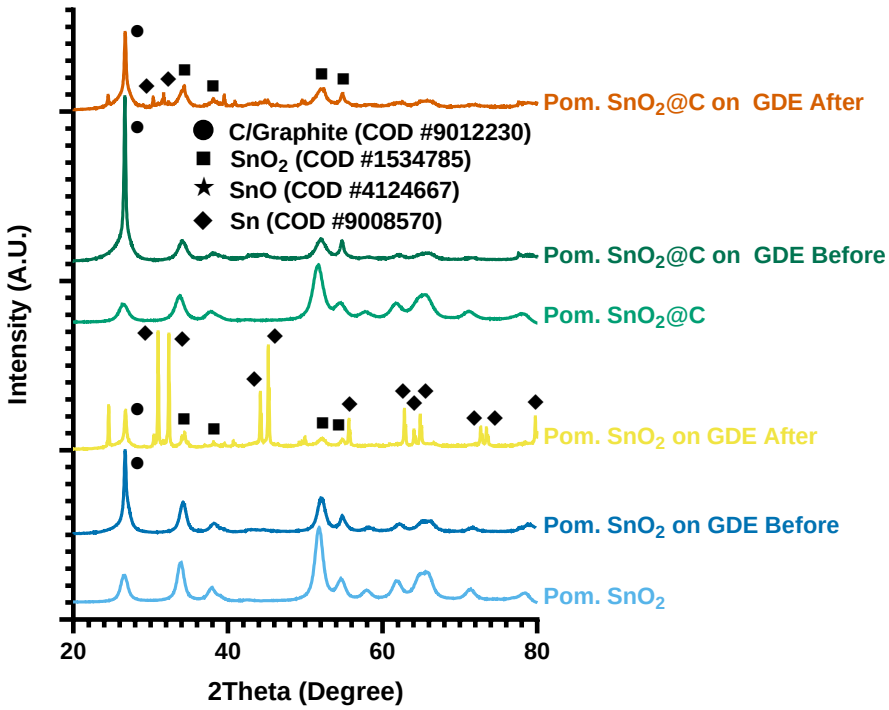

Figure 6.11 Ex situ XRD diffractogram of Pom. SnO_2 and Pom. SnO_2@C before and after 24 h of eCO_2R, compared with the Crystallography Open Database (COD) #9012230 for graphite, #1534785 for SnO_2, #4124667 for SnO and #9008570 for Sn.[234,235,242–244]

It appears that upon electrolysis a reduction of the pristine SnO_2 structure indeed occurs, as is evidenced by the appearance of peaks that can be

ascribed to metallic Sn (COD #9008570).[244] Due to the large surface area (S_{BET}) and strong carbon signal, originating from the GDE and Pom. SnO_2@C itself, a quantitative analysis isn't possible and it thus remains unclear which sample underwent the most significant *in situ* reduction.

Therefore, *ex situ* X-ray photoelectron spectroscopy (XPS) and a sputter depth profile were recorded on both electrodes after 24 h of electrolysis, until a stable Sn signal was obtained. Re-oxidation of both samples after electrolysis was minimized by storing and transferring all samples under an inert argon atmosphere. Figure 6.12 shows the high resolution Sn 3d XPS spectrum for both samples after 24 h of electrolysis.

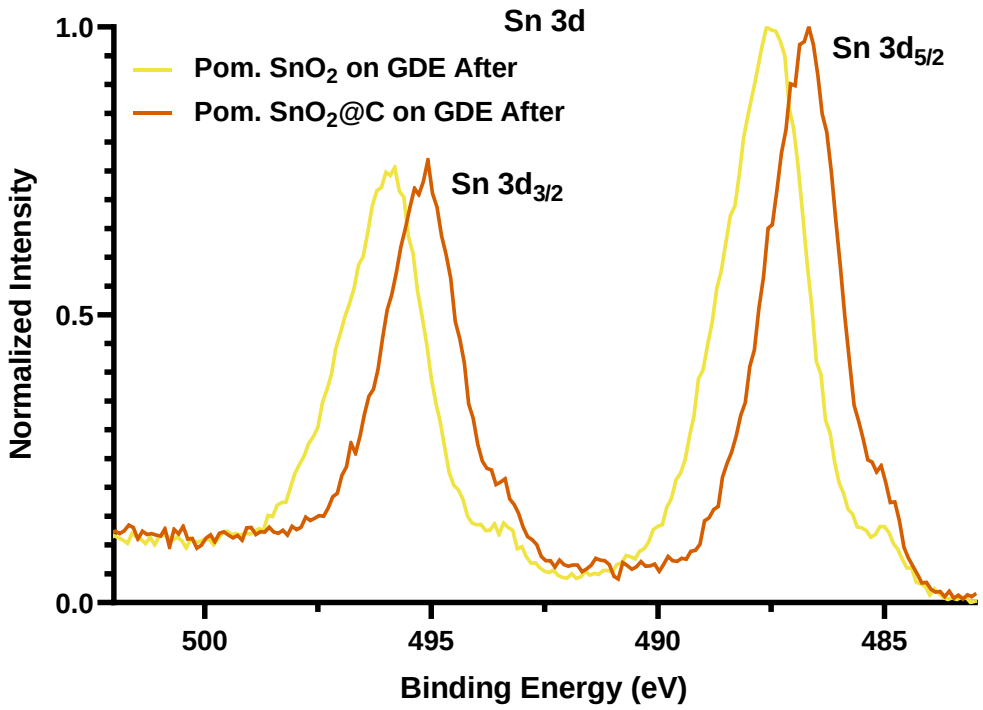

Figure 6.12 Ex situ high resolution Sn 3d XPS spectra of Pom. SnO_2 and Pom. SnO_2@C after 24 h of eCO_2R.[245]

Both Pom. SnO_2 and Pom. SnO_2@C show a large $3d_{5/2}$ peak with an asymmetry at lower binding energies (revealed as a small shoulder) indicating the presence of metallic Sn^0. The difference in binding energy (Δ) between the apex of both shoulders of the Sn $3d_{5/2}$ and $3d_{3/2}$ peaks is approximately 8.41 eV, which corresponds to the reported value in literature for Sn^0, confirming that these shoulders can rightfully be attributed to metallic Sn.[245] The final obtained high resolution Sn 3d XPS spectra were normalized and shifted to match the metallic Sn binding energy (485 ± 0.5 eV).[245]

Comparing the higher binding energy contribution, a clear shift can be noticed which is presumably caused by different types of Sn bonds. Furthermore, the difference in binding energy between the apex of the large Sn $3d_{5/2}$ peak and shoulder is dissimilar for both spectra, indicating the presence of different predominant oxidation states of Sn in both samples. More importantly, these results confirm that, after 24 h of eCO_2R, the Pom. SnO_2@C electrocatalyst encompasses more reduced Sn^0, compared to the Pom. SnO_2 without carbon shell, as evidenced by the increased intensity of the metallic Sn shoulder at a binding energy of 485 eV. This clearly indicates faster and more pronounced *in situ* SnO_2 reduction of the former, which isn't offset by the morphological electrocatalyst degradation revealing new and selective SnO_x active sites, as suspected for the Pom. SnO_2. Consequently, utilising *ex situ* XRD and XPS, we were able to unambiguously link the temporary selectivity loss of the Pom. SnO_2@C electrocatalyst to the *in situ* SnO_2 reduction to Sn^0.

As described by Dutta *et al.*[183,184] the *in situ* reduction of SnO_2 is one of the few degradation pathways which seems to be partially reversible. While *in situ* SnO_2 reduction occurs in all samples, since their operating potentials are comparable, the segregation and agglomeration observed in the Pom. SnO_2 sample could offset and postpone the decrease in selectivity by providing new and selective Sn^{4+} or Sn^{2+} active sites, originating from the core of the original nanoparticles, as previously suggested for the SnO_2-N-OMC electrocatalysts in chapter 5. Although the heterogeneously covering carbon shell largely ensures the preservation of the pomegranate-structured morphology, it also provides a higher conductivity and currently isn't fully covering the pomegranate-structured SnO_2 nanoparticles. Therefore, it probably causes a more rapid depletion of the selective Sn^{4+} or Sn^{2+} sites, ensuring a more rapid loss in selectivity, in comparison to the commercial SnO_2 and Pom. SnO_2 electrocatalysts. Improved synthesis of the Pom. SnO_2@C electrocatalyst, ensuring a homogeneous and fully covering carbon shell has the potential to further increase its long-term electrocatalytic stability by inhibiting irreversible morphological changes and protecting the pomegranate SnO_2 nanocomposites against *in situ* reduction.

6.4 Conclusion

In conclusion, we have successfully synthesised previously reported Pom. SnO_2 and -SnO_2@C nanocomposite electrocatalysts and demonstrated their use as a promising catalyst for the selective eCO_2R to formate. With

an initial selectivity of 83 and 86% towards formate, for the Pom. SnO_2 and Pom. SnO_2@C, respectively, these novel catalysts are able to compete with most current state-of-the-art Sn-based electrocatalysts in terms of activity and selectivity. Furthermore, the pomegranate SnO_2 electrocatalyst exhibits an excellent 24 h stability, maintaining an average FE% formate of 83%. Counterintuitively, the Pom. SnO_2@C electrocatalyst, which retained its morphology much better, as confirmed by HAADF-STEM imaging, displayed a decrease in FE% towards formate from 83% (after 15 minutes) to 46% (after 24 hours). This loss of selectivity, however, proved to be temporary since we were able to restore most of its selectivity to its original FE% by leaving the electrode to dry in air. Out of all the used (24 h) electrocatalysts, the pomegranate SnO_2@C had the highest selectivity over a time period of one hour, reaching an average recovered FE% of 85%, while the commercial SnO_2 and pomegranate SnO_2 electrocatalysts reached an average of 79 and 80% FE% towards formate, respectively. *Ex situ* XRD and XPS were used to link this temporary selectivity loss of the Pom. SnO_2@C electrocatalyst to the *in situ* SnO_2 reduction to metallic Sn. While this electrochemical degradation occurs in both electrocatalysts, it is more pronounced in the Pom. SnO_2@C electrocatalyst since it isn't offset by the morphological electrocatalyst degradation revealing new and selective SnO_x active sites, as suspected for the Pom. SnO_2. The use of a carbon shell has been clearly demonstrated to reduce the irreversible morphological electrocatalytic degradation and we were able to largely restore the temporary selectivity

loss for the Pom. SnO_2@C electrocatalyst by leaving them to dry in air, i.e. re-oxidising them.

Given these results in terms of selectivity, activity and morphological stability, and due to the straightforward synthesis method which displays possibilities towards scaling up, the Pom SnO_2@C electrocatalyst appears to be promising if its morphological stability is maintained for an extended period of operation beyond 24 h and if the *in situ* SnO_2 reduction is mitigated. In the following chapter, pulsed-eCO_2R is explored to investigate whether it is possible to re-oxidise the Pom. SnO_2@C electrocatalyst *in situ*, without having to disassemble the electrolyser.

6.5 Supporting information

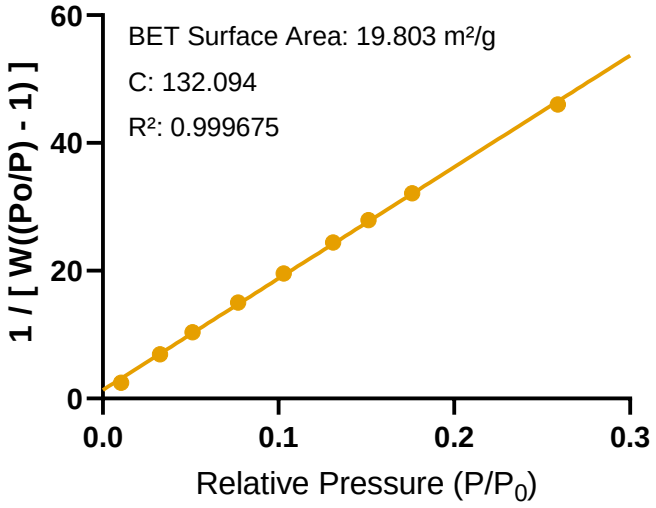

Figure S6.1 Brunauer-Emmett-Teller (BET) surface area plot of the commercial SnO_2 nanoparticles.

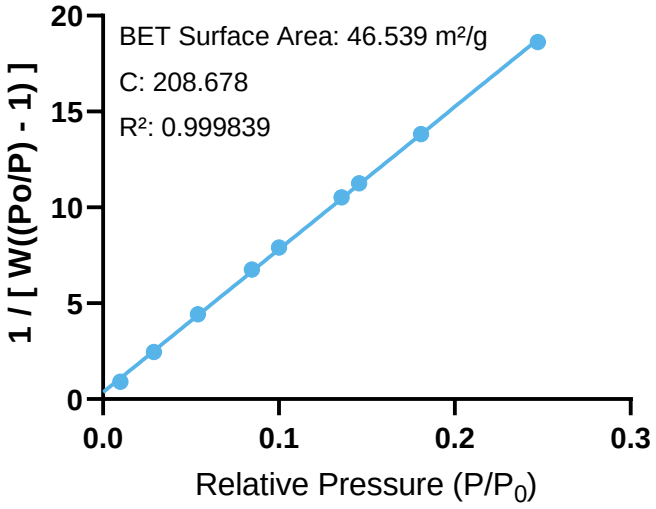

Figure S6.2 Brunauer-Emmett-Teller (BET) surface area plot of the pomegranate SnO_2 electrocatalyst.

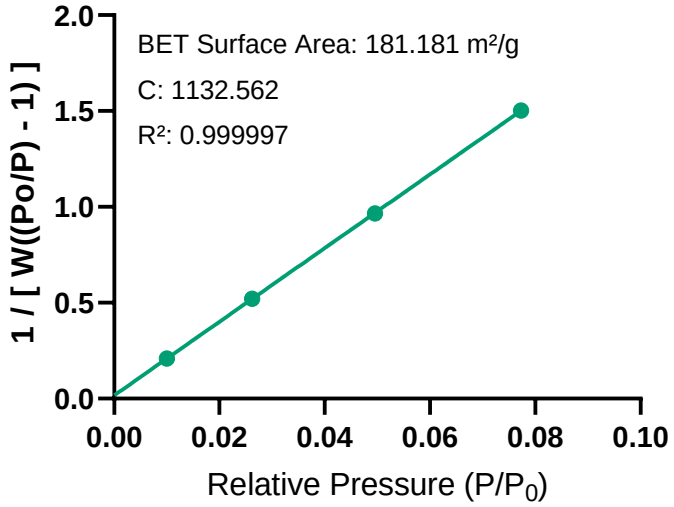

Figure S6.3 Brunauer-Emmett-Teller (BET) surface area plot of the pomegranate SnO_2@C electrocatalyst.

A)

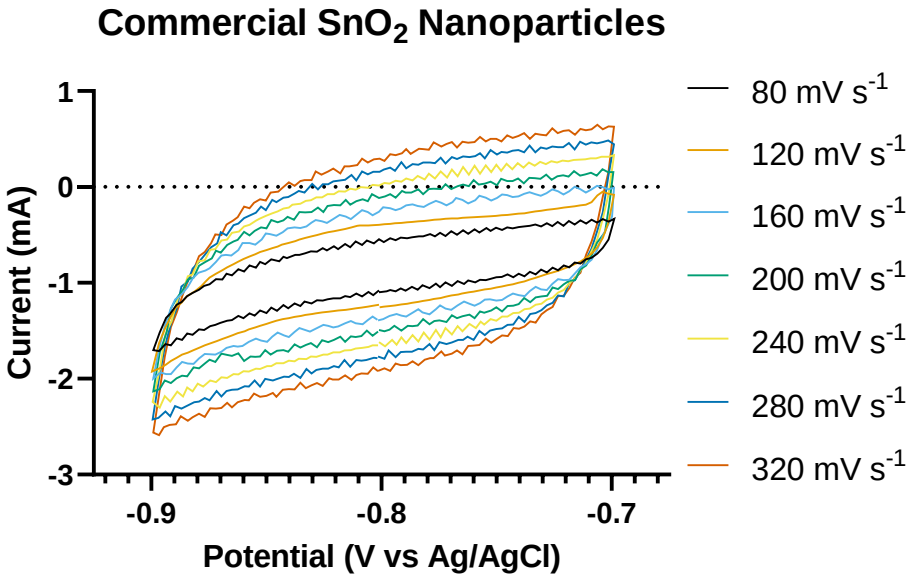
Commercial SnO2 Nanoparticles
Current (mA)
1
0
-1
-2
-3
-0.9
-0.8
-0.7
Potential (V vs Ag/AgCl)
80 mV s-1
120 mV s-1
160 mV s-1
200 mV s-1
240 mV s-1
280 mV s-1
320 mV s-1

B)

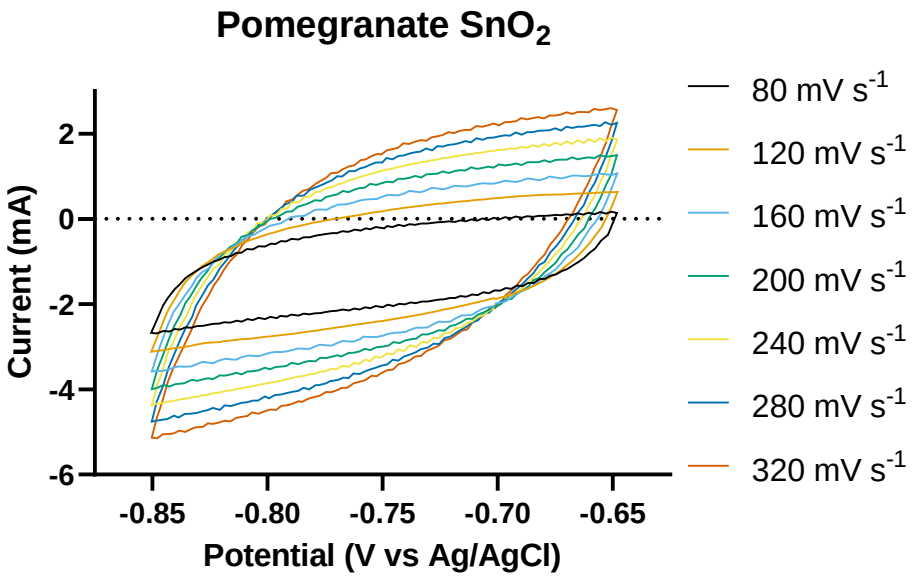
Pomegranate SnO2
Current (mA)
2
0
-2
-4
-6
-0.85
-0.80
-0.75
-0.70
-0.65
Potential (V vs Ag/AgCl)
80 mV s-1
120 mV s-1
160 mV s-1
200 mV s-1
240 mV s-1
280 mV s-1
320 mV s-1

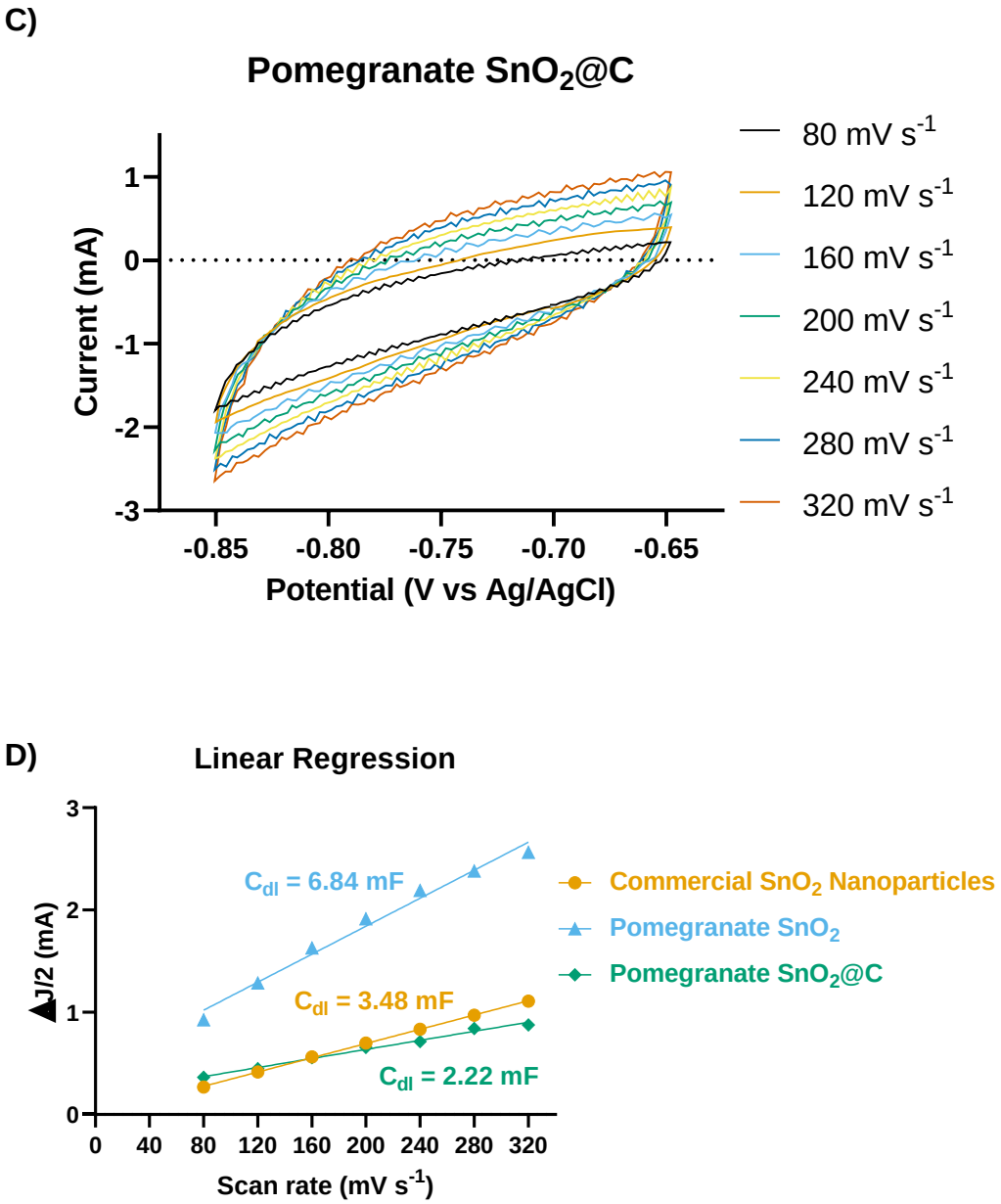

Figure S6.4 Cyclic voltammetry curves in a non-faradaic region at scan rates of 80, 120, 160, 200, 240, 280 and 320 mV s^{-1} for a) Commercial SnO_2 nanoparticles, b) Pomegranate SnO_2 and c) Pomegranate SnO_2@C. d) Linear regression between the current density differences in the middle of the potential window and the scan rate.

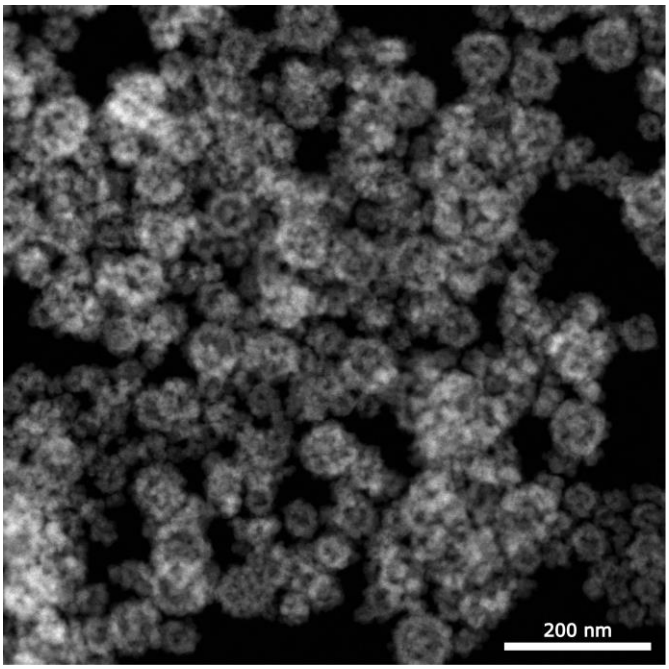

Figure S6.5 HAADF-STEM image of the Pomegranate SnO_2 electrocatalyst before electrochemical CO_2 reduction.

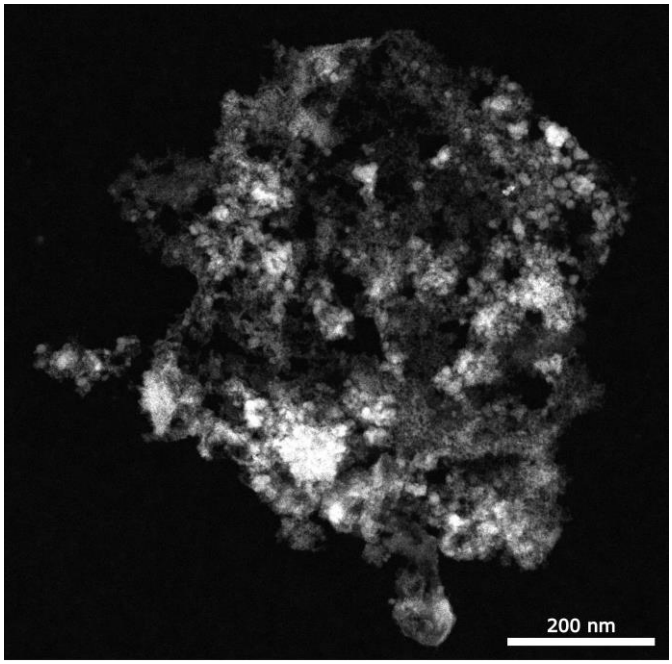

Figure S6.6 HAADF-STEM image of the Pomegranate SnO_2 electrocatalyst after 24 h electrochemical CO_2 reduction.

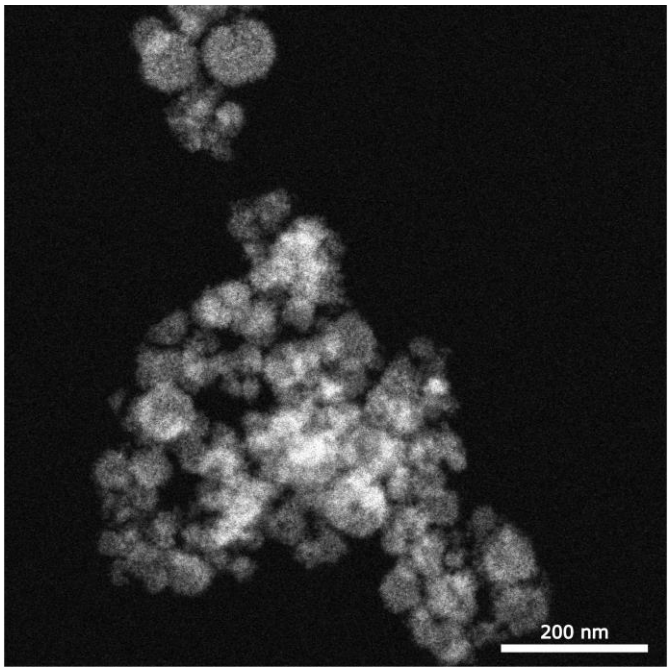

Figure S6.7 HAADF-STEM image of the Pomegranate SnO_2@C electrocatalyst before electrochemical CO_2 reduction.

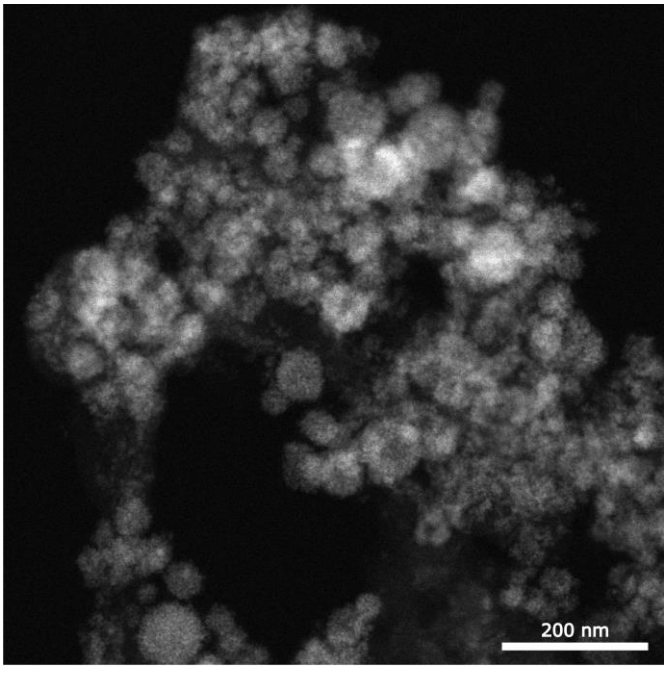

Figure S6.8 HAADF-STEM image of the Pomegranate SnO_2@C electrocatalyst after 24 h electrochemical CO_2 reduction.

Chapter 7

Pulsed-eCO_2R: an exploratory study

Following the identification of *in situ* SnO_2 reduction as the undeniable predominant cause of degradation for the Pom. SnO_2@C electrocatalyst and subsequent recovery of the Faradaic efficiency, an exploratory study of pulsed-eCO_2R is performed to further extend the electrocatalytic stability, without the need to disassemble the electrolyser or introduce air.

Manuscript in preparation.

7.1 Introduction

In the preceding chapter, the use of a carbon shell has been demonstrated to successfully reduce irreversible morphological electrocatalyst degradation, such as segregation/pulverization and agglomeration, clearly observed for the pomegranate-structured SnO_2 electrocatalyst and barely detected for the Pom. SnO_2@C electrocatalyst. Counterintuitively, the Pom. SnO_2@C electrocatalyst, which retained its original morphology much better, displayed a decreasing FE% towards formate over the course of a 24 hour galvanostatic stability measurement. However, this loss of selectivity proved to be of a temporary nature as it was largely restored by leaving the used electrode (GDE) to dry (re-oxidise) in air. Ultimately, after thorough *ex situ* characterisation, this temporary loss of FE_{FA} was attributed to the *in situ* SnO_2 reduction to metallic Sn.[207]

In search of an electrochemical solution to further enhance the stability of this Pom. SnO_2@C electrocatalyst for the electrochemical CO_2 reduction towards formate, an exploratory study of the opportunities of pulsed electrochemical CO_2 reduction (p-eCO$_2$R) was performed.

7.1.1 Introduction to pulsed-eCO$_2$R

For the most part, the eCO$_2$R is performed under steady-state operating conditions at a fixed current or potential. The same holds true for p-eCO$_2$R, both current and potential controlled pulsed electrolysis are possible, however, when pulsating, the steady-state cathodic operating conditions are periodically interrupted by an anodic treatment.[246]

Figure 7.1 illustrates the key concept behind potential controlled p-eCO$_2$R, as performed in this chapter, with E_c and E_a being the applied cathodic and anodic potential, respectively. During a potential controlled p-eCO$_2$R experiment, the applied potential is repeatedly varied between E_c and E_a, which are variables dependent on the utilised electrocatalyst and the intended outcome (discussed hereinafter) of pulsating the operating potential. Another variable is the duration of every pulse, i.e., the cathodic and anodic pulse time (t_c and t_a), which determine the total period of one pulse cycle ($t_p = t_c + t_a$) and thus the pulse frequency ($f_p = 1/t_p$) and are typically classified as "short" (< 1 s) or "long" (> 1 s) pulses.[246]

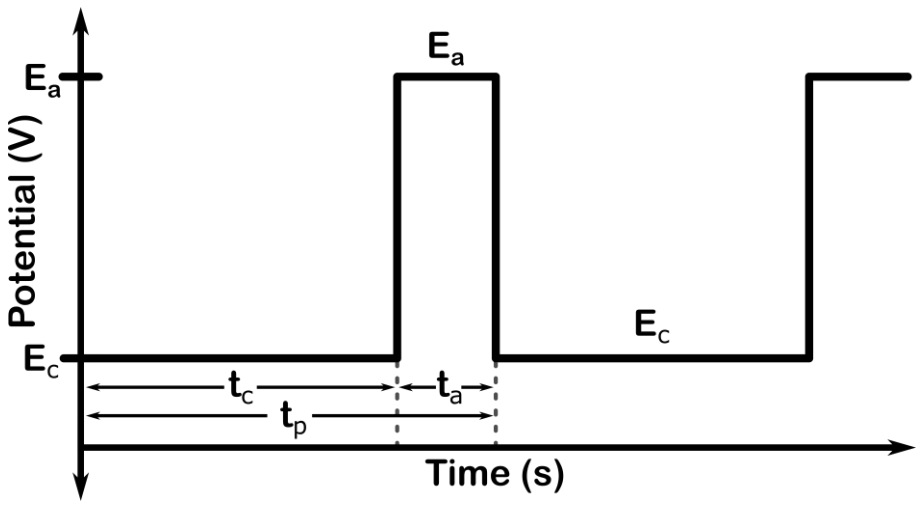

Figure 7.1 Example of an applied pulse profile for pulsed electrochemical CO_2 reduction.

A square wave pulse profile, as depicted in Figure 7.1, is considered to be the most elementary form of p-eCO$_2$R and was utilised here. It should be noted however that more complex waveforms, such as triangular, sawtooth, sinusoidal, etc., could be explored once an in-depth understanding concerning the relationship between the applied pulse and

electrochemical performance (electrocatalytic stability) has been attained.[246] These more complex forms provide an additional degree of freedom in terms of fine-tuning in the sense that the transition between E_c and E_a can be precisely controlled to achieve the desired effect of the transient potential on the electrochemical performance of the electrocatalysts.

Compared to the traditional steady-state potentiostatic (or galvanostatic) eCO$_2$R, a variety of physicochemical processes (Figure 7.2) inherent to heterogeneous electrocatalysis can be manipulated by performing the eCO$_2$R under transient potentiostatic operating conditions. Even though these processes occur simultaneously, carefully designing the applied pulse profile allows for a tailored relative contribution of each at different pulse conditions.[246]

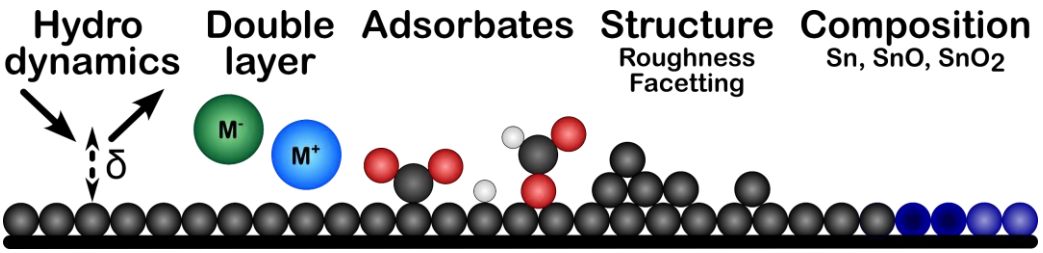

Figure 7.2 Overview of the physicochemical processes of heterogeneous electrocatalysis that may be influenced during p-eCO$_2$R, redrawn from ref.[246]

As previously discussed in Chapter 3, mass transfer optimisation is an important aspect for CO$_2$ electrolysis.[140,141] In this regard, p-eCO$_2$R can be utilised to overcome mass transfer limitations since the depleted CO$_2$ during the cathodic pulse can be replenished during the anodic pulse. In order to achieve this, the anodic pulse should be long enough to

substantially replenish the CO_2, but not too long so that the majority of the pulse cycle is still utilised to reduce CO_2 and the energy penalty doesn't become too high.[247,248] The effectiveness of this CO_2 replenishment during the anodic pulse is highly dependent on the boundary layer thickness (δ). In their research, Gupta *et al.*[247] determined that for a typical boundary layer with a thickness of approximately 100 µm, a t_a of 5 - 10 s is required.[247] Pulsing can thus clearly affect the available CO_2 concentration at the electrocatalyst surface in a positive manner.[246,247]

Furthermore, a sudden change of potential has been reported to drastically rearrange the DL (as discussed in section 3.1.3) and presence of adsorbed species (primarily ions and reaction intermediates). Due to their charged nature (H^+/H_3O^+, OH^-, K^+) and the large dipole moment of several crucial reaction intermediates (•OCHO, •COOH), variations in the electrode polarity are expected to influence their surface coverage.[249] While multiple studies have been performed to gather insight into these dynamic changes of the DL and surface adsorbates on Cu-based electrocatalysts, an in-depth understanding for Sn-based electrocatalysts is still missing.[246]

Finally, various p-eCO$_2$R studies (mainly on Cu-based electrocatalysts) have demonstrated that the electrode structure and chemical nature can be altered during the p-eCO$_2$R, depending on the applied anodic potential (E_a) and pulse duration (t_a).[250–254] As described in detail in Chapter 4, no general agreement concerning the electrocatalytic active site of Sn-based electrocatalysts has been reached. Nonetheless, as evidenced in Chapter 4, 5 and 6, oxides appear to play a crucial role during the eCO$_2$R towards

formate on Sn-based electrocatalysts.[189,207] Combining these observations with the fact that longer anodic pulses (several seconds) have previously been reported to yield surface roughening and morphological changes, as well as the formation of persistent oxides on Cu-based electrocatalysts, it is obvious that p-eCO$_2$R is a valuable approach to diminish/reverse *in situ* SnO$_2$ reduction and thereby prolong Sn-based electrocatalytic stability.[246]

7.1.2 Pulsed-eCO$_2$R state-of-the-art

Shortly after the influential publication by Yoshio Hori *et al.*[58] in 1993, which categorised various monometallic electrodes according to their predominant eCO$_2$R products, Shiratsuchi *et al.*[255] reported the superior, more stable performance of Cu electrodes for the eCO$_2$R towards methane and ethylene under pulsed-eCO$_2$R operating conditions, as compared to the conventional galvanostatic electrolysis. In their research, they demonstrated that periodical interruptions of the cathodic electroreduction with an anodic pulse prolonged the lifetime of their copper electrocatalyst and enhanced the FEs towards CH_4 and C_2H_4.[255]

More recently, p-eCO$_2$R has gained renewed attention, primarily for Cu-based electrocatalysts, as a promising technique to tailor the electrocatalytic performance (selectivity) beyond mainstream attempts such as altering the electrocatalysts' structure (faceting, nanostructuring) and composition (alloying, core-shell), modifying the electrolyte and optimising the electrolyser design.[246,256] Although significant advances have been achieved using these conventional techniques, stability issues

continue to hold back the eCO$_2$R technology.[189,202] Fortunately, numerous reports, utilising both "short" and "long" pulses on various electrocatalysts (Cu,[246,250,253] Ag,[257] Au,[258] Pd[259] and Pb[260]) have described how product selectivity and electrocatalyst lifetimes were positively affected by performing the eCO$_2$R under pulsating operating conditions.[246]

While most state-of-the-art p-eCO$_2$R studies focus on Cu-based electrocatalysts and C_{2+} product formation, Lee *et al.*[259] and Blom *et al.*[260] reported a Pd- and Pb-based electrocatalyst, respectively, for the p-eCO$_2$R towards formate. In their research, Lee *et al.* achieved a remarkable 45 h stable production of formate with a FE_{FA} of 97.8% on a Pd-based electrocatalyst. Inherently, Pd-based electrocatalysts are prone to CO poisoning, which block the active sites and leads to dehydration of the electrocatalyst. Applying a potentiostatic controlled pulse profile (E_c = -0.8 V vs. RHE, t_c = 590 s, E_a = 1.22 V vs. RHE and t_a = 10 s), Lee *et al.* were able to oxidise the adsorbed CO during the anodic pulse, inhibiting CO poisoning and yielding a stable performance for 45 h, whereas under steady-state potentiostatic operating conditions, a 24.1% decrease was observed in the FE_{FA} after merely 6 h.[259] Additionally, Blom *et al.* demonstrated an enhanced and stable formate production of approximately 50% for 16 h on a Pb-based electrocatalyst by pulsating the applied potential during the eCO$_2$R. Investigating both symmetric and asymmetric square wave pulses, they found that longer cycle times caused an increase in formate partial current density. This increase in FE_{FA} was ascribed, using *in situ* Raman spectroscopy and thermodynamic

calculations, to the oxidation of the Pb surface to $PbCO_3$ during the anodic pulse, which is hypothesised to be more selective towards formate production.[260] Despite the opportunities of p-eCO$_2$R to enhance electrocatalytic selectivity and prolong their lifetime, to the best of our knowledge, no p-eCO$_2$R has been reported for Sn-based electrocatalysts. Therefore, in this chapter an exploratory study was performed, investigating the possibility to further enhance the stability of the Pom. SnO_2@C electrocatalyst. By applying several pulse parameter combinations, an initial idea concerning the effect of a transient potential on the electrochemical performance (i.e. selectivity, activity and stability) of the Pom. SnO_2@C electrocatalyst was acquired.

7.2 Experimental

7.2.1 Chemicals

The following chemicals were used as received, without any further purification: d-glucose (anhydrous, biotechnology grade, VWR Life Science), D520 NAFION® solution (Ion Power), ethanol (99.8%, abs. p., Chem-Lab), potassium hydrogen carbonate (99.5+%, v.p., Chem-Lab), potassium hydroxide (85+%, pellets a.r., Chem-Lab), 2-propanol (99.8+%, iso-propanol a.r., Chem-Lab), sodium tin(IV) oxide trihydrate (98%, Alfa Aesar).

7.2.2 Pulsed-eCO$_2$R

The as-synthesised pomegranate-structured SnO_2@C electrodes were prepared by spray coating a Sigracet 39 BB gas diffusion electrode (GDE)

with an ink made from the obtained electrocatalyst powders. For each deposition, 75 mg of the electrocatalyst powder is dispersed with 0.3750 g of a 5 wt% Nafion solution in approximately 10 mL of a 1:1 Milli-Q (18.2 MΩ·cm @ 25 °C):IPA Solution. A GDE of 25 cm^2 is slowly and uniformly spray coated before being divided into 6 smaller GDEs with a projected area of approximately 3 cm^2 and the targeted electrocatalyst loading of 1.5 mg cm^{-2}. These spray coated GDEs were then used as cathodes in a small-flow by electrolyser with a geometric electrochemically active surface area of 1 cm^2.

Pulsed-eCO$_2$R experiments were conducted in the abovementioned flow-by electrolyser (Figure S5.4), examining a variety of parameters with E_c = -2.1 V vs. Ag/AgCl, t_c = 300 s, E_a = -0.5 V or -0.25 V vs. Ag/AgCl and t_a = 10 or 30 s. 1 h p-eCO$_2$R experiments were performed using 12 pulse cycles, while 72 and 288 cycles were used for 6 h and 24 h experiments, respectively. The catholyte, 0.5M $KHCO_3$, was pumped single pass at a flow rate of 2 mL min^{-1}, while the anolyte, 2M KOH, was recycled at an equal flow rate over a Ni foam anode. Furthermore, a Nafion 117 membrane and Ag/AgCl reference electrode were used. Liquid samples were collected during various cycles, in order to determine the FE% towards formate by means of HPLC. The reported data was reproduced three times and an average value is reported for all FE_{FA} and current densities.

7.3 Results and discussion

Seeing as the operating potential of the Pom. SnO$_2$@C electrocatalyst continually becomes more negative, decreasing from -2.11 V to -2.36 V vs. Ag/AgCl, over the course of the 24 h eCO$_2$R experiment, a potential screening was performed to determine the optimal E_c. To this extent, seven different potentials (from -1.8 to -2.4 V vs. Ag/AgCl) were applied and liquid samples were collected and analysed by means of HPLC to determine the FE_{FA}. Figure 7.3 displays the results of this potential screening, revealing an excellent performance with selectivities around 80% at most of the applied potentials. A larger, yet expected, difference was observed in the current response, which varied from 73 ± 2 mA cm^{-2} at -1.8 V vs. Ag/AgCl to 140 ± 6 mA cm^{-2} at -2.4 V vs. Ag/AgCl. -2.1 V vs. Ag/AgCl was chosen as E_c in the p-eCO$_2$R experiments, to maintain approximately the same cathodic conditions as in chapter 6 and thus to maintain a comparable electrocatalyst degradation rate.

As demonstrated in Chapter 6 (Figure 6.7), a decrease in FE_{FA} could be noticed for the Pom. SnO$_2$@C electrocatalyst as early as 4 h after the start of the 24 h galvanostatic eCO$_2$R at 100 mA cm^{-2}. In order to validate the chosen E_c and confirm the comparable electrocatalyst degradation rate, 6 h steady-state potentiostatic eCO$_2$R experiments were performed at -2.1 V vs. Ag/AgCl (Figure 7.4). Starting at an average current density of 101 mA cm^{-2} and a FE_{FA} of 86 ± 4%, the Pom. SnO$_2$@C electrocatalyst display a similar initial selectivity and activity as reported during the galvanostatic (100 mA cm^{-2}) electrolysis experiments in Chapter 6. Furthermore,

throughout the 6 h electrolysis, a similar decrease in FE_{FA} was noticed, starting after approximately 4 h, leading towards a lower FE_{FA} of 70 ± 6% after 6 h of continuous potentiostatic electrolysis, validating the choice of -2.1 V vs. Ag/AgCl as E_c.

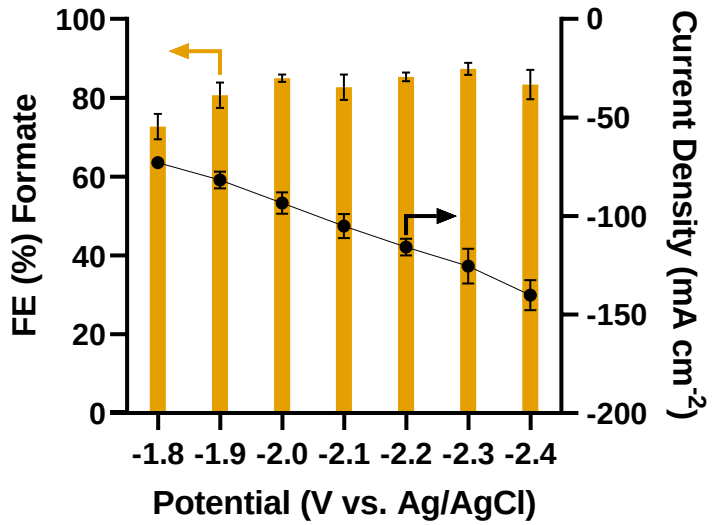

Figure 7.3 Potential screening of the Pom. SnO_2@C electrocatalyst, with an average FE_{FA} and current density (mA cm^{-2}) reported for every potential.

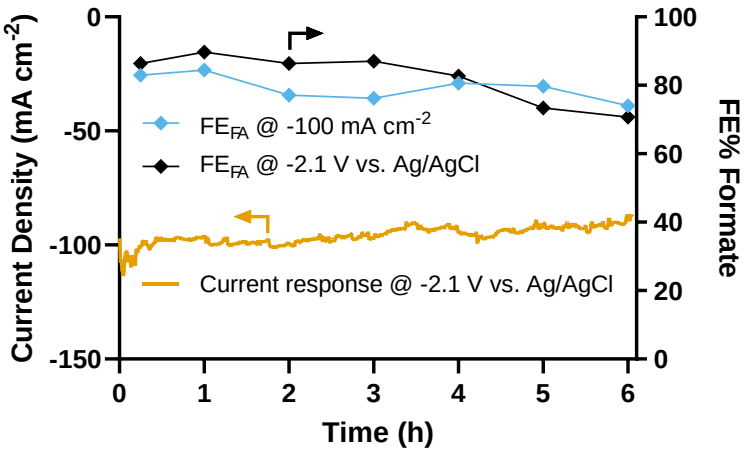

Figure 7.4 Average current density (mA cm^{-2}) and FE_{FA} of the Pom. SnO_2@C electrocatalyst, plotted as function of time (h) at a constant potential of -2.1 V vs. Ag/AgCl for 6 h (yellow and black, respectively), compared with the FE_{FA} during a galvanostatic experiment (blue) at 100 mA cm^{-2} from Chapter 6.

The remaining pulse parameters E_a, t_c and t_a were determined by performing a cyclic voltammetry (E_a) and literature review (t_c and t_a), respectively. At a scan rate of 200 mV s^{-1}, the cyclic voltammetry (Figure 7.5) of the Pom. SnO_2@C electrocatalyst reveals two peaks near -0.5 V and -0.25 V vs. Ag/AgCl, which are attributed to the oxidation of *in situ* reduced Sn^0 to Sn^{2+} and Sn^{2+} to Sn^{4+}, respectively. In Chapter 4, metastable Sn^{2+} oxyhydroxide, was established as the most probable active site for the selective eCO$_2$R towards FA. For this reason, -0.5 V vs. Ag/AgCl was chosen as E_a in order to maximise the *in situ* re-oxidation of the metallic Sn to the more active and selective Sn^{2+}.

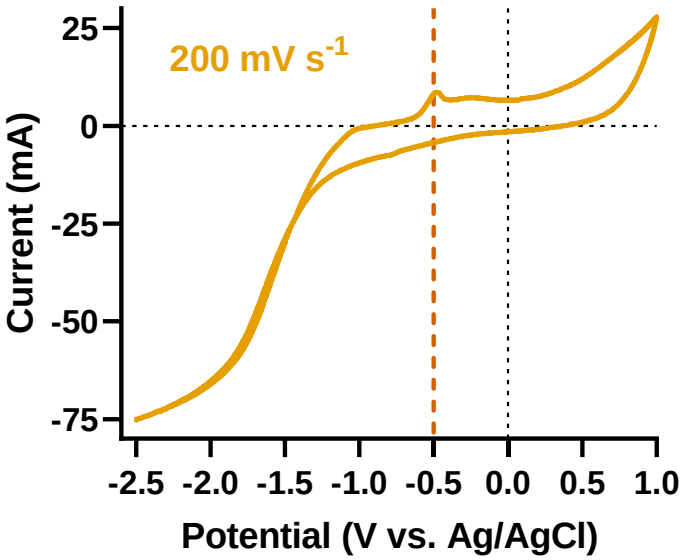

Figure 7.5 Cyclic voltammetry of the Pom. SnO_2@C electrocatalyst, performed at a scan rate of 200 mV s^{-1} in the flow-by electrolyser with 0.5 M $KHCO_3$ as catholyte.

To effectively determine the minimum cathodic and anodic pulse time, the response time of the electrocatalytic system, i.e. resistor-capacitor (RC =

C_{dl} x iR) time constant, needs to be taken into account.[253] With a C_{dl} of 2.22 mF, as determined in Chapter 6 (Figure S6.4D), and a maximum measured Ohmic resistance of 10 Ω in the flow-by electrolyser, applied pulses should therefore at least last longer than 22.20 ms for the electrocatalyst to experience an effect from these alternating potentials.[207,253] Nevertheless, a literature study revealed that surface roughening, morphological changes and the formation of persistent surface oxides predominantly occurs at "longer" pulse times, in the order of seconds.[246] Therefore, as initial parameters, t_c and t_a were fixed at 300 and 10 s, respectively.[246,259,260] With a total pulse time of 310 s, 72 pulse cycles were performed in order to subject the Pom. SnO_2@C electrocatalyst to E_c for a total of 6 h.

Applying these initially selected pulse parameters (E_c = -2.1 V, E_a = -0.5 V vs. Ag/AgCl, t_c = 300, t_a = 10 s) a similar current response and decrease of FE_{FA} was observed, as presented in figure 7.6, compared to the steady-state 6 h potentiostatic electrolysis at -2.1 V vs. Ag/AgCl. On the one hand, the *in situ* SnO_2 reduction is thus insufficiently countered, utilising the aforementioned pulse parameters. On the other hand, this result demonstrates that pulsation of the applied potential has no adverse effect on the electrochemical performance. Improvement can possibly be achieved by adjusting the anodic pulse parameters, such as applying an even more positive anodic potential (E_a = -0.25 V vs. Ag/AgCl) or elongating the anodic pulse time (t_a = 30 s) in an attempt to obtain a more pronounced re-oxidation of the Sn surface layers.

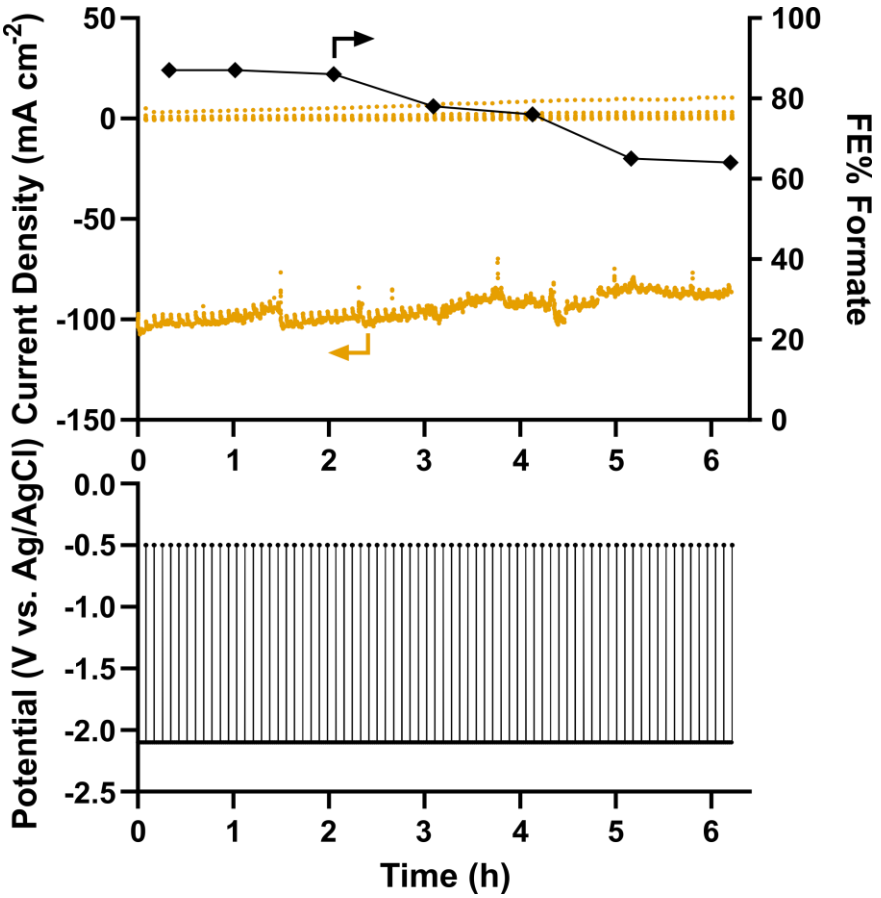

Figure 7.6 Current response and FE_{FA} of the 6 h potentiostatic p-eCO$_2$R of the Pom. SnO$_2$@C electrocatalyst (E_c = -2.1 V, E_a = -0.5 V vs. Ag/AgCl, t_c = 300 s, t_a = 10 s).

By changing the E_a to -0.25 V vs. Ag/AgCl, a faster decay in FE_{FA} and a decrease in current are observed over the course of time (Figure 7.7). While the current response starts at approximately 100 mA cm^{-2}, during the first 12 cycles (1 h of cathodic operation) each subsequent cycle the current response decreases to finally stabilise around a current density of ± 70 mA cm^{-2}. Simultaneously, the FE_{FA} quickly decreases from 84% to 50% after 12 cycles and even further to 33% after 72 cycles, clearly indicating that applying a more positive anodic potential has a disadvantageous effect on

the Pom. SnO$_2$@C electrocatalyst and appears to accelerate electrocatalyst degradation to beyond normal galvanostatic electrolysis for 24 h. Further research combined with an in-depth characterisation (8.2 Perspective) are required to acquire clues to explain this electrochemical behaviour.

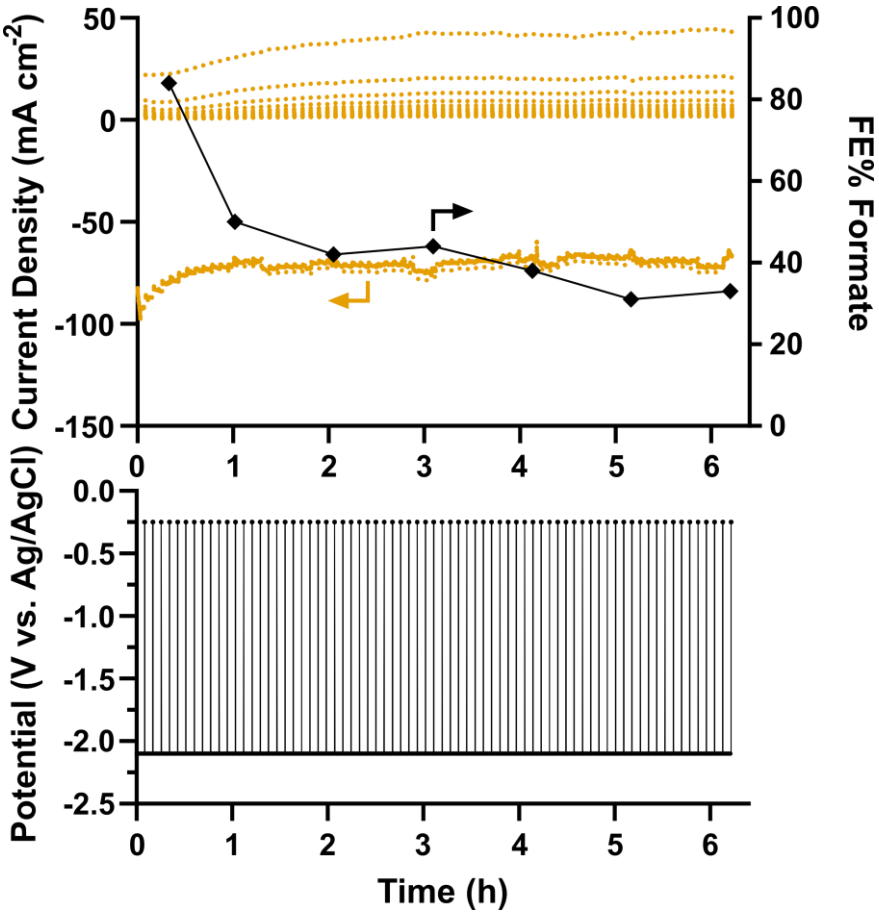

Figure 7.7 Current response and FE$_{FA}$ of the 6 h potentiostatic p-eCO$_2$R of the Pom. SnO$_2$@C electrocatalyst (E_c = -2.1 V, E_a = -0.25 V vs. Ag/AgCl, t_c = 300 s, t_a = 10 s).

Upon elongating the anodic pulse time, t_a, from 10 to 30 s, an improvement in stability could be observed for the Pom. SnO$_2$@C electrocatalyst. The FE$_{FA}$ maintains a high selectivity of 78 ± 2% after 72 cycles of p-eCO$_2$R, exhibiting a smaller decrease of only 6%, whereas previously a decrease of

at least 15% was observed over the same time period (Figure 7.4 and 7.8). Considering these encouraging results, a 288 cycle p-eCO$_2$R electrolysis, corresponding to 24 h of cathodic operation, was performed applying the same pulse parameters (E_c = -2.1 V, E_a = -0.5 V vs. Ag/AgCl, t_c = 300 s, t_a = 30 s).

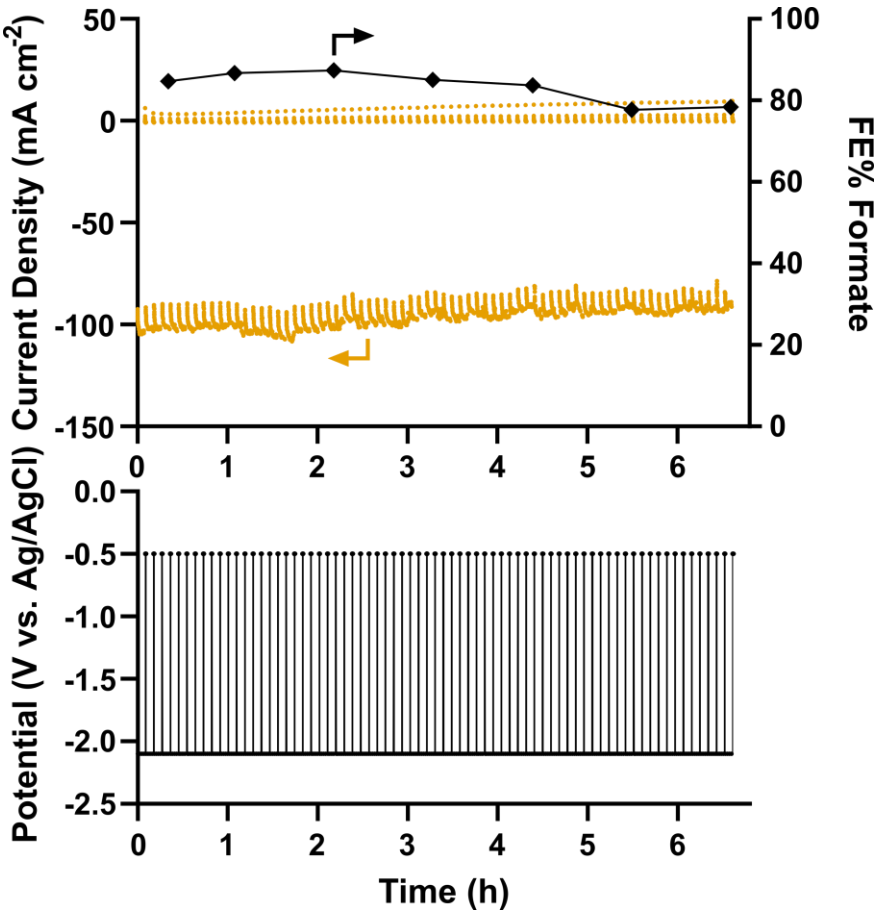

Figure 7.8 Current response and FE_{FA} of the 6 h potentiostatic p-eCO$_2$R of the Pom. SnO$_2$@C electrocatalyst (E_c = -2.1 V, E_a = -0.5 V vs. Ag/AgCl, t_c = 300 s, t_a = 30 s).

Figure 7.9 shows that while pulsating the operating potential appears to slow down the *in situ* SnO$_2$ reduction and electrocatalytic degradation,

ultimately, after 24 h of cathodic operation, the FE_{FA} decreased to 44%, which is similar to the 24 h galvanostatic electrolysis without pulsation, in the previous chapter. Nonetheless, we are confident that additional fine-tuning of the pulse parameters, combined with in-depth physicochemical characterisation can further diminish the *in situ* SnO_2 reduction and enhance the Pom. SnO_2@C electrocatalytic stability as a result.

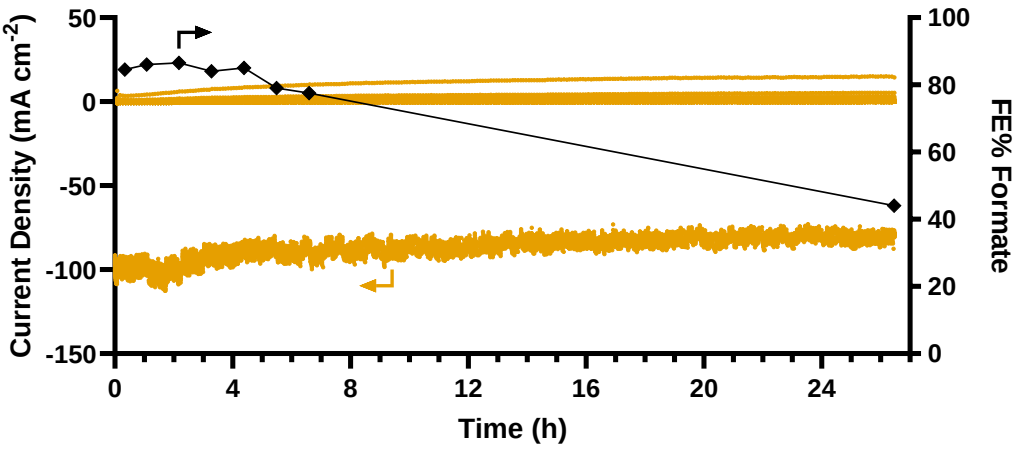

Figure 7.9 Current response and FE_{FA} of the 24 h potentiostatic p-eCO$_2$R of the Pom. SnO$_2$@C electrocatalyst (E_c = -2.1 V, E_a = -0.5 V vs. Ag/AgCl, t_c = 300 s, t_a = 30 s).

7.4 Conclusion

In summary, the p-eCO$_2$R has been demonstrated to be a promising electrochemical technique to tune the electrocatalytic performance and stability beyond conventional endeavours. Precise control over the potentiostatic pulse parameters enables a variety of physicochemical processes to be manipulated *in situ*, without the need to disassemble the electrolyser. By carefully adjusting the initial pulse parameters, derived

from literature and previous experiments, we have successfully slowed down the *in situ* SnO_2 reduction and electrocatalytic degradation of the Pom. SnO_2@C electrocatalyst. Applying these improved pulse parameters, a high selectivity of 78 ± 2% was maintained after 72 cycles (6 h) of p-eCO$_2$R, exhibiting a slight decrease of only 6%, whereas previously a decrease of at least 15% was observed over the same time period under steady-state operating conditions. Unfortunately, the *in situ* SnO_2 wasn't completely nullified as ultimately a similar decrease in FE_{FA} was observed after 24h of p-eCO$_2$R. Therefore, further exploration combined with an in-depth physicochemical characterisation are required to investigate whether it is possible to enhance the electrocatalytic stability even more and to understand the electrochemical performance when adjustment of the pulse parameters improves or diminished the electrocatalytic stability. Nonetheless, these results clearly highlighted, for the first time, the opportunities of p-eCO$_2$R to enhance the stability of the Pom. SnO_2@C and Sn-based electrocatalysts in general. Hopefully, further exploration and optimisation enables the increase of the electrocatalytic stability of Sn-based catalysts beyond the state-of-the-art towards industrially relevant lifetimes.

Chapter 8

Conclusions and perspective

To bring this dissertation to a close, all previous conclusions are linked together, providing a summary of the knowledge and understanding gained during my PhD. In addition, my perspective on future research to continue enhancing the stability of Sn-based electrocatalysts for the electrochemical CO_2 reduction towards formate is presented.

8.1 Conclusions

A comprehensive literature review (Chapter 1) has made it clear that despite an excellent selectivity and activity, the stability of the state-of-the-art Sn-based electrocatalysts leaves much to be desired. Out of the more than 50 reviewed Sn-based electrocatalysts, merely eight have a minimum reported stability of 72 h. To date, the longest reported stable Sn-based electrocatalyst is a homogeneously alloyed $Bi_{0.1}Sn$ crystal, which exhibits a 95% selectivity during a continuous operation at 100 mA cm^{-2} for more than 100 days, without a single trace of degradation.[71]

Moreover, whenever electrocatalytic stability is evaluated, there is currently no consistent approach to this. Current literature showed that stability testing varies from experiments in batch (H-cell) under controlled and less harsh operating conditions compared to electrolyser experiments at more industrially relevant conditions. Although H-cell experiments can also be harsh for the electrocatalyst due to the combination of a low electrocatalyst loading, high overpotential and lower limiting current density because of mass transfer limitations of the dissolved CO_2, all of these results are hard to compare and the necessity for an adequate and unified stability evaluation protocol (Chapter 4) became apparent. Therefore, based on recent literature, we proposed a unified stability evaluation for electrocatalysts which have a minimum stability of 48 h, to be carried out in an electrolyser under industrially relevant operating conditions ($>$ 100 mA cm^{-2}). Once this initial stability of 48 h is obtained, subsequent accelerated degradation tests (ADTs) should be performed in

combination with *ex situ* and *in operando* physicochemical characterisation to gather valuable information regarding their long-term stability and predominant degradation pathways.

In recent years, Sn-based electrocatalysts have moved away from bulk Sn towards advanced, rationally designed nanostructures, such as nanoparticles, alloys, core-shell nanoparticles, oxides, sulfides, etc. While this transition has proven to be beneficial in terms of selectivity and activity, they are still subject to numerous degradation mechanisms, such as reshaping, agglomeration, pulverisation, particle detachment, dissolution, Ostwald ripening, poisoning and *in situ* SnO_2 reduction. Although their electrochemical performance is highly dependent on the local environment, which in turn is influenced by electrolyser design and experimental parameters, in this dissertation we have solely focused on Sn-based electrocatalyst degradation in order to acquire an in-depth understanding concerning their most predominant degradation pathways and the effectiveness of several mitigation strategies to enhance their stability by rational electrocatalyst (Chapter 5 and 6) and pulse profile (p-eCO_2R, Chapter 7) design.

Driven by rational electrocatalyst design, SnO_2-N-OMC electrocatalysts were synthesised in Chapter 5, combining selective SnO_2 with an N-OMC carbon capture medium for the eCO_2R towards FA. Utilising a minimal amount of SnO_2, the best performing SnO_2-N-OMC electrocatalysts required a low overpotential for the conversion of CO_2 towards FA with a FE_{FA} of $\pm$ 60% at a current density of 100 mA cm^{-2}. Over the course of a

24 h eCO_2R experiment, the FE_{FA} of SnO_2-N-OMC (6) decreased from 59% to 12%, while the SnO_2-N-OMC (2) electrocatalyst exhibited a smaller loss in FE_{FA} from 61% to 43%. *Ex situ* HAADF-STEM and EDS elemental mapping revealed the morphological degradation through pulverization and agglomeration and the *in situ* SnO_2 reduction of the SnO_2 active species. In the case of SnO_2-N-OMC (2), however, this *in situ* SnO_2 was more offset by the pulverization of large SnO_2 species, revealing 'fresh' and selective SnO_2 active sites for the eCO_2R towards FA, explaining difference in long-term electrochemical performance for both SnO_2-N-OMC electrocatalysts. Consequently, we concluded that while morphological stability of the Sn-based electrocatalyst is important in the long run, chemical stability to withstand *in situ* SnO_2 reduction appears to be more crucial as this directly correlates to a severe loss in selectivity. Furthermore, our exploration of the interplay between SnO_2 and the N-OMC carbon capture medium support material revealed that an optimal combination of both SnO_2 species and the N-OMC carbon capture medium could result in a synergistic effect for the eCO_2R towards FA, especially when utilization of the N-OMC support material and incorporation of the SnO_2 species is optimized to morphologically stabilize the SnO_2 active species.

In an attempt to optimise the utilisation of carbon to morphologically stabilise the active SnO_2 species by means of the particle confinement strategy, in Chapter 6, pomegranate-structured SnO_2 (Pom. SnO_2) and –SnO_2@C (Pom. SnO_2@C) nanocomposite electrocatalysts where

synthesised and examined. Yielding an average FE_{FA} of 83% during 24 h of electrolysis, the Pom. SnO_2 electrocatalyst belongs amongst the best of the state-of-the-art. Despite being covered with a heterogeneous carbon shell, the Pom. SnO_2@C electrocatalyst displayed a decreasing FE_{FA} from 86% to 46% over the course of 24 h at 100 mA cm^{-2}. *Ex situ* HAADF-STEM imaging revealed that regardless of this loss in selectivity, the Pom. SnO_2@C displayed a better morphological stability, compared to the Pom. SnO_2 electrocatalyst. Furthermore, this loss of selectivity proved to be reversible, since its FE_{FA} was largely restored to its original selectivity by leaving the electrode to dry in air. Using *ex situ* XRD and XPS, this temporary selectivity loss was unambiguously linked to the *in situ* SnO_2 reduction, similar to SnO_2-N-OMC electrocatalysts in Chapter 5. While this electrochemical degradation occurred in both electrocatalysts, it was more pronounced in the Pom. SnO_2@C electrocatalyst since it wasn't offset by morphological electrocatalyst degradation. In the longer term, the Pom. SnO_2 is expected to likewise lose its selectivity, which might not be reversible since it is accompanied by morphological degradation, unlike for the Pom. SnO_2@C electrocatalyst.

Finally, in Chapter 7, potential controlled pulsed-eCO_2R (p-eCO_2R) was explored in an endeavour to counteract the remaining and most predominant degradation pathway, i.e. *in situ* SnO_2 reduction, of the Pom. SnO_2@C. Under steady-state operating conditions (100 mA cm^{-2} or -2.1 V vs. Ag/AgCl), the Pom. SnO_2@C electrocatalyst exhibits a decrease in FE_{FA} of at least 15% over a time period of 6 h. Rational design of the pulse

profile enabled us to enhance its stability, diminishing this decrease in FE_{FA} to only 6%, maintaining a high FE_{FA} of 78 ± 2% after 72 cycles (or 6 h) of p-eCO_2R. After 24 h (or 288 cycles) of p-eCO_2R however, the FE_{FA} decreased to 44%, which is similar to the electrochemical performance under steady-state (-100 mA cm^{-2}) operating conditions. Nevertheless, these results clearly demonstrate the opportunities of p-eCO_2R to further enhance the stability of the Pom. SnO_2@C- and Sn-based electrocatalysts by slowing down the *in situ* SnO_2 reduction and require further exploration and fine-tuning to bring the electrocatalytic stability of Sn-based electrocatalysts beyond the state-of-the-art towards industrially relevant lifetimes.

8.2 Perspective

Throughout this dissertation, the degradation and associated stability of Sn-based electrocatalysts were the prime focus. Based on state-of-the-art literature, the most predominant degradation mechanisms were identified, whereafter several 'novel' Sn-based electrocatalysts were synthesised utilising the particle confinement strategy. After successfully increasing the morphological stability, through the use of carbon, an exploratory study of p-eCO_2R revealed great potential to further enhance Sn-based electrocatalytic stability by delaying the *in situ* SnO_2 reduction. In order to continue enhancing the stability of Sn-based electrocatalysts for the electrochemical CO_2 reduction towards formate, aiming at higher TRLs, several research paths may be considered.

In Chapter 4, we've argued that in order to bring the eCO_2R towards formate to an industrial feasibility, Sn-based electrocatalysts and CO_2 electrolysers should be optimised in conjunction. Nevertheless, more fundamental research concerning Sn-based electrocatalysts, unravelling the electrocatalytic active site, investigating electrocatalyst degradation, stability, etc., provides crucial knowledge and insights into the *in situ* behaviour of Sn-based electrocatalysts. To this extent, the particle confinement strategy, which showed great results in this dissertation, could further be explored, optimising the carbon shell coverage, activating the carbon for the eCO_2R towards FA by boron doping[261,262] and extending this particle confinement strategy to other state-of-the-art Sn-based electrocatalysts with reported morphological degradation. Additionally, the synthesis of 'novel' Sn-based electrocatalysts could be extended beyond the common metallic Sn and SnO_2 species to various $Sn_6O_4(OH)_4$ and SnO morphologies.

Aside from increasing stability through rational electrocatalyst design and synthesis, p-eCO_2R appears to be a promising electrochemical technique to manipulate the Sn oxidation state and consequently the FE_{FA} *in situ*. Since this p-eCO_2R is currently predominantly being studied for Cu- and to a lesser extent Ag-based electrocatalysts, supplementary research regarding the effects of transient working potentials on Sn-based electrocatalysts, in combination with physicochemical characterisation, are suggested to unlock the full potential of this emerging electrochemical technique.

Finally, in order to transpose the Sn-based electrocatalyst assisted eCO_2R towards FA from laboratory scale towards industrial application (pilot scale), it is imperative to optimise the entire system, i.e. electrocatalyst (cathode and anode), electrolyser, membrane, downstream processing, etc., concurrently. An adequate stability evaluation by means of the discussed metrics (Figures of merit), techniques and protocols (ADTs) is suggested.

List of Figures

List of Tables

Bibliography

1. Mitchell, J. F. B. The "Greenhouse" effect and climate change. *Rev. Geophys.* 27, 115–139 (1989).

2. Obama, B. The irreversible momentum of clean energy. *Science (80- .).* 355, 126–129 (2017).

3. Malhi, G. S., Kaur, M. & Kaushik, P. Impact of Climate Change on Agriculture and Its Mitigation Strategies: A Review. *Sustainability* 13, 1318 (2021).

4. Friedlingstein, P. *et al.* Global Carbon Budget 2022. *Earth Syst. Sci. Data* 14, 4811–4900 (2022).

5. Rogelj, J. *et al.* Paris Agreement climate proposals need a boost to keep warming well below 2 °C. *Nature* 534, 631–639 (2016).

6. IPCC. *Climate Change 2021: The Physical Science Basis. Contribution of Working Group I to the Sixth Assessment Report of the Intergovernmental Panel on Climate Change. Cambridge University Press* (2021).

7. Mac Dowell, N., Fennell, P. S., Shah, N. & Maitland, G. C. The role of CO2 capture and utilization in mitigating climate change. *Nat. Clim. Chang.* 7, 243–249 (2017).

8. Meinshausen, M. *et al.* Realization of Paris Agreement pledges may limit warming just below 2 °C. *Nature* 604, 304–309 (2022).

9. Tebaldi, C. *et al.* Extreme sea levels at different global warming levels. *Nat. Clim. Chang.* 11, 746–751 (2021).

10. Andrews, O., Le Quéré, C., Kjellstrom, T., Lemke, B. & Haines, A. Implications for workability and survivability in populations exposed to extreme heat under climate change: a modelling study. *Lancet Planet. Heal.* 2, e540–e547 (2018).

11. Arnell, N. W., Lowe, J. A., Challinor, A. J. & Osborn, T. J. Global

and regional impacts of climate change at different levels of global temperature increase. *Clim. Change* 155, 377–391 (2019).

12. Sherwood, S. C. & Huber, M. An adaptability limit to climate change due to heat stress. *Proc. Natl. Acad. Sci.* 107, 9552–9555 (2010).

13. Peters, G. P. *et al.* The challenge to keep global warming below 2 °C. *Nat. Clim. Chang.* 3, 4–6 (2013).

14. Le Quéré, C. *et al.* Temporary reduction in daily global CO2 emissions during the COVID-19 forced confinement. *Nat. Clim. Chang.* 10, 647–653 (2020).

15. Tollefson, J. COVID curbed carbon emissions in 2020 — but not by much. *Nature* 589, 343–343 (2021).

16. Liu, Z. *et al.* Near-real-time monitoring of global CO2 emissions reveals the effects of the COVID-19 pandemic. *Nat. Commun.* 11, 5172 (2020).

17. Liu, Z. *et al.* Global patterns of daily CO2 emissions reductions in the first year of COVID-19. *Nat. Geosci.* 15, 615–620 (2022).

18. Mikulčić, H. *et al.* Flexible Carbon Capture and Utilization technologies in future energy systems and the utilization pathways of captured CO2. *Renew. Sustain. Energy Rev.* 114, 109338 (2019).

19. Cano, Z. P. *et al.* Batteries and fuel cells for emerging electric vehicle markets. *Nat. Energy* 3, 279–289 (2018).

20. Peters, G. P. *et al.* Key indicators to track current progress and future ambition of the Paris Agreement. *Nat. Clim. Chang.* 7, 118–122 (2017).

21. Chen, S., Liu, J., Zhang, Q., Teng, F. & McLellan, B. C. A critical review on deployment planning and risk analysis of carbon capture, utilization, and storage (CCUS) toward carbon neutrality. *Renew. Sustain. Energy Rev.* 167, 112537 (2022).

22. Wang, T., Park, A. H. A., Shi, Y. & Gadikota, G. Carbon Dioxide Capture and Utilization - Closing the Carbon Cycle. *Energy and Fuels* 33, 1693 (2019).

23. Wei, Y.-M. *et al.* A proposed global layout of carbon capture and storage in line with a 2 °C climate target. *Nat. Clim. Chang.* 11, 112–118 (2021).

24. Mertens, J. *et al.* Carbon capture and utilization: More than hiding CO2 for some time. *Joule* 1–8 (2023). doi:10.1016/j.joule.2023.01.005

25. Gabrielli, P., Gazzani, M. & Mazzotti, M. The Role of Carbon Capture and Utilization, Carbon Capture and Storage, and Biomass to Enable a Net-Zero-CO 2 Emissions Chemical Industry. *Ind. Eng. Chem. Res.* 59, 7033–7045 (2020).

26. Kätelhön, A., Meys, R., Deutz, S., Suh, S. & Bardow, A. Climate change mitigation potential of carbon capture and utilization in the chemical industry. *Proc. Natl. Acad. Sci.* 116, 11187–11194 (2019).

27. Wang, X. & Song, C. Carbon Capture From Flue Gas and the Atmosphere: A Perspective. *Front. Energy Res.* 8, (2020).

28. McQueen, N. *et al.* A review of direct air capture (DAC): scaling up commercial technologies and innovating for the future. *Prog. Energy* 3, 032001 (2021).

29. Wilberforce, T., Olabi, A. G., Sayed, E. T., Elsaid, K. & Abdelkareem, M. A. Progress in carbon capture technologies. *Sci. Total Environ.* 761, 143203 (2021).

30. Osman, A. I., Hefny, M., Abdel Maksoud, M. I. A., Elgarahy, A. M. & Rooney, D. W. Recent advances in carbon capture storage and utilisation technologies: a review. *Environ. Chem. Lett.* 19, 797–849 (2021).

31. Raza, A., Gholami, R., Rezaee, R., Rasouli, V. & Rabiei, M. Significant aspects of carbon capture and storage – A review. *Petroleum* 5, 335–340 (2019).

32. Kondratenko, E. V., Mul, G., Baltrusaitis, J., Larrazábal, G. O. & Pérez-Ramírez, J. Status and perspectives of CO2 conversion into fuels and chemicals by catalytic, photocatalytic and electrocatalytic processes. *Energy Environ. Sci.* 6, 3112 (2013).

33. Valluri, S., Claremboux, V. & Kawatra, S. Opportunities and challenges in CO2 utilization. *J. Environ. Sci.* 113, 322–344 (2022).

34. Kortlever, R., Shen, J., Schouten, K. J. P., Calle-Vallejo, F. & Koper, M. T. M. Catalysts and Reaction Pathways for the Electrochemical Reduction of Carbon Dioxide. *J. Phys. Chem. Lett.* 6, 4073–4082 (2015).

35. Vasileff, A., Zheng, Y. & Qiao, S. Z. Carbon Solving Carbon's Problems: Recent Progress of Nanostructured Carbon-Based Catalysts for the Electrochemical Reduction of CO2. *Adv. Energy Mater.* 7, 1–21 (2017).

36. Larrazábal, G. O., Martín, A. J. & Pérez-Ramírez, J. Building Blocks for High Performance in Electrocatalytic CO2 Reduction: Materials, Optimization Strategies, and Device Engineering. *J. Phys. Chem. Lett.* 8, 3933–3944 (2017).

37. Stephens, I. E. L. *et al.* 2022 roadmap on low temperature electrochemical CO 2 reduction. *J. Phys. Energy* 4, 042003 (2022).

38. Khezri, B., Fisher, A. C. & Pumera, M. CO2 reduction: The quest for electrocatalytic materials. *J. Mater. Chem. A* 5, 8230–8246 (2017).

39. Grim, R. G. *et al.* Transforming the carbon economy: challenges and opportunities in the convergence of low-cost electricity and reductive CO 2 utilization. *Energy Environ. Sci.* 13, 472–494 (2020).

40. Birdja, Y. Y. *et al.* Advances and challenges in understanding the electrocatalytic conversion of carbon dioxide to fuels. *Nat. Energy* 4, 732–745 (2019).

41. Pei, Y., Zhong, H. & Jin, F. A brief review of electrocatalytic reduction of CO 2 —Materials, reaction conditions, and devices.

Energy Sci. Eng. 9, 1012–1032 (2021).

42. Bushuyev, O. S. *et al.* What Should We Make with CO2 and How Can We Make It? *Joule* 2, 825–832 (2018).

43. Sun, Z., Ma, T., Tao, H., Fan, Q. & Han, B. Fundamentals and Challenges of Electrochemical CO2 Reduction Using Two-Dimensional Materials. *Chem* 3, 560–587 (2017).

44. Kibria, M. G. *et al.* Electrochemical CO2 Reduction into Chemical Feedstocks: From Mechanistic Electrocatalysis Models to System Design. *Adv. Mater.* 31, 1–24 (2019).

45. Shin, H., Hansen, K. U. & Jiao, F. Techno-economic assessment of low-temperature carbon dioxide electrolysis. *Nat. Sustain.* 4, 911–919 (2021).

46. Somoza-Tornos, A., Guerra, O. J., Crow, A. M., Smith, W. A. & Hodge, B.-M. Process modeling, techno-economic assessment, and life cycle assessment of the electrochemical reduction of CO2: a review. *iScience* 24, 102813 (2021).

47. Chen, C., Khosrowabadi Kotyk, J. F. & Sheehan, S. W. Progress toward Commercial Application of Electrochemical Carbon Dioxide Reduction. *Chem* 4, 2571–2586 (2018).

48. Spurgeon, J. M. & Kumar, B. A comparative technoeconomic analysis of pathways for commercial electrochemical CO 2 reduction to liquid products. *Energy Environ. Sci.* 11, 1536–1551 (2018).

49. Debergh, P. *et al.* The Economics of Electrochemical Syngas Production via Direct Air Capture. *ACS Energy Lett.* 8, 3398–3403 (2023).

50. Yang, Z., Oropeza, F. E. & Zhang, K. H. L. P-block metal-based (Sn, In, Bi, Pb) electrocatalysts for selective reduction of CO 2 to formate. *APL Mater.* 8, 060901 (2020).

51. Thijs, B., Rongé, J. & Martens, J. A. Matching emerging formic acid synthesis processes with application requirements. *Green Chem.* 24, 2287–2295 (2022).

52. Pérez-Fortes, M., Schöneberger, J. C., Boulamanti, A., Harrison, G. & Tzimas, E. Formic acid synthesis using CO2 as raw material: Techno-economic and environmental evaluation and market potential. *Int. J. Hydrogen Energy* 41, 16444–16462 (2016).

53. Ramdin, M. *et al.* High-Pressure Electrochemical Reduction of CO2 to Formic Acid/Formate: Effect of pH on the Downstream Separation Process and Economics. *Ind. Eng. Chem. Res.* 58, 22718–22740 (2019).

54. Agarwal, A. S., Zhai, Y., Hill, D. & Sridhar, N. The electrochemical reduction of carbon dioxide to formate/formic acid: Engineering and economic feasibility. *ChemSusChem* 4, 1301–1310 (2011).

55. Rumayor, M., Dominguez-Ramos, A., Perez, P. & Irabien, A. A techno-economic evaluation approach to the electrochemical reduction of CO2 for formic acid manufacture. *J. CO2 Util.* 34, 490–499 (2019).

56. Tufa, R. A. *et al.* Towards highly efficient electrochemical CO2 reduction: Cell designs, membranes and electrocatalysts. *Appl. Energy* 277, 115557 (2020).

57. Zhang, W. *et al.* Progress and Perspective of Electrocatalytic CO2 Reduction for Renewable Carbonaceous Fuels and Chemicals. *Adv. Sci.* 5, (2018).

58. Hori, Y., Wakebe, H. H. I., Tsukamoto, T. & Koga, O. Electrocatalytic Process of CO Selectivity in Electrochemical Reduction of CO2 at Metal Electrodes in Aqueous Media. *Electrochim. Acta* 39, 1833–1839 (1994).

59. Yoo, J. S., Christensen, R., Vegge, T., Nørskov, J. K. & Studt, F. Theoretical Insight into the Trends that Guide the Electrochemical Reduction of Carbon Dioxide to Formic Acid. *ChemSusChem* 9, 358–363 (2016).

60. An, X. *et al.* Common strategies for improving the performances of tin and bismuth-based catalysts in the electrocatalytic reduction of

CO2 to formic acid/formate. *Renew. Sustain. Energy Rev.* 143, 110952 (2021).

61. Ding, P. *et al.* Metal-based electrocatalytic conversion of CO 2 to formic acid/formate. *J. Mater. Chem. A* 8, 21947–21960 (2020).

62. Turekian, K. K. & Wedepohl, K. H. Distribution of the Elements in Some Major Units of the Earth's Crust. *Geol. Soc. Am. Bull.* 72, 175–192 (1961).

63. Hara, K., Kudo, A. & Sakata, T. Electrochemical reduction of carbon dioxide under high pressure on various electrodes in an aqueous electrolyte. *J. Electroanal. Chem.* 391, 141–147 (1995).

64. Henckens, T. Scarce mineral resources: Extraction, consumption and limits of sustainability. *Resour. Conserv. Recycl.* 169, 105511 (2021).

65. Masel, R. I. *et al.* An industrial perspective on catalysts for low-temperature CO2 electrolysis. *Nat. Nanotechnol.* 16, 118–128 (2021).

66. Zhao, S. *et al.* Advances in Sn-Based Catalysts for Electrochemical CO2 Reduction. *Nano-Micro Lett.* 11, 62 (2019).

67. Li, Q. *et al.* Energy storage through CO2 electroreduction: A brief review of advanced Sn-based electrocatalysts and electrodes. *J. CO2 Util.* 27, 48–59 (2018).

68. Wang, Y., Liu, J., Wang, Y., Al-Enizi, A. M. & Zheng, G. Tuning of CO2 Reduction Selectivity on Metal Electrocatalysts. *Small* 13, 1–15 (2017).

69. He, J., Johnson, N. J. J., Huang, A. & Berlinguette, C. P. Electrocatalytic Alloys for CO2 Reduction. *ChemSusChem* 11, 48–57 (2018).

70. Yin, Z., Palmore, G. T. R. & Sun, S. Electrochemical Reduction of CO2 Catalyzed by Metal Nanocatalysts. *Trends Chem.* 1, 739–750 (2019).

71. Li, L. *et al.* Stable, active CO2 reduction to formate via redox-modulated stabilization of active sites. *Nat. Commun.* 12, 5223 (2021).

72. Yang, H., Kaczur, J. J., Sajjad, S. D. & Masel, R. I. Electrochemical conversion of CO2 to formic acid utilizing Sustainion^{TM} membranes. *J. CO2 Util.* 20, 208–217 (2017).

73. Wu, J., Sun, S.-G. & Zhou, X.-D. Origin of the performance degradation and implementation of stable tin electrodes for the conversion of CO2 to fuels. *Nano Energy* 27, 225–229 (2016).

74. Ko, Y.-J. *et al.* Exploring dopant effects in stannic oxide nanoparticles for CO2 electro-reduction to formate. *Nat. Commun.* 13, 2205 (2022).

75. Kim, Y. E. *et al.* Leaching-resistant SnO2/γ-Al2O3 nanocatalyst for stable electrochemical CO2 reduction into formate. *J. Ind. Eng. Chem.* 78, 73–78 (2019).

76. Cheng, C. *et al.* Amorphous Sn(HPO4)2-derived phosphorus-modified Sn/SnO core/shell catalyst for efficient CO2 electroreduction to formate. *J. Energy Chem.* (2023). doi:10.1016/j.jechem.2022.12.022

77. Wen, G. *et al.* Orbital Interactions in Bi-Sn Bimetallic Electrocatalysts for Highly Selective Electrochemical CO 2 Reduction toward Formate Production. *Adv. Energy Mater.* 8, 1802427 (2018).

78. Lim, J., Kang, P. W., Jeon, S. S. & Lee, H. Electrochemically deposited Sn catalysts with dense tips on a gas diffusion electrode for electrochemical CO 2 reduction. *J. Mater. Chem. A* 8, 9032–9038 (2020).

79. Wang, J. *et al.* In-Sn alloy core-shell nanoparticles: In-doped SnOx shell enables high stability and activity towards selective formate production from electrochemical reduction of CO2. *Appl. Catal. B Environ.* 288, 119979 (2021).

80. Liu, S. *et al.* Stable nanoporous Sn/SnO2 composites for efficient electroreduction of CO2 to formate over wide potential range. *Appl. Mater. Today* 13, 135–143 (2018).

81. Wang, X. *et al.* Polycrystalline SnS x nanofilm enables CO 2 electroreduction to formate with high current density. *Chem. Commun.* 58, 7654–7657 (2022).

82. Zheng, X. *et al.* Theory-guided Sn/Cu alloying for efficient CO2 electroreduction at low overpotentials. *Nat. Catal.* 2, 55–61 (2019).

83. Yang, Q. *et al.* Novel Bi-Doped Amorphous SnOx Nanoshells for Efficient Electrochemical CO2 Reduction into Formate at Low Overpotentials. *Adv. Mater.* 32, 1–7 (2020).

84. Lei, F. *et al.* Metallic tin quantum sheets confined in graphene toward high-efficiency carbon dioxide electroreduction. *Nat. Commun.* 7, 12697 (2016).

85. Kim, M. K. *et al.* Design of less than 1 nm Scale Spaces on SnO 2 Nanoparticles for High-Performance Electrochemical CO 2 Reduction. *Adv. Funct. Mater.* 32, 2107349 (2022).

86. Wang, J. *et al.* Heterostructured intermetallic CuSn catalysts: High performance towards the electrochemical reduction of CO2 to formate. *J. Mater. Chem. A* 7, 27514–27521 (2019).

87. Zheng, X. *et al.* Sulfur-Modulated Tin Sites Enable Highly Selective Electrochemical Reduction of CO2 to Formate. *Joule* 1, 794–805 (2017).

88. Ye, K. *et al.* In Situ Reconstruction of a Hierarchical Sn-Cu/SnO x Core/Shell Catalyst for High-Performance CO 2 Electroreduction . *Angew. Chemie* 132, 4844–4851 (2020).

89. Li, H. *et al.* Selective electroreduction of CO2 to formate over the co-electrodeposited Cu/Sn bimetallic catalyst. *Mater. Today Energy* 21, 100797 (2021).

90. Nguyen-Phan, T.-D. *et al.* High current density electroreduction of CO2 into formate with tin oxide nanospheres. *Sci. Rep.* 12, 8420 (2022).

91. Li, F., Chen, L., Knowles, G. P., MacFarlane, D. R. & Zhang, J. Hierarchical Mesoporous SnO2Nanosheets on Carbon Cloth: A Robust and Flexible Electrocatalyst for CO2Reduction with High Efficiency and Selectivity. *Angew. Chemie - Int. Ed.* 56, 505–509 (2017).

92. Luc, W. *et al.* Ag-sn bimetallic catalyst with a core-shell structure for CO2 reduction. *J. Am. Chem. Soc.* 139, 1885–1893 (2017).

93. Zhao, Y., Liang, J., Wang, C., Ma, J. & Wallace, G. G. Tunable and Efficient Tin Modified Nitrogen-Doped Carbon Nanofibers for Electrochemical Reduction of Aqueous Carbon Dioxide. *Adv. Energy Mater.* 8, 1–9 (2018).

94. Lucas, F. W. S. & Lima, F. H. B. Electrodeposited Tin-Antimony Alloys as Novel Electrocatalysts for Selective and Stable Carbon Dioxide Reduction to Formate. *ChemElectroChem* 7, 3733–3742 (2020).

95. Lai, Q., Yang, N. & Yuan, G. Highly efficient In–Sn alloy catalysts for electrochemical reduction of CO2 to formate. *Electrochem. commun.* 83, 24–27 (2017).

96. Li, Z. *et al.* Fabrication of Bi/Sn bimetallic electrode for high-performance electrochemical reduction of carbon dioxide to formate. *Chem. Eng. J.* 428, 130901 (2022).

97. Liu, Z., Liu, C., Mao, S. & Huang, X. Heterogeneous Structure of Sn/SnO 2 Constructed via Phase Engineering for Efficient and Stable CO 2 Reduction. *ACS Appl. Mater. Interfaces* (2023). doi:10.1021/acsami.2c18522

98. Jiang, X. *et al.* Oxidation State Modulation of Bimetallic Tin-Copper Oxide Nanotubes for Selective CO 2 Electroreduction to Formate. *Small* 18, 2204148 (2022).

99. Li, Y. *et al.* Rational Design and Synthesis of SnO x Electrocatalysts with Coralline Structure for Highly Improved Aqueous CO 2 Reduction to Formate. *ChemElectroChem* 3, 1618–1628 (2016).

100. Zhang, S., Kang, P. & Meyer, T. J. Nanostructured tin catalysts for selective electrochemical reduction of carbon dioxide to formate. *J. Am. Chem. Soc.* 136, 1734–1737 (2014).

101. Chen, Z. *et al.* Wavy SnO2 catalyzed simultaneous reinforcement of carbon dioxide adsorption and activation towards electrochemical conversion of CO2 to HCOOH. *Appl. Catal. B Environ.* 261, 118243 (2020).

102. Won, D. H. *et al.* Rational Design of a Hierarchical Tin Dendrite Electrode for Efficient Electrochemical Reduction of CO2. *ChemSusChem* 8, 3092–3098 (2015).

103. Rasul, S., Pugnant, A., Xiang, H., Fontmorin, J. M. & Yu, E. H. Low cost and efficient alloy electrocatalysts for CO2 reduction to formate. *J. CO2 Util.* 32, 1–10 (2019).

104. Han, P. *et al.* 2D Assembly of Confined Space toward Enhanced CO2 Electroreduction. *Adv. Energy Mater.* 8, 1–7 (2018).

105. Hou, X. *et al.* 3D core-shell porous-structured Cu@Sn hybrid electrodes with unprecedented selective CO 2 -into-formate electroreduction achieving 100%. *J. Mater. Chem. A* 7, 3197–3205 (2019).

106. Kumar, B. *et al.* Reduced SnO2 Porous Nanowires with a High Density of Grain Boundaries as Catalysts for Efficient Electrochemical CO2-into-HCOOH Conversion. *Angew. Chemie - Int. Ed.* 56, 3645–3649 (2017).

107. Wang, Y. *et al.* Laser-fabricated channeled Cu6Sn5/Sn as electrocatalyst and gas diffusion electrode for efficient CO2 electroreduction to formate. *Appl. Catal. B Environ.* 307, 120991 (2022).

108. Li, F. *et al.* Towards a better Sn: Efficient electrocatalytic reduction of CO 2 to formate by Sn/SnS 2 derived from SnS 2 nanosheets. *Nano Energy* 31, 270–277 (2017).

109. Li, W. *et al.* ZnSn nanocatalyst: Ultra-high formate selectivity from CO2 electrochemical reduction and the structure evolution effect. *J. Colloid Interface Sci.* 608, 2791–2800 (2022).

110. Liu, W., Zhang, Z., Huo, S., Ren, Q. & Liu, M. Bimetallic Zn3Sn2 electrocatalyst derived from mixed oxides enhances formate production towards CO2 electroreduction reaction. *Appl. Surf. Sci.* 608, 155110 (2023).

111. Jiang, X. *et al.* A highly selective tin-copper bimetallic electrocatalyst for the electrochemical reduction of aqueous CO2 to formate. *Appl. Catal. B Environ.* 259, 118040 (2019).

112. Lai, Q., Yuan, W., Huang, W. & Yuan, G. Sn/SnOx electrode catalyst with mesoporous structure for efficient electroreduction of CO2 to formate. *Appl. Surf. Sci.* 508, (2020).

113. Tian, J. *et al.* Bi–Sn Oxides for Highly Selective CO 2 Electroreduction to Formate in a Wide Potential Window. *ChemSusChem* 14, 2247–2254 (2021).

114. Chen, Y. *et al.* A Robust, Scalable Platform for the Electrochemical Conversion of CO 2 to Formate: Identifying Pathways to Higher Energy Efficiencies. *ACS Energy Lett.* 5, 1825–1833 (2020).

115. Ye, K. *et al.* Synergy effects on Sn-Cu alloy catalyst for efficient CO2 electroreduction to formate with high mass activity. *Sci. Bull.* 65, 711–719 (2020).

116. Cao, X., Wulan, B., Zhang, B., Tan, D. & Zhang, J. Defect evolution of hierarchical SnO 2 aggregates for boosting CO 2 electrocatalytic reduction. *J. Mater. Chem. A* 9, 14741–14751 (2021).

117. Li, F. Efficient electrochemical reduction of CO2 to formate using Sn-Polyaniline film on Ni foam. *Electrochim. Acta* 332, 135457 (2020).

118. Liu, H.-Y. *et al.* Selective Formate Production from the Electrochemical CO 2 Reduction Reaction of Surface Oxide-Modified InSn 4 Binary Catalysts. *ACS Appl. Energy Mater.* 5, 9895–9901 (2022).

119. Tian, J. *et al.* Highly Efficient and Selective CO 2 Electro-Reduction to HCOOH on Sn Particle-Decorated Polymeric Carbon Nitride. *ChemSusChem* cssc.202002184 (2020). doi:10.1002/cssc.202002184

120. He, Y., Jiang, W. J., Zhang, Y., Huang, L. B. & Hu, J. S. Pore-structure-directed CO2 electroreduction to formate on SnO2/C catalysts. *J. Mater. Chem. A* 7, 18428–18433 (2019).

121. Chen, C. *et al.* Sharp Cu@Sn nanocones on Cu foam for highly selective and efficient electrochemical reduction of CO2 to formate. *J. Mater. Chem. A* 6, 19621–19630 (2018).

122. An, X. *et al.* Electrodeposition of Tin-Based Electrocatalysts with Different Surface Tin Species Distributions for Electrochemical Reduction of CO 2 to HCOOH. *ACS Sustain. Chem. Eng.* 7, 9360–9368 (2019).

123. Fu, Y. *et al.* Nanoconfined Tin Oxide within N-Doped Nanocarbon Supported on Electrochemically Exfoliated Graphene for Efficient Electroreduction of CO 2 to Formate and C1 Products. *ACS Appl. Mater. Interfaces* 12, 16178–16185 (2020).

124. Wang, P. *et al.* Phase and structure engineering of copper tin heterostructures for efficient electrochemical carbon dioxide reduction. *Nat. Commun.* 9, 1–10 (2018).

125. Cheng, F. *et al.* Recent Progress of Sn-Based Derivative Catalysts for Electrochemical Reduction of CO2. *Energy Technol.* 9, 1–18 (2021).

126. Martín, A. J., Larrazábal, G. O. & Pérez-Ramírez, J. Towards sustainable fuels and chemicals through the electrochemical reduction of CO2: Lessons from water electrolysis. *Green Chem.* 17, 5114–5130 (2015).

127. Zhang, X., Guo, S.-X., Gandionco, K. A., Bond, A. M. & Zhang, J. Electrocatalytic carbon dioxide reduction: from fundamental principles to catalyst design. *Mater. Today Adv.* 7, 100074 (2020).

128. Strbac, S. B. & Adzic, R. R. Electrocatalysis, Fundamentals - Electron Transfer Process; Current-Potential Relationship; Volcano Plots. in *Encyclopedia of Applied Electrochemistry* 417–423 (Springer New York, 2014). doi:10.1007/978-1-4419-6996-5_485

129. Banoth, P., Kandula, C. & Kollu, P. Introduction to Electrocatalysts. in *ACS Symposium Series* 1432, 1–37 (American Chemical Society, 2022).

130. Ooka, H., Huang, J. & Exner, K. S. The Sabatier Principle in Electrocatalysis: Basics, Limitations, and Extensions. *Front. Energy Res.* 9, 1–20 (2021).

131. Calderón-Cárdenas, A., Paredes-Salazar, E. A. & Varela, H. Apparent Activation Energy in Electrochemical Multistep Reactions: A Description via Sensitivities and Degrees of Rate Control. *ACS Catal.* 10, 9336–9345 (2020).

132. Brett, C. M. A. & Brett, A. M. O. *Electrochemistry: Principles, Methods and Applications*. (Oxford University Press Inc., 1993).

133. Bard, A. J. & Faulkner, L. R. *Electrochemical Methods: Fundamentals and Applications, 2nd Edition*. (John Wiley & Sons, 2001).

134. Zhang, S., Fan, Q., Xia, R. & Meyer, T. J. CO 2 Reduction: From Homogeneous to Heterogeneous Electrocatalysis. *Acc. Chem. Res.* 53, 255–264 (2020).

135. Feng, D.-M., Zhu, Y.-P., Chen, P. & Ma, T.-Y. Recent Advances in Transition-Metal-Mediated Electrocatalytic CO2 Reduction: From Homogeneous to Heterogeneous Systems. *Catalysts* 7, 373 (2017).

136. Benson, E. E., Kubiak, C. P., Sathrum, A. J. & Smieja, J. M. Electrocatalytic and homogeneous approaches to conversion of CO 2 to liquid fuels. *Chem. Soc. Rev.* 38, 89–99 (2009).

137. Handoko, A. D., Wei, F., Jenndy, Yeo, B. S. & Seh, Z. W. Understanding heterogeneous electrocatalytic carbon dioxide reduction through operando techniques. *Nat. Catal.* 1, 922–934 (2018).

138. Ringe, S. *et al.* Double layer charging driven carbon dioxide adsorption limits the rate of electrochemical carbon dioxide reduction on Gold. *Nat. Commun.* 11, 33 (2020).

139. Damas, G. B. *et al.* On the Mechanism of Carbon Dioxide Reduction on Sn-Based Electrodes: Insights into the Role of Oxide Surfaces. *Catalysts* 9, 636 (2019).

140. Weekes, D. M., Salvatore, D. A., Reyes, A., Huang, A. & Berlinguette, C. P. Electrolytic CO 2 Reduction in a Flow Cell. *Acc. Chem. Res.* 51, 910–918 (2018).

141. Nesbitt, N. T. *et al.* Liquid–Solid Boundaries Dominate Activity of CO 2 Reduction on Gas-Diffusion Electrodes. *ACS Catal.* 10, 14093–14106 (2020).

142. Seger, B., Robert, M. & Jiao, F. Best practices for electrochemical reduction of carbon dioxide. *Nat. Sustain.* 6, 236–238 (2023).

143. Krischer, K. & Savinova, E. R. Fundamentals of Electrocatalysis. in *Handbook of Heterogeneous Catalysis* 3–5, 1873–1905 (Wiley-VCH Verlag GmbH & Co. KGaA, 2008).

144. Dunwell, M., Yan, Y. & Xu, B. Understanding the influence of the electrochemical double-layer on heterogeneous electrochemical reactions. *Curr. Opin. Chem. Eng.* 20, 151–158 (2018).

145. Pan, B., Wang, Y. & Li, Y. Understanding and leveraging the effect of cations in the electrical double layer for electrochemical CO2 reduction. *Chem Catal.* 2, 1267–1276 (2022).

146. König, M., Vaes, J., Klemm, E. & Pant, D. Solvents and Supporting Electrolytes in the Electrocatalytic Reduction of CO2. *iScience* 19, 135–160 (2019).

147. Marcandalli, G., Monteiro, M. C. O., Goyal, A. & Koper, M. T. M.

Electrolyte Effects on CO 2 Electrochemical Reduction to CO. *Acc. Chem. Res.* 55, 1900–1911 (2022).

148. Moura de Salles Pupo, M. & Kortlever, R. Electrolyte Effects on the Electrochemical Reduction of CO 2. *ChemPhysChem* 20, 2926–2935 (2019).

149. Bohra, D., Chaudhry, J. H., Burdyny, T., Pidko, E. A. & Smith, W. A. Modeling the electrical double layer to understand the reaction environment in a CO 2 electrocatalytic system. *Energy Environ. Sci.* 12, 3380–3389 (2019).

150. Nitopi, S. *et al.* Progress and Perspectives of Electrochemical CO 2 Reduction on Copper in Aqueous Electrolyte. *Chem. Rev.* 119, 7610–7672 (2019).

151. Koper, M. T. M. Thermodynamic theory of multi-electron transfer reactions: Implications for electrocatalysis. *J. Electroanal. Chem.* 660, 254–260 (2011).

152. Baruch, M. F., Pander, J. E., White, J. L. & Bocarsly, A. B. Mechanistic Insights into the Reduction of CO2 on Tin Electrodes using in Situ ATR-IR Spectroscopy. *ACS Catal.* 5, 3148–3156 (2015).

153. Deng, W., Zhang, P., Seger, B. & Gong, J. Unraveling the rate-limiting step of two-electron transfer electrochemical reduction of carbon dioxide. *Nat. Commun.* 13, 803 (2022).

154. Sabatier, P. *La Catalyse en Chimie Organique, Encyclopédie de Science Chimique Appliquée.* (C. Béranger (Paris, Liége), 1913).

155. Feaster, J. T. *et al.* Understanding Selectivity for the Electrochemical Reduction of Carbon Dioxide to Formic Acid and Carbon Monoxide on Metal Electrodes. *ACS Catal.* 7, 4822–4827 (2017).

156. Sánchez, O. G. *et al.* Recent advances in industrial CO 2 electroreduction. *Curr. Opin. Green Sustain. Chem.* 16, 47–56 (2019).

157. Tan, Y. C. *et al.* Pitfalls and Protocols: Evaluating Catalysts for CO 2 Reduction in Electrolyzers Based on Gas Diffusion Electrodes. *ACS Energy Lett.* 7, 2012–2023 (2022).

158. Jhong, H. R. M., Ma, S. & Kenis, P. J. Electrochemical conversion of CO2 to useful chemicals: Current status, remaining challenges, and future opportunities. *Curr. Opin. Chem. Eng.* 2, 191–199 (2013).

159. Wakerley, D. *et al.* Gas diffusion electrodes, reactor designs and key metrics of low-temperature CO2 electrolysers. *Nat. Energy* 7, 130–143 (2022).

160. Xu, D. *et al.* Electrocatalytic CO 2 reduction towards industrial applications. *Carbon Energy* 5, 1–27 (2023).

161. Salvatore, D. & Berlinguette, C. P. Voltage Matters When Reducing CO 2 in an Electrochemical Flow Cell. *ACS Energy Lett.* 5, 215–220 (2020).

162. Vass, Á., Kormányos, A., Kószó, Z., Endrődi, B. & Janáky, C. Anode Catalysts in CO 2 Electrolysis: Challenges and Untapped Opportunities. *ACS Catal.* 12, 1037–1051 (2022).

163. Sundén, B. Electrochemistry and thermodynamics. in *Hydrogen, Batteries and Fuel Cells* 15–36 (Elsevier, 2019). doi:10.1016/B978-0-12-816950-6.00002-6

164. Zhu, D. D., Liu, J. L. & Qiao, S. Z. Recent Advances in Inorganic Heterogeneous Electrocatalysts for Reduction of Carbon Dioxide. *Adv. Mater.* 28, 3423–3452 (2016).

165. Wei, C. *et al.* Approaches for measuring the surface areas of metal oxide electrocatalysts for determining their intrinsic electrocatalytic activity. *Chem. Soc. Rev.* 48, 2518–2534 (2019).

166. Chiacchiarelli, L. M., Zhai, Y., Frankel, G. S., Agarwal, A. S. & Sridhar, N. Cathodic degradation mechanisms of pure Sn electrocatalyst in a nitrogen atmosphere. *J. Appl. Electrochem.* 42, 21–29 (2012).

167. Ma, R. *et al.* Anodic SnO2porous nanostructures with rich grain boundaries for efficient CO2electroreduction to formate. *RSC Adv.* 10, 22828–22835 (2020).

168. Kas, R. *et al.* Electrochemical co2 reduction on nanostructured metal electrodes: Fact or defect? *Chem. Sci.* 11, 1738–1749 (2020).

169. Lu, Q., Rosen, J. & Jiao, F. Nanostructured metallic electrocatalysts for carbon dioxide reduction. *ChemCatChem* 7, 38–47 (2015).

170. Bai, X. *et al.* Exclusive Formation of Formic Acid from CO2 Electroreduction by a Tunable Pd-Sn Alloy. *Angew. Chemie - Int. Ed.* 56, 12219–12223 (2017).

171. Choi, S. Y., Jeong, S. K., Kim, H. J., Baek, I. H. & Park, K. T. Electrochemical Reduction of Carbon Dioxide to Formate on Tin-Lead Alloys. *ACS Sustain. Chem. Eng.* 4, 1311–1318 (2016).

172. He, J., Dettelbach, K. E., Huang, A. & Berlinguette, C. P. Brass and Bronze as Effective CO2 Reduction Electrocatalysts. *Angew. Chemie - Int. Ed.* 56, 16579–16582 (2017).

173. Moore, C. E. & Gyenge, E. L. Tuning the Composition of Electrodeposited Bimetallic Tin–Lead Catalysts for Enhanced Activity and Durability in Carbon Dioxide Electroreduction to Formate. *ChemSusChem* 10, 3512–3519 (2017).

174. Zhang, X., Li, F., Zhang, Y., Bond, A. M. & Zhang, J. Stannate derived bimetallic nanoparticles for electrocatalytic CO2 reduction. *J. Mater. Chem. A* 6, 7851–7858 (2018).

175. Li, Q. *et al.* Tuning Sn-Catalysis for Electrochemical Reduction of CO2 to CO via the Core/Shell Cu/SnO2 Structure. *J. Am. Chem. Soc.* 139, 4290–4293 (2017).

176. Ju, W. *et al.* Electrocatalytic Reduction of Gaseous CO2 to CO on Sn/Cu-Nanofiber-Based Gas Diffusion Electrodes. *Adv. Energy Mater.* 9, 1–6 (2019).

177. Salvini, C., Re Fiorentin, M., Risplendi, F., Raffone, F. & Cicero, G.

Active Surface Structure of SnO2 Catalysts for CO2 Reduction Revealed by Ab Initio Simulations. *J. Phys. Chem. C* 126, 14441–14447 (2022).

178. Cui, C., Wang, H., Zhu, X., Han, J. & Ge, Q. A DFT study of CO2 electrochemical reduction on Pb(211) and Sn(112). *Sci. China Chem.* 58, 607–613 (2015).

179. Cui, C. *et al.* Promotional effect of surface hydroxyls on electrochemical reduction of CO2 over SnOx/Sn electrode. *J. Catal.* 343, 257–265 (2016).

180. Ning, S. *et al.* Electrochemical reduction of SnO2 to Sn from the Bottom: In-Situ formation of SnO2/Sn heterostructure for highly efficient electrochemical reduction of carbon dioxide to formate. *J. Catal.* 399, 67–74 (2021).

181. Li, L. *et al.* Tuning Oxygen Vacancies of Oxides to Promote Electrocatalytic Reduction of Carbon Dioxide. *ACS Energy Lett.* 5, 552–558 (2020).

182. Deng, W. *et al.* Crucial Role of Surface Hydroxyls on the Activity and Stability in Electrochemical CO 2 Reduction. *J. Am. Chem. Soc.* 141, 2911–2915 (2019).

183. Dutta, A., Kuzume, A., Rahaman, M., Vesztergom, S. & Broekmann, P. Monitoring the Chemical State of Catalysts for CO2 Electroreduction: An In Operando Study. *ACS Catal.* 5, 7498–7502 (2015).

184. Dutta, A. *et al.* Probing the chemical state of tin oxide NP catalysts during CO2 electroreduction: A complementary operando approach. *Nano Energy* 53, 828–840 (2018).

185. Lee, S., Ocon, J. D., Son, Y. Il & Lee, J. Alkaline CO2 electrolysis toward selective and continuous HCOO- production over SnO2 nanocatalysts. *J. Phys. Chem. C* 119, 4884–4890 (2015).

186. Zhang, R., Lv, W. & Lei, L. Role of the oxide layer on Sn electrode in electrochemical reduction of CO 2 to formate. *Appl. Surf. Sci.*

356, 24–29 (2015).

187. Chen, Y. & Kanan, M. W. Tin oxide dependence of the CO 2 reduction efficiency on tin electrodes and enhanced activity for tin/tin oxide thin-film catalysts. *J. Am. Chem. Soc.* 134, 1986–1989 (2012).

188. Xiang, H. *et al.* Production of formate by CO 2 electrochemical reduction and its application in energy storage. *Sustain. Energy Fuels* 4, 277–284 (2020).

189. Van Daele, K. *et al.* Sn-Based Electrocatalyst Stability: A Crucial Piece to the Puzzle for the Electrochemical CO 2 Reduction toward Formic Acid. *ACS Energy Lett.* 6, 4317–4327 (2021).

190. Hori, Y. *et al.* 'deactivation of copper electrode' in electrochemical reduction of CO2. *Electrochim. Acta* 50, 5354–5369 (2005).

191. Ma, M., Liu, K., Shen, J., Kas, R. & Smith, W. A. In Situ Fabrication and Reactivation of Highly Selective and Stable Ag Catalysts for Electrochemical CO2 Conversion. *ACS Energy Lett.* 3, 1301–1306 (2018).

192. Ikemiya, N., Natsui, K., Nakata, K. & Einaga, Y. Long-Term Continuous Conversion of CO2 to Formic Acid Using Boron-Doped Diamond Electrodes. *ACS Sustain. Chem. Eng.* 6, 8108–8112 (2018).

193. Wuttig, A. & Surendranath, Y. Impurity Ion Complexation Enhances Carbon Dioxide Reduction Catalysis. *ACS Catal.* 5, 4479–4484 (2015).

194. Luc, W. *et al.* SO 2 -Induced Selectivity Change in CO 2 Electroreduction. *J. Am. Chem. Soc.* 141, 9902–9909 (2019).

195. Park, S., Wijaya, D. T., Na, J. & Lee, C. W. Towards the large-scale electrochemical reduction of carbon dioxide. *Catalysts* 11, 1–30 (2021).

196. Bienen, F. *et al.* Degradation study on tin- and bismuth-based gas-diffusion electrodes during electrochemical CO2 reduction in highly

alkaline media. *J. Energy Chem.* 62, 367–376 (2021).

197. Vanrenterghem, B. *et al.* Increase of electrodeposited catalyst stability via plasma grown vertically oriented graphene nanoparticle movement restriction. *Chem. Commun.* 53, 9340–9343 (2017).

198. He, M. *et al.* Oxygen induced promotion of electrochemical reduction of CO2 via co-electrolysis. *Nat. Commun.* 11, 1–10 (2020).

199. Choi, W., Won, D. H. & Hwang, Y. J. Catalyst design strategies for stable electrochemical CO2reduction reaction. *J. Mater. Chem. A* 8, 15341–15357 (2020).

200. Clark, E. L. *et al.* Standards and Protocols for Data Acquisition and Reporting for Studies of the Electrochemical Reduction of Carbon Dioxide. *ACS Catal.* 8, 6560–6570 (2018).

201. Birdja, Y. Y. & Vaes, J. Towards a Critical Evaluation of Electrocatalyst Stability for CO2 Electroreduction. *ChemElectroChem* 7, 4713–4717 (2020).

202. Popović, S. *et al.* Stability and Degradation Mechanisms of Copper-Based Catalysts for Electrochemical CO 2 Reduction. *Angew. Chemie Int. Ed.* 59, 14736–14746 (2020).

203. Nwabara, U. O. *et al.* Towards accelerated durability testing protocols for CO 2 electrolysis. *J. Mater. Chem. A* 8, 22557–22571 (2020).

204. Duarte, M. *et al.* Enhanced CO2electroreduction with metal-nitrogen-doped carbons in a continuous flow reactor. *J. CO2 Util.* 50, 101583 (2021).

205. Daems, N. *et al.* Nickel-containing N-doped carbon as effective electrocatalysts for the reduction of CO2 to CO in a continuous-flow electrolyzer. *Sustain. Energy Fuels* 4, 1296–1311 (2020).

206. De Mot, B., Ramdin, M., Hereijgers, J., Vlugt, T. J. H. & Breugelmans, T. Direct Water Injection in Catholyte-Free Zero-Gap Carbon Dioxide Electrolyzers. *ChemElectroChem* 7, 3839–3843

(2020).

207. Daele, K. Van *et al.* Enhanced Pomegranate-Structured SnO 2 Electrocatalysts for the Electrochemical CO 2 Reduction to Formate. *ChemElectroChem* 202201024, 1–9 (2023).

208. Artjom Maljusch, J. M. and W. S. A. S. B. E. V. Techniques and methodologies in modern electrocatalysis: evaluation of activity, selectivity and stability of catalytic materials. *Analyst* 139, 1274–1291 (2014).

209. Meier, J. C. *et al.* Stability investigations of electrocatalysts on the nanoscale. *Energy Environ. Sci.* 5, 9319–9330 (2012).

210. Burdyny, T. & Smith, W. A. CO2 reduction on gas-diffusion electrodes and why catalytic performance must be assessed at commercially-relevant conditions. *Energy Environ. Sci.* 12, 1442–1453 (2019).

211. Hodnik, N., Dehm, G. & Mayrhofer, K. J. J. Importance and Challenges of Electrochemical in Situ Liquid Cell Electron Microscopy for Energy Conversion Research. *Acc. Chem. Res.* 49, 2015–2022 (2016).

212. Zhu, Y., Wang, J., Chu, H., Chu, Y. C. & Chen, H. M. In Situ/ Operando Studies for Designing Next-Generation Electrocatalysts. *ACS Energy Lett.* 5, 1281–1291 (2020).

213. Jung, S. *et al.* Gastight Hydrodynamic Electrochemistry: Design for a Hermetically Sealed Rotating Disk Electrode Cell. *Anal. Chem.* 89, 581–585 (2017).

214. Moreno-Garciá, P. *et al.* Toward CO2 Electroreduction under Controlled Mass Flow Conditions: A Combined Inverted RDE and Gas Chromatography Approach. *Anal. Chem.* 92, 4301–4308 (2020).

215. Lin, X., Zalitis, C. M., Sharman, J. & Kucernak, A. Electrocatalyst Performance at the Gas/Electrolyte Interface under High-Mass-Transport Conditions: Optimization of the 'floating Electrode' Method. *ACS Appl. Mater. Interfaces* 12, 47467–47481 (2020).

216. Martens, S. *et al.* A comparison of rotating disc electrode, floating electrode technique and membrane electrode assembly measurements for catalyst testing. *J. Power Sources* 392, 274–284 (2018).

217. Geiger, S. *et al.* The stability number as a metric for electrocatalyst stability benchmarking. *Nat. Catal.* 1, 508–515 (2018).

218. Kim, Y. T. *et al.* Balancing activity, stability and conductivity of nanoporous core-shell iridium/iridium oxide oxygen evolution catalysts. *Nat. Commun.* 8, 1–8 (2017).

219. Goel, C., Bhunia, H. & Bajpai, P. K. Synthesis of nitrogen doped mesoporous carbons for carbon dioxide capture. *RSC Adv.* 5, 46568–46582 (2015).

220. Wan, X., Li, Y., Xiao, H., Pan, Y. & Liu, J. Hydrothermal synthesis of nitrogen-doped ordered mesoporous carbon via lysine-assisted self-assembly for efficient CO 2 capture. *RSC Adv.* 10, 2932–2941 (2020).

221. Chen, J. *et al.* Efficient and Simple Strategy to Obtain Ordered Mesoporous Carbons with Abundant Structural Base N Sites toward CO 2 Selective Capture and Catalytic Conversion. *ACS Sustain. Chem. Eng.* 10, 5175–5182 (2022).

222. Varela, A. S. *et al.* Electrochemical Reduction of CO 2 on Metal-Nitrogen-Doped Carbon Catalysts. *ACS Catal.* 9, 7270–7284 (2019).

223. Van Daele, K. *et al.* Sn-Based Electrocatalyst Stability: A Crucial Piece to the Puzzle for the Electrochemical CO2Reduction toward Formic Acid. *ACS Energy Lett.* 6, 4317–4327 (2021).

224. Zhang, R., Lv, W., Li, G. & Lei, L. Electrochemical reduction of CO2 on SnO2/nitrogen-doped multiwalled carbon nanotubes composites in KHCO3 aqueous solution. *Mater. Lett.* 141, 63–66 (2015).

225. Birdja, Y. Y., Shen, J. & Koper, M. T. M. Influence of the metal center of metalloprotoporphyrins on the electrocatalytic CO2 reduction to formic acid. *Catal. Today* 288, 37–47 (2017).

226. Zhao, Y., Liang, J., Wang, C., Ma, J. & Wallace, G. G. Tunable and Efficient Tin Modified Nitrogen-Doped Carbon Nanofibers for Electrochemical Reduction of Aqueous Carbon Dioxide. *Adv. Energy Mater.* 8, 1702524 (2018).

227. Duarte, M. *et al.* Enhanced CO2 electroreduction with metal-nitrogen-doped carbons in a continuous flow reactor. *J. CO2 Util.* 50, 101583 (2021).

228. Sheng, X. *et al.* N-doped ordered mesoporous carbons prepared by a two-step nanocasting strategy as highly active and selective electrocatalysts for the reduction of O2 to H2O2. *Appl. Catal. B Environ.* 176–177, 212–224 (2015).

229. Daems, N. *et al.* Doped ordered mesoporous carbons as novel, selective electrocatalysts for the reduction of nitrobenzene to aniline. *J. Mater. Chem. A* 6, 13397–13411 (2018).

230. Wang, Y. *et al.* Simple synthesis of metallic Sn nanocrystals embedded in graphitic ordered mesoporous carbon walls as superior anode materials for lithium ion batteries. *J. Power Sources* 219, 89–93 (2012).

231. Thommes, M. *et al.* Physisorption of gases, with special reference to the evaluation of surface area and pore size distribution (IUPAC Technical Report). *Pure Appl. Chem.* 87, 1051–1069 (2015).

232. Ferrari, A. C. & Basko, D. M. Raman spectroscopy as a versatile tool for studying the properties of graphene. *Nat. Nanotechnol.* 8, 235–246 (2013).

233. Schuepfer, D. B. *et al.* Assessing the structural properties of graphitic and non-graphitic carbons by Raman spectroscopy. *Carbon N. Y.* 161, 359–372 (2020).

234. Graulis, S. *et al.* Crystallography Open Database - An open-access collection of crystal structures. *J. Appl. Crystallogr.* 42, 726–729 (2009).

235. Seki, H., Ishizawa, N., Mizutani, N. & Kato, M. High Temperature Structures of the Rutile-Type Oxides, TiO2 and SnO2. *J. Ceram. Assoc. Japan* 92, 219–223 (1984).

236. Hursán, D. *et al.* Morphological Attributes Govern Carbon Dioxide Reduction on N-Doped Carbon Electrodes. *Joule* 3, 1719–1733 (2019).

237. Yoo, J. M., Shin, H., Chung, D. Y. & Sung, Y. E. Carbon Shell on Active Nanocatalyst for Stable Electrocatalysis. *Acc. Chem. Res.* 55, 1278–1289 (2022).

238. Pacquets, L. *et al.* Use of Nanoscale Carbon Layers on Ag-Based Gas Diffusion Electrodes to Promote CO Production. *ACS Appl. Nano Mater.* 5, 7723–7732 (2022).

239. Wen, W. *et al.* Cu particles decorated pomegranate-structured SnO2@C composites as anode for lithium ion batteries with enhanced performance. *Electrochim. Acta* 182, 272–279 (2015).

240. De Mot, B., Hereijgers, J., Duarte, M. & Breugelmans, T. Influence of flow and pressure distribution inside a gas diffusion electrode on the performance of a flow-by CO2 electrolyzer. *Chem. Eng. J.* 378, 1–8 (2019).

241. Kim, J. Y. *et al.* Quasi-graphitic carbon shell-induced Cu confinement promotes electrocatalytic CO2 reduction toward C2+ products. *Nat. Commun.* 12, 1–11 (2021).

242. Fayos, J. Possible 3D Carbon Structures as Progressive Intermediates in Graphite to Diamond Phase Transition. *J. Solid State Chem.* 148, 278–285 (1999).

243. Moore, W. J. & Pauling, L. The Crystal Structures of the Tetragonal Monoxides of Lead, Tin, Palladium, and Platinum. *J. Am. Chem. Soc.* 63, 1392–1394 (1941).

244. Wyckoff, R. W. G. Second edition. Interscience Publishers, New York, New York Sample known as white tin. *Cryst. Struct.* 1, 7–83 (1963).

245. Moulder, J. F., Stickle, W. F., Sobol, P. E. & Bomben, K. D. *Handbook of X-ray Photoelectron Spectroscopy*. (Perkin-Elmer Corporation, 1992).

246. Casebolt, R., Levine, K., Suntivich, J. & Hanrath, T. Pulse check: Potential opportunities in pulsed electrochemical CO2 reduction. *Joule* 5, 1987–2026 (2021).

247. Gupta, N., Gattrell, M. & MacDougall, B. Calculation for the cathode surface concentrations in the electrochemical reduction of CO2 in KHCO3 solutions. *J. Appl. Electrochem.* 36, 161–172 (2006).

248. Kim, C., Weng, L.-C. & Bell, A. T. Impact of Pulsed Electrochemical Reduction of CO 2 on the Formation of C 2+ Products over Cu. *ACS Catal.* 10, 12403–12413 (2020).

249. Clark, E. L. & Bell, A. T. Chapter 3. Heterogeneous Electrochemical CO2 Reduction. in 98–150 (2020). doi:10.1039/9781788015844-00098

250. Arán-Ais, R. M., Scholten, F., Kunze, S., Rizo, R. & Roldan Cuenya, B. The role of in situ generated morphological motifs and Cu(i) species in C2+ product selectivity during CO2 pulsed electroreduction. *Nat. Energy* 5, 317–325 (2020).

251. Lin, S.-C. *et al.* Operando time-resolved X-ray absorption spectroscopy reveals the chemical nature enabling highly selective CO2 reduction. *Nat. Commun.* 11, 3525 (2020).

252. Lee, S. H. *et al.* Correlating Oxidation State and Surface Area to Activity from Operando Studies of Copper CO Electroreduction Catalysts in a Gas-Fed Device. *ACS Catal.* 10, 8000–8011 (2020).

253. Timoshenko, J. *et al.* Steering the structure and selectivity of CO2 electroreduction catalysts by potential pulses. *Nat. Catal.* 5, 259–267 (2022).

254. Jännsch, Y. *et al.* Pulsed potential electrochemical CO2 reduction for enhanced stability and catalyst reactivation of copper electrodes. *Electrochem. commun.* 121, 106861 (2020).

255. Shiratsuchi, R., Aikoh, Y. & Nogami, G. Pulsed Electroreduction of

CO 2 on Copper Electrodes. *J. Electrochem. Soc.* 140, 3479–3482 (1993).

256. Engelbrecht, A. *et al.* On the Electrochemical CO 2 Reduction at Copper Sheet Electrodes with Enhanced Long-Term Stability by Pulsed Electrolysis. *J. Electrochem. Soc.* 165, J3059–J3068 (2018).

257. Shiratsuchi, R. & Nogami, G. Pulsed Electroreduction of CO 2 on Silver Electrodes. *J. Electrochem. Soc.* 143, 582–586 (1996).

258. Kedzierzawski, P. & Augustynski, J. Poisoning and Activation of the Gold Cathode during Electroreduction of CO 2. *J. Electrochem. Soc.* 141, L58–L60 (1994).

259. Lee, C. W., Cho, N. H., Nam, K. T., Hwang, Y. J. & Min, B. K. Cyclic two-step electrolysis for stable electrochemical conversion of carbon dioxide to formate. *Nat. Commun.* 10, 3919 (2019).

260. Blom, M. J. W., Smulders, V., van Swaaij, W. P. M., Kersten, S. R. A. & Mul, G. Pulsed electrochemical synthesis of formate using Pb electrodes. *Appl. Catal. B Environ.* 268, 118420 (2020).

261. Du, J. *et al.* A New Pathway for CO 2 Reduction Relying on the Self-Activation Mechanism of Boron-Doped Diamond Cathode. *JACS Au* 2, 1375–1382 (2022).

262. Sreekanth, N., Nazrulla, M. A., Vineesh, T. V., Sailaja, K. & Phani, K. L. Metal-free boron-doped graphene for selective electroreduction of carbon dioxide to formic acid/formate. *Chem. Commun.* 51, 16061–16064 (2015).

Personal Information

Publications in international peer-reviewed journals included in the Web of Science

1 Daems, N.; De Mot, B.; Choukroun, D.; Van Daele, K.; Li, C.; Hubin, A.; Bals, S.; Hereijgers, J.; Breugelmans, T. Nickel-Containing N-Doped Carbon as Effective Electrocatalysts for the Reduction of CO2 to CO in a Continuous-Flow Electrolyzer. *Sustain. Energy Fuels* 2020, *4* (3), 1296–1311. https://doi.org/10.1039/c9se00814d.

2 Laemont, A.; Abednatanzi, S.; Derakshandeh, P. G.; Verbruggen, F.; Fiset, E.; Qin, Q.; Van Daele, K.; Meledina, M.; Schmidt, J.; Oschatz, M.; Van Der Voort, P.; Rabaey, K.; Antonietti, M.; Breugelmans, T.; Leus, K. Covalent Triazine Framework/Carbon Nanotube Hybrids Enabling Selective Reduction of CO2 to CO at Low Overpotential. *Green Chem.* 2020, *22* (10), 3095–3103. https://doi.org/10.1039/d0gc00090f.

3 Li, C.; Tardajos, A. P.; Wang, D.; Choukroun, D.; Van Daele, K.; Breugelmans, T.; Bals, S. A Simple Method to Clean Ligand Contamination on TEM Grids. *Ultramicroscopy* 2021, *221* (December 2020), 113195. https://doi.org/10.1016/j.ultramic.2020.113195.

4 Van Daele, K.; De Mot, B.; Pupo, M.; Daems, N.; Pant, D.; Kortlever, R.; Breugelmans, T. Sn-Based Electrocatalyst Stability: A Crucial Piece to the Puzzle for the Electrochemical CO2Reduction toward Formic Acid. *ACS Energy Lett.* 2021, *6* (12), 4317–4327. https://doi.org/10.1021/acsenergylett.1c02049.

5 Van Daele, K.; Arenas-Esteban, D.; Choukroun, D.; Hoekx, S.; Rossen, A.; Daems, N.; Pant, D.; Bals, S.; Breugelmans, T. Enhanced Pomegranate-Structured SnO_2 Electrocatalysts for the Electrochemical CO_2 Reduction to Formate. *ChemElectroChem* 2023, 202201024, 1–9.
https://doi.org/10.1002/celc.202201024

Oral Presentations at international conferences

1 Van Daele, K.; Daems, N.; Pant, D.; Breugelmans, T. Increasing Sn-based Electrocatalyst Stability for the Electrochemical CO_2 Reduction to Formic Acid: a Particle Confinement Strategy. 29th topical meeting of the International Society of Electrochemistry (ISE), 19-21 April 2021, Mikulov, Czech Republic. (Held online)

2 Van Daele, K.; Daems, N.; Pant, D.; Breugelmans, T. A Deep Dive into the Stability of Sn-based Electrocatalysts for the Electrochemical CO_2 Reduction Towards Formic Acid. Electrochemistry 2022 (Berlin), 27-30 September 2022, Berlin, Germany.

3 Van Daele, K.; Daems, N.; Pant, D.; Breugelmans, T. An in-depth Exploration of the Electrocatalytic Stability of Sn-based Electrocatalysts for the Electrochemical CO2 Reduction Towards Formate. 244th ECS Meeting, 8-12 October 2023, Gothenburg, Sweden.

Oral Presentations at national conferences

1 Van Daele, K.; Daems, N.; Choukroun, D.; Pant, D.; Breugelmans, T. Carbon-supported Cu/SnO_2 Core-shell Nanoparticles for the Selective Electrochemical CO_2 Reduction Towards Formic Acid. Chemical Research in Flanders (CRF-2)

symposium Blankenberge, 14-16 October 2019, Blankenberge, Belgium.

2 Van Daele, K.; Daems, N.; Pant, D.; Breugelmans, T. Increasing Sn-based Electrocatalyst Stability for the Electrochemical CO_2 Reduction to Formic Acid: a Particle Confinement Strategy. CAPTURE Days, 26 - 27 August 2021, Gent, Belgium. (Held online)

3 Van Daele, K.; Daems, N.; Pant, D.; Breugelmans, T. Enhancing the stability of Sn-based electrocatalysts for the electrochemical CO_2 reduction towards formate. CAPTURE Science Talks, 5 June 2023, Gent, Belgium. (Held online)

Poster Presentations at international conferences

1 Van Daele, K.; Daems, N.; Choukroun, D.; Pant, D.; Breugelmans, T. Carbon-supported Cu/SnO_2 Core-shell Nanoparticles for the Selective Electrochemical CO_2 Reduction Towards Formic Acid. 71st Annual Meeting of the International Society of Electrochemistry (ISE), 30 August - 4 September 2020, Belgrade, Serbia. (Held online)

2 Van Daele, K.; Daems, N.; Choukroun, D.; Pant, D.; Breugelmans, T. Carbon-supported Cu/SnO_2 Core-shell Nanoparticles for the Selective Electrochemical CO_2 Reduction Towards Formic Acid. International Conference on Electrocatalysis for Energy Applications and Sustainable Chemicals (EcoCat), 23-25 November 2020. (Held online)

3 Van Daele, K.; Daems, N.; Pant, D.; Breugelmans, T. Increasing Sn-based Electrocatalyst Stability for the Electrochemical CO_2 Reduction to Formic Acid: a Particle Confinement Strategy.

International Conference on Electrocatalysis for Renewable Energy (Elcorel), 29-31 March 2021. (Held online)